Earth-Fixed Heave Compensation

Master Thesis

T. Ouwehand

TUDelft

MARINE CONTRACTORS

Earth-Fixed Heave Compensation

Master Thesis

by

T. Ouwehand

to obtain the degree of Master of Science in Offshore and Dredging Engineering
at Delft University of Technology

Student number:	4347153	
Project duration:	February 10, 2020 – December 22, 2020	
Thesis committee:	Prof. Dr. Ir. A. Metrikine	TU Delft, Chairman
	Dr. Ir. B. Ummels	TU Delft, Supervisor
	Ir. M. Burger	Heerema Marine Contractors
	Ing. P. Geene	Heerema Marine Contractors

Preface

This thesis is written to obtain a master's degree in Offshore and Dredging Engineering at Delft University of Technology. I was given the opportunity to investigate the dynamic behavior of earth-fixed heave compensation for the installation of offshore wind turbines at Heerema Marine Contractors.

Heerema Marine Contractors presented me a concept regarding active/passive heave compensation for their vessels. The system could possibly provide a novel way of installing wind turbines using only a fraction of the energy of a regular active heave compensator. The use of a mechanical system on board of a floating vessel to install offshore wind turbines combines three of my main interests: the analysis of mechanical systems, the offshore industry and sustainability.

The time we live in brings lots of challenges of which one of them is climate change. I believe we should always develop new and more sustainable ways to harvest energy in order to provide future generations the same quality of life as we have now. With my background as a mechanical engineer, and after graduation as offshore engineer, I hope to contribute to this goal by investigating a novel method for the installation of offshore wind turbines.

I would like to thank my university supervisor Bart Ummels for helping me writing this thesis and always letting me critically reflecting on my work. Secondly, I want to thank my supervisors from Heerema, Maarten Burger and Paul Geene. The technical discussions we had inspired me and always got me thinking in a different way. Furthermore, I would like to thank Joris van Drunen for his technical support. You all have the ability to make me come up with answers myself, by posing the right questions. Also, I would like to thank Heerema Marine Contractors in general. During my time working as a student before graduating, I was given the opportunity to go offshore multiple times. This enlarged my enthusiasm for the industry even more and provided me with lots of practical experience. Furthermore, I would like to thank my family and friends for always supporting me during my time at university.

Enjoy reading!

T. Ouwehand
Leiden, December 2020

Summary

With a global growing demand of energy, more offshore wind farms are installed, further away and in deeper waters. Nowadays, offshore wind turbines are mostly installed by jack-up installation vessels. Most existing jack-up vessels have legs that are becoming too short for these water depths while offshore wind turbines are increasing in size year after year. Since 2014, the turbine capacity of newly installed wind turbines has increased by 16% every year. Therefore, larger jack-up crane vessels are needed and installation by floating crane vessels is being considered.

Heerema Marine Contractors aims to be one of the leaders in the offshore wind installation with her large crane vessels such as HLV Aegir, SSCV Thialf and SSCV Sleipnir. The challenge of floating installation of offshore wind turbines is that motions of the vessel are transferred to the rotor-nacelle assembly (RNA) while low tolerances apply for the installation of an RNA. Vertical motions can be reduced by means of a heave compensation system. Such systems are available but come with certain drawbacks: they are difficult to retrofit to a vessel, use a large amount of energy and are rather expensive. A possible solution to these problems could be a novel concept called earth-fixed heave compensation. In this concept, the crane wire is connected to the seabed via a transmission on board of the vessel, transforming an upward motion of the vessel into a downward motion of the RNA and vice versa. At present, it is unclear if such a system is technically feasible.

In this research, an analytical model of an earth-fixed heave compensation system is developed. The objective of the model is to gain insight in the influence of design parameters such as the transmission and stiffness of the system. The model is set up in three stages: Stage 1 comprising one degree of freedom for the transmission; Stage 2 comprising two additional degrees of freedom for the sheaves that connect the earth-fixed wire from the seabed to the transmission; Stage 3 comprising all other sheaves, crane reeving and payload, resulting in a sixteen degrees of freedom model.

A first finding is that wire damping has a negligible influence on the results because natural frequencies of the system are found to lie outside the wave frequency range. However, the first natural frequency is close to the wave frequency range, resulting in a larger response amplitude for both transmission and vertical payload motion in the higher frequencies. Furthermore, it is shown that the inertia of the sheaves of the earth-fixed wire can be neglected for a range of transmission inertias and earth-fixed wire stiffnesses. On top of this, the model confirms that the inertia of the other sheaves can be modelled by means of an equivalent inertia block, to simplify the model for time-domain simulations. The losses in wire tension due to wire-sheave interaction were approximately 5% and it is shown that they can be modelled accurately by means of a *sigmoid* function.

Frequency-domain simulations showed that the heading of the vessel, or wave direction, has a significant influence on the vertical RNA motions. On top of that, increasing peak periods generally result in larger vertical RNA motions. A time-domain simulation for typical North Sea environmental conditions, head waves and a fixed crane slew angle without the heave compensator is made to compare results with. These simulations have shown that it is in principle possible to reduce vertical RNA motions. For a given sea state, 80% motion reduction is achieved by tuning the transmission ratio of the system. It is shown that the location of the earth-fixed wire has an impact on the vessel and payload motions. When located on the starboard side of the vessel, rather than reducing the vertical payload motions that are induced by vessel roll, those motions of the vessel itself are actually increased. Further simulations show that the stiffness of the earth-fixed wire and the losses occurring due to wire-sheave interaction determine the performance for a large part.

Although the overall performance of the system can be considered promising, additional research is needed to confirm whether earth-fixed heave compensation can be competitive relative to existing passive and active heave compensation systems with a performance of 80% to 95%. Also, it is recommended that the behavior of the system for different sea states is investigated. Sensitivity analyses already show that shorter wave periods result in a significant drop in performance. The vessel heading seems to have a limited influence on the performance of the heave compensator.

Contents

List of Figures

List of Tables

Nomenclature

List of Abbreviations

AHC	Active Heave Compensation
API	Application Programming Interface
CSMC	Combined Ship Motion Compensation
CTW	Constant Tension Winch
DSMC	Direct Ship Motion Compensation
EFHC	Earth-Fixed Heave Compensation
GBS	Gravity Based Structure
HLV	Heavy Lift Vessel
JUV	Jack-Up Vessel
LRFD	Load and Resistance Factor Design
PHC	Passive Heave Compensation
RAO	Response Amplitude Operator
RNA	Rotor-Nacelle Assembly
SDA	Significant Double Amplitude
SPF	Spreader Frame
SPHC	Subsea Passive Heave Compensation
SSCV	Semi Submersible Crane Vessel
WSD	Working Stress Design

1

Introduction

1.1. Offshore wind and turbines

New offshore wind farms are installed further away and in deeper waters (Wind Europe, 2019). Figure 1.1 shows that the average water depth of installed wind farms has increased every year since 2011. Nowadays, offshore wind turbines are mostly installed by jack-up installation vessels. Since most existing jack-up vessels have legs that are becoming too short for these water depths (Temporary Works Design, 2019), bigger jack-up crane vessels should be designed, or installation by floating crane vessels should be considered. An overview of some of the currently available wind installation vessels and new vessels to come is presented in Table 1.1. Heerema Marine Contractors aims to be one of the leaders in the offshore wind installation with her large crane vessels such as HLV Aegir, SSCV Thialf and SSCV Sleipnir (see Figure 1.2).

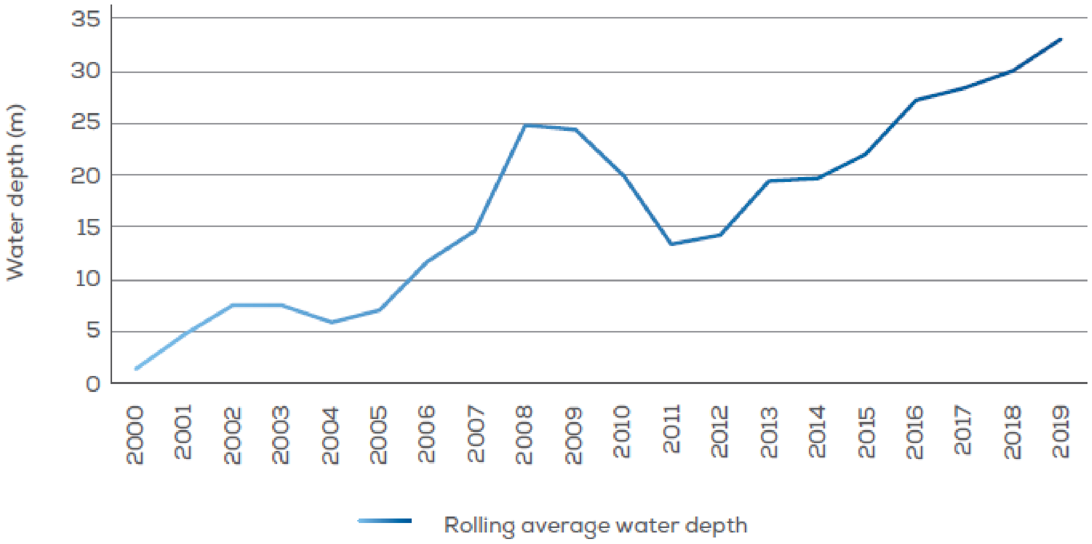

Figure 1.1: Average water depth of online offshore wind farms (Wind Europe, 2019)

Besides moving to deeper waters, offshore wind turbines are growing year after year. Since 2014, the turbine capacity of newly installed wind turbines has increased by 16% every year (Wind Europe, 2019). This trend is clearly shown in Figure 1.3. The increasing power output evidently means that turbines are getting larger as well. This, again, asks for installation by larger jack-up vessels or floating installation.

1.2. Wind turbine installation and floating installation

In general, an offshore wind turbine consists of the following components: foundation, transition piece, tower, nacelle, hub and blades. The blades and nacelle are often referred to as the rotor-nacelle assembly or

Figure 1.2: Part of Heerema's fleet. From left to right, top to bottom: SSCV Thialf, HLV Aegir, SSCV Sleipnir, Kolga (tug), Bylgia (tug). Source: Heerema

RNA. The foundation of the turbine can be a gravity based structure (GBS), a jacket structure or a monopile. The last one is the most widely used foundation for several reasons. Monopiles are relatively straightforward to design, fabricate and install (Thomsen, 2014). The monopile is usually hammered into the soil using a hydraulic hammer. The next step is to install the transition piece, which forms the connection between the monopile and the tower, on top of the monopile. The connection between monopile and transition piece is normally a grouted connection, however, recent developments show that the use of a friction based slip joint connection could be used for the connection of the transition piece to the monopile (Heerema Marine Contractors, 2020b, Segeren et al., 2014).

On top of the tower, the nacelle (including generator), rotor hub and three blades need to be installed. This is generally done by single blade installation in horizontal position, which means that the nacelle, including the hub, is installed on the tower first. After this step, the blades are installed one by one. The hub is turned two times by use of a motor or a hydraulic unit in order to align for the blade that is usually positioned horizontally. Alternatively, the turbine can be installed in its entirety, including the tower. This method has been used for projects with only a limited amount of wind turbines, such as the Beatrice Wind Farm Demonstrator Project (Scaldis, 2020) and Hywind (Saipem, 2020), respectively, two and five turbines were installed. Fred. Olsen Windcarrier (2013) demonstrated that a turbine can also be installed using a so called 'bunny-ear' con-

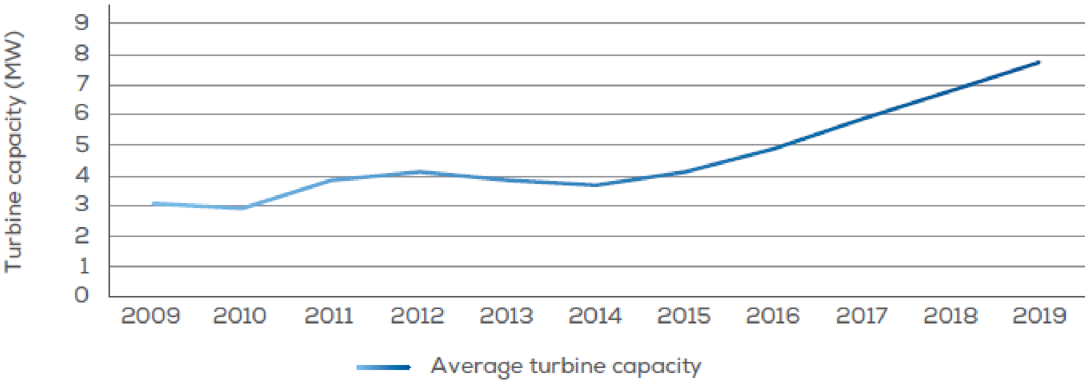

Figure 1.3: Yearly average of newly installed offshore wind turbine rated capacity (Wind Europe, 2019)

Figure 1.4: Blade installation on nacelle on board of vessel (Heerema Marine Contractors, 2020a)

Figure 1.5: RNA lift from vessel to turbine tower (Heerema Marine Contractors, 2020a)

Figure 1.6: RNA installed on turbine tower (Heerema Marine Contractors, 2020a)

figuration. In this method, the nacelle and two blades (in 10 and 2 o'clock position) are installed onto the tower in one go. After this, the last blade is installed separately.

This research considers a novel method for installation of the RNA components. Here, the nacelle, hub and also the rotor blades are assembled first on board the vessel. This process is shown in Figure 1.4, Figure 1.5 and Figure 1.6. First, the nacelle is installed on the red and white dummy tower which is fixed on the vessel. Secondly, the blades are installed on the nacelle one by one. At last, the whole RNA is disconnected from the dummy tower and installed on the turbine tower.

The single-blade installation method has as main advantage that the operability compared to integral installation is higher. The wind loads, and therefore motions of the blade, are lower, which increases operability. However, for installation by a floating vessel, this method can take more time due to the number of outboard lifts that is needed, in which there is a relative motion between the vessel and the turbine tower. The integral installation requires just one outboard lift, which is a large benefit since only shorter weather windows are needed for installation. The other lifts are conducted on board and therefore more controlled. For this installation method, the needed weather window is shorter, although weather limits might also be lower. This means that the operability for the integral installation does not have to better per se. Note that this method also requires a dummy tower on board of the vessel suited for the turbine.
Table 1.1 gives an overview of some of the currently available and new vessels[1] which are or can be used for the installation of offshore wind turbines. It can be seen that the new ships are either heavy lift vessels (HLV) or have longer legs and therefore a bigger maximum water depth in which they can operate.

The main advantage of installation by a jack-up vessel is that the influence of waves and current is limited, resulting in the vessel being a stable platform when jacked up. In general, this is not the case for floating vessels since they are free to move, to some extent. However, jack-up vessels tend to have limited deck space due to the legs that pierce through the deck. On top of that, the location where the vessel can jack up is dependent on soil stability and once jacked up, the vessel is unable to move. Also jacking operations, including soil preloading and controlled pull-out, take time. Taking the wind direction during installation into account,

---

[1] For the new vessels, the expected year that the vessel will be in service is shown.

this can be a problem. Furthermore, the operability of a jack-up vessel is limited by the water depth. On top of that, jack-up vessels may not be allowed to jack up in the desired position due readily installed cables (DNV GL, 2018), this is an additional challenge when installing offshore wind farms. Installation by a floating vessel is independent of water depth and soil conditions. As mentioned before, there will be an increase in the use of floating vessels due to increasing water depths, increasing wind turbine size and increasing number of projects. However, with floating installation of wind turbines new challenges come along.

Vessel	Type	Company	Year	Leg length	Max. water depth
MPI Adventure	JUV	MPI Offshore/Van Oord	2011	71 m	40 m
Blue Tern	JUV	Fred. Olsen Windcarrier	2012	106 m	65 m
Brave Tern / Bold Tern	JUV	Fred. Olsen Windcarrier	2013	92 m	60 m
Aeolus	JUV	Van Oord	2014	81 m	45 m
Bokalift 1	HLV	Boskalis	2017	n/a	n/a
Orion	HLV	DEME	2019	n/a	n/a
Bokalift 2	HLV	Boskalis	2021	n/a	n/a
Vole au Vent	JUV	Jan de Nul	2022	90 m	50 m
Voltaire	JUV	Jan de Nul	2022	130 m	80 m
Thialf	SSCV	Heerema	1985	n/a	n/a
Aegir	HLV	Heerema	2013	n/a	n/a
Sleipnir	SSCV	Heerema	2019	n/a	n/a

Table 1.1: Selection of currently available and new vessels for offshore wind installation.

1.3. Heave compensation and working principle of new concept

Due to the presence of waves, vessels move in multiple directions. Vessels move back and forth (surge), sideways (sway) and up and down (heave). Besides, vessels can rotate around their x-, y- and z-axis, respectively called roll, pitch and yaw. For crane vessels, three of these motions, heave, roll and pitch can result in vertical motions of the payload. Heave compensation is generally used to decouple the motion of the ship and a load. It can also be used to reduce dynamic loads in hoisting wires during, for instance, deep water lifting operations (Herdzik, 2014). This report considers a new heave compensation system called earth-fixed heave compensation (EFHC).

To understand the working principle of earth-fixed heave compensation, it is important to first explain the basic principle of an offshore crane. Figure 1.7 shows a simple overview of the mast crane on HLV Aegir, which is used to describe for the basic challenges of floating installation and the use of heave compensation. The crane block, to which a payload is attached, is connected to the crane boom via the crane wire. One side is the so called *dead end*, which is fixed to the crane boom. The other end of the wire is connected to a winch inside the crane pedestal. The winch is used to control the vertical position of the load. In this simplified figure, the wire to the crane block has only a single reeving. In reality, multiple reevings are used to increase lifting capacity. Assuming that the normal crane winch is not rotating, the heave motions of the ship will be transferred almost directly to the suspended payload.

Since there is a desire to reduce vertical motions of the payload, a concept was developed to connect the dead end of the crane wire to a transmission on board of the vessel (represented by the blue wire in Figure 1.8). This transmission is subsequently connected to the seabed (represented by the yellow wire in Figure 1.8). Now, when dimensioned properly, this system can counteract a part of the vessel motions. For example, if the vessel moves in a downward direction (negative heave), the yellow wire slackens. The transmission should be set up in such a way that slackening of the yellow wire results in pulling in of the blue wire. In this way, the load in crane is pulled up in case of downward motion of the vessel. This means that the load remains in place. How this works for a simply reeved crane is shown in Figure 1.9. In reality, however, the ship does not only move in vertical direction. This can have a negative influence on the behaviour of the system. A combination of heave, roll and pitch motions results in vertical movement of the payload. All concepts contain a constant tension winch to obtain a static equilibrium in the transmission. Although the use of the proposed heave compensation system is certainly not limited to the installation of RNA's, the focus of this thesis is on the installation of RNA's.

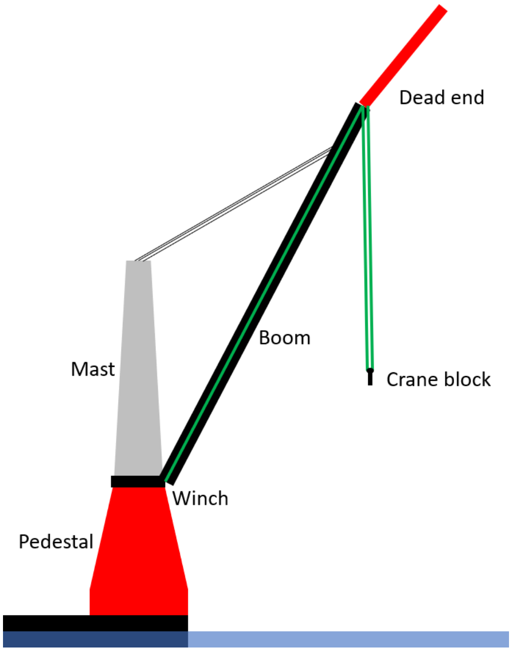

Figure 1.7: Mast crane terminology

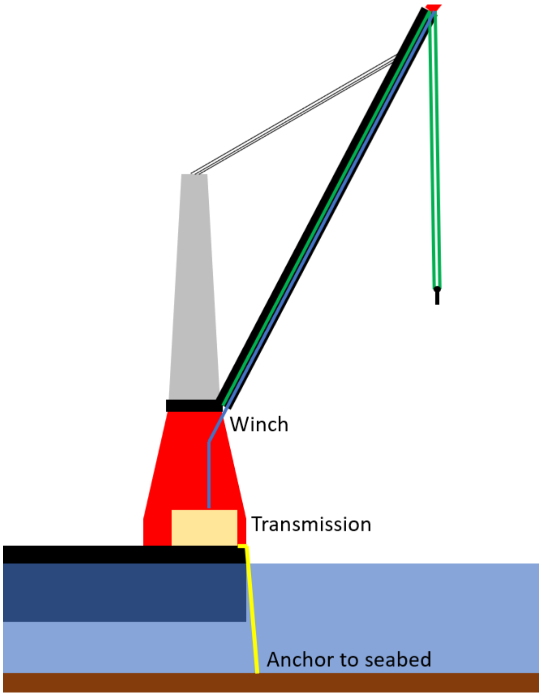

Figure 1.8: Basic overview of mast crane and principle of earth fixed heave compensation.

1.4. Problem statement

The difficulty of floating installation of offshore wind turbines is that the motions of the vessel are being transferred to the RNA. The RNA is generally to be connected to the turbine tower via a bolted flange connection. This type of connection is known to have small tolerances during installation. On top of this, the installation of offshore wind turbines is very repetitive work compared to the one-off installations typically performed in the offshore oil and gas industry. This means that the motions of the vessel are not only important for the installation tolerances, but also in terms of operability. Vertical motions can be reduced by means of a heave compensation system, either passive or active. Both systems are available but come with certain drawbacks. First of all, active heave compensation systems are difficult to retrofit to a vessel, this means that it can be rather difficult to install such a system on Heerema's already existing vessels. On top of that, active heave compensation uses a large amount of energy during operation. On HLV Aegir, for instance, 3 MW is needed for the heave compensation of the auxiliary crane block. For a single lift this would not be a concern, but the energy, and thus fuel consumption can add up when a large number of lifts need to be executed, which is not in line with Heerema's mission statement to be the *'leading marine contractor creating sustainable value(s) for clients and stakeholders'* and goal to become carbon neutral. Lastly, the systems are relatively expensive. A possible solution to these stated problems could be the proposed earth-fixed heave compensation. Although first simulations by Heerema have shown a promising results, realistic behaviour of the system was not investigated. These simulations merely demonstrated a proof of concept. For instance, no losses due to sheave friction and wire bending were taken into account and the reeving of the system was only consisting of 2 crane wires. The next step is to assess the performance of the system in a more detailed way.

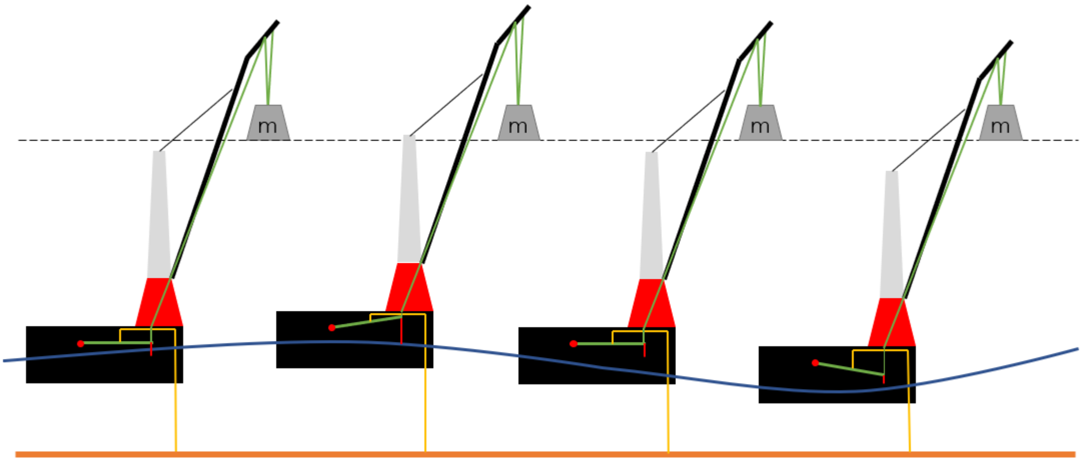

Figure 1.9: Working principle of the sytem for a simple crane reeving. The hoist wire is represented by the green wire, the earth fixed wire by the orange wire, and the constant tension winch by the red wire.

1.5. Research objective and questions

The objective of this thesis is to investigate the effectiveness of an earth-fixed heave compensation for reducing vertical payload motions. To provide an answer to this question, other research questions have to be answered first:

- What are typical environmental conditions during installation of offshore wind turbines?
- What are the corresponding vessel motions?
- How can earth fixed heave compensation be modelled?
- What is the effect of stiffness, inertia and energy losses of the system on its behavior?
- Can earth-fixed heave compensation reduce RNA motions?
- How can earth-fixed heave compensation be tuned to improve performance?

1.6. Methodology and thesis outline

The research is structured as follows. Chapter 2 provides a theoretical background and the modelling approach wherein literature is discussed to find out what is known in the field of heave compensation and modelling of offshore wind installation. On top of that, hydromechanic theory is considered. The way in which all structural elements of proposed system are modelled is discussed next. Furthermore, a clear overview is given on what is investigated under which assumptions and what is not considered in this research.

In chapter 3, RAO's of the vertical RNA motions are calculated to gain insight in which are present during a regular lift. The modelling approach regarding the crane wires, RNA, rigging and tugger lines are discussed. Frequency domain simulations have been performed for a given set of environmental conditions as chosen in chapter 2.

In chapter 4, the modelling of the heave compensation is covered. An analytical solution is found for the heave compensation system in the frequency domain. Note that this analytical solution is not used to prove that the heave compensation system works as desired, but to validate the choices made with regards to the modelling of the sheaves and wires.

Chapter 5 provides information about the time-domain simulations and the results of these simulations. The performance of the system, and the sensitivity of certain design parameters such as wire stiffness and inertia and losses caused by wire-sheave interaction on the system's performance are assessed.

Chapter 6 reflects on aforementioned research objectives and presents all conclusions and recommendations for potential further development of the earth-fixed heave compensation system.

2

Theoretical Background and Modelling Approach

This chapter provides a theoretical background on operability, heave compensation systems, hydromechanics and structural modelling of proposed heave compensation system. Furthermore, all delineations and assumptions are listed.

2.1. Offshore operations and operability

In order to define operability, it is necessary to distinguish weather restricted from weather unrestricted operations. DNV GL (2018) provides a method to determine whether an operation should be considered weather restricted or unrestricted. To determine this for a wind turbine installation with a floating vessel, one should determine the operation's duration first. This duration is called the reference period T_R and can be calculated by Equation 2.1 (DNV GL, 2018).

$$T_R = T_{POP} + T_c \tag{2.1}$$

In which T_{POP} stands for the planned operation period and T_C is the estimated maximum contingency time. According to DNV GL (2018), the former should, "if possible, be based on a detailed schedule for the operation" and the latter "should be based on a reasonably conservative assessment of experience with same or similar tasks". This estimated maximum contingency contains a general uncertainty but does not include the uncertainty of the weather conditions. For a novel installation method with a floating vessel using earth-fixed heave compensation, the best that can be done would be to consider an operation period by means of a simulation or to use operation periods for offshore wind farms previously installed by other contractors. Also, it is advised to use a real conservative estimate for T_C for the first time using the new technology.

Given that T_{POP} and T_R for the proposed installation method are well below 72 hours and 96 hours respectively, it can be concluded that the operation is weather restricted. It should be investigated whether the assembly of the RNA on board of the vessel is defined as a part of the installation. This depends on the maximum allowed motions as given by the turbine manufacturer. According to DNV GL (2018), the operational limit, or OP_{LIM}, can then be defined. This operational limit is, amongst others, depending on limitations "based on experience with involved vessel" and "weather restrictions for equipment". This means that, if the vertical motion of the payload is the governing limit, proposed heave compensation system could increase OP_{LIM} and therefore improve operability.

Since there is uncertainty involved in the weather forecasting, the operational limit should be multiplied by a certain alpha factor α (DNV GL, 2018). The forecasted operational limit is now given by Equation 2.2.

$$OP_{WF} = \alpha \times OP_{LIM} \tag{2.2}$$

The factor α can be found in *DNVGL-ST-N001: Marine operations and marine warranty* and is depending on whether there is environmental monitoring, the operational limit in terms of significant wave height[1] H_S, T_{POP} and whether Load and Resistance Factor Design (LRFD) or Working Stress Design (WSD)[2] is used. The difference in values of the alpha factors is due to uncertainty in wave height.

Furthermore, it is stated by DNV GL (2018) that for active heave compensators, the efficiency (in terms of stroke and pay-in/out speed) of the heave compensator shall be multiplied by a safety factor of 0.9, and shall also not exceed an efficiency of 80%. For example, for a heave compensator with 95% efficiency, the lowest of 0.9 × 95% = 0.86% and 0.80% shall be used. This means that for an increase in operability according to DNV GL, it is not necessary to design a heave compensator with an efficiency higher than 90%. However, in practice, a higher efficiency is of course better.

In this research, the goal is not to perform a full operability analysis. The behaviour of the system is assessed for a given set of wave parameters. For these conditions, it is determined if earth fixed heave compensation reduces vertical motions of the payload and therefore could improve operability or simply improve the handling of the RNA. For the simulations, a JONSWAP wave spectrum (further discussed in section 2.3) is used with a significant wave height of 1.5 meter, a zero-up-crossing period of 7.5 seconds and a γ-factor of 3.3. These are typical values for the North Sea (DNV GL, 2019c). The direction of the waves is 180°, i.e. waves travelling from bow to stern. Wind and current are neglected since these are mostly resulting in horizontal motions of vessel and payload. However, it should be noted that a different vessel heading might be desired due to wind on the RNA during installation.

2.2. Heave compensation

In general, heave compensation can be split up in two types: passive heave compensation (PHC) and active heave compensation (AHC). On top of that, hybrid forms of these two types exist. This chapter explains the differences between active and passive heave compensation and discusses their performance.

2.2.1. Passive heave compensation

Passive heave compensators do not require energy to operate. For example, a load is connected via a system to the vessel. This system should work as a parallel spring-damper system. Figure 2.1 shows a simple example of such a passive heave compensator with a spring-damper system (Woodacre et al., 2015).

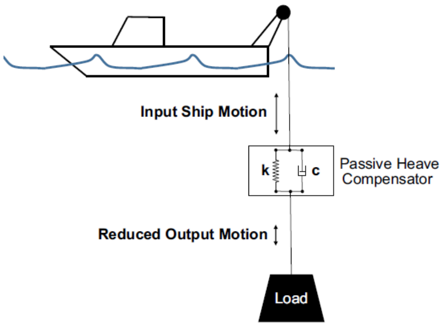

Figure 2.1: Example of a passive heave compensator (Woodacre et al., 2015).

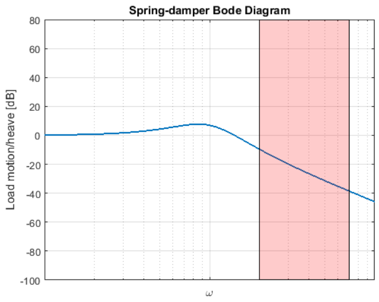

Figure 2.2: Typical bode diagrams of passive heave compensators.

The goal of this system is to reduce the ratio between heave amplitude of the load and heave amplitude of the crane tip. Figure 2.2 shows a qualitative bode diagram of a spring-damper system. The system works as a low pass filter, low frequencies of the vessel motion are transferred to the load almost directly. At the cut-off frequency, the motion of the load is amplified. In the higher frequencies, the ratio between the motion of the load and the heave motion of the vessel is below one. This means the motion of the load is less than the motion of the vessel itself. The properties of the system should be chosen in a way that the the amplification is well below one within the wave spectrum (shown by the red area in Figure 2.2).

---

[1] The significant wave height is defined as the average of the highest one-third of the waves.

[2] LRFD and WSD are design methods used within structural engineering, differences between these methods are not further discussed in this report.

Ormond (2011) patented a depth compensated passive heave compensator that acts as a spring-damper system, based on gas pressure and hydraulic fluid. The system is depicted in Figure 2.3. The compensator consists out of an accumulator, an actuator and a depth compensator. The piston in the actuator is connected to the load, the top end of the actuator is connected to the crane. The accumulator contains a high pressure nitrogen at the top, to maintain pressure in the lower chamber of the actuator which contains a high pressure oil. The upper chamber of the actuator is connected to the depth compensator with low pressure oil. The hydrostatic pressure of the water exerts a force on the piston in the depth compensator and therefore increases pressure in the top chamber of both actuator and depth compensator. In this way, the force exerted on bottom of the actuator piston is counteracted by the pressure in the top chamber of the actuator. Ormond (2011) claims the subsea passive heave compensator (SPHC) can operate in air and in water depths up to 10000 ft. The accumulator and the actuator work as a spring-damper system, with its stiffness as a function of the volume of gas in the actuator and the damping coefficient determined by multiple aspects, such as mechanical friction, geometry of the load and cable length (Woodacre et al., 2015). Since this information originates from a patent, numbers for the performance of this system are not available.

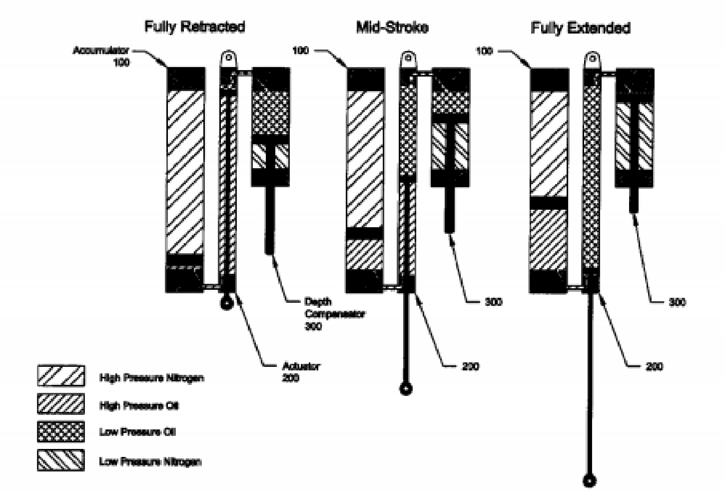

Figure 2.3: Depth compensated passive heave compensator (Ormond, 2011).

Figure 2.4: A passive heave compensator used offshore for transition piece installation (Cranemaster, 2020).

Another type of passive heave compensator is the nylon stretcher. This is a synthetic sling with visco-elastic properties. This can typically be used during deep water operations (DNV GL, 2019b). Advantage of passive heave compensators are that they can be used without having to make adjustments to the vessel and that they do not need an external power supply. One of the drawbacks of PHC's is that the performance is dependent of excitation frequency, i.e. the system responds differently for different sea states (Gu et al., 2013). This frequency dependent performance is a direct result of the system's physical properties as stiffness and damping coefficient. PHC's can have an efficiency up to 85% for heave motions over 4 m, but, for instance, an efficiency of only 40% for heave motions under 2 m (Gu et al., 2013). However, Hatleskog and Dunnigan (2006) state that the maximum efficiency of a passive heave compensator is roughly 80%. On top of that, a system like this requires extra lifting height when placed between the crane block and the load. Especially for installation of wind turbines, this is problematic since lifting height is one of the main limiting factors for current crane vessels. Furthermore, the performance of a PHC is limited by its stroke, i.e. the maximum distance that the piston in the actuator can travel.

2.2.2. Active heave compensation

Active heave compensators, on the other hand, do require energy as input. AHC's operate using closed loop control and the input is not necessarily limited to the heave motion of the ship. For example, feedback can be based on wave data or data from a load cell between the vessel and the load. Modern AHC's are equipped with actuators, either hydraulic or electronic, sensors and electronics (Woodacre et al., 2015). A disadvantage of AHC's is that the amount of energy needed, especially when lifting large masses, can be rather high (Nielsen,

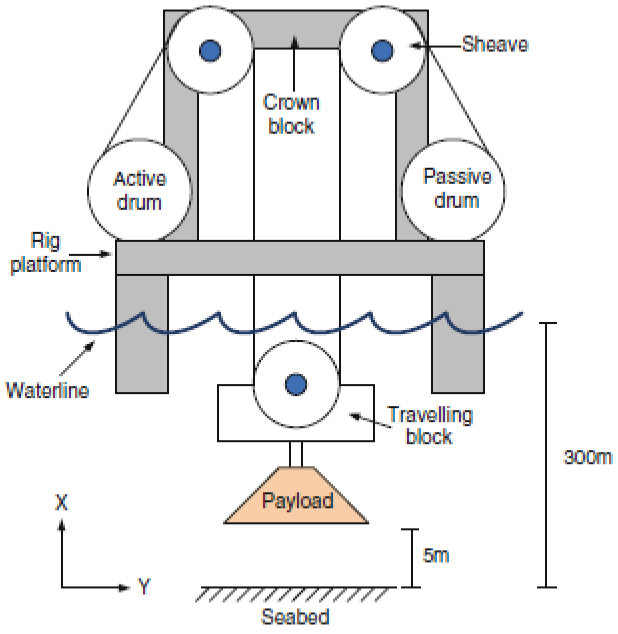

Figure 2.5: Type of active heave compensation (Gu et al., 2013).

2007). Electric AHC's are popular because of their high efficiency, however, using only an electric motor can be impractical compared to a hydraulic motor since an electrical motor with equal power output is large compared to a hydraulic one (Woodacre et al., 2015).
A simple example of an AHC is shown in Figure 2.5. The active drum recieves input from the sensors and subsequently reacts to the motions of the floating platform. In this way, the motions of the payload are reduced. Gu et al. (2013) states that the typical efficiency of an AHC is around 95%, i.e. the amplitude of the oscillations of the payload should be smaller than 5% of the vessel's heave amplitude.

Wang et al. (2018) compared a combined ship motion compensation (CSMC) to a direct motion compensation (DSMC) proposed by Barge Master, as shown in Figure 2.6. The latter compensates the heave, roll and pitch motions all by means of hydraulic cylinders. The former, shown in Figure 2.7, compensates only roll and pitch with hydraulic cylinders. The heave motion compensation is a separate system integrated in the crane. Although the CSMC only uses a maximum of 25% of the energy of the DSMC, the power needed for CSMC can still go up to 0.8 MW for a payload of 10 t. This is caused by the fact that in both systems the motion of the whole crane is compensated in roll and pitch direction, and for the DSMC also in heave direction. Considering the typical weight of wind turbines and the size of the cranes, both DSMC and CSMC seem unfeasible options.

Figure 2.6: Direct ship motion compensation (Barge Master, 2020).

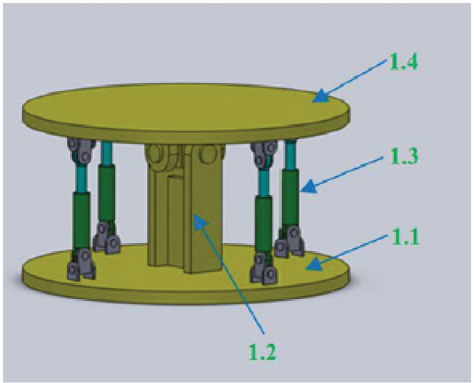

Figure 2.7: Combined ship motion compensation. 1.1: lower plate, 1.2: main support shaft, 1.3: hydraulic cylinder, 1.4: upper plate (Wang et al., 2018).

2.2.3. Passive versus active heave compensation

As mentioned earlier, the efficiency of a PHC is strongly dependent on the vessel's motion. Its performance reaches a maximum around 80% to 85%. AHC, on the other hand, can have efficiencies up to 95%. This means only 5% of the vessel's motion is transferred to the load. For example, a load hanging on a vessel that is heaving 1 m is only heaving 5 cm in case of a 95% efficient AHC. One of the drawbacks of AHC's is the amount of energy that is needed during operation, also the wear of wires around sheaves and drum is a disadvantage (Offshore Engineer, 2013). On top of that, AHC makes use of various control mechanisms. This creates a risk of sudden response of the heave compensation system when, for instance, the payload is set down. The investigation of an earth-fixed heave compensator, as discussed in this report, is not found in current literature. The concept of an earth-fixed heave compensator can be considered hybrid. In principle, the system is passive, but the constant tension winch (CTW) is an active component.

The full performance of proposed system is something that is not considered in this report. A total quantitative comparison can only be made when time-domain simulations are executed for all systems in various environmental conditions. The performance is calculated for a certain sea state, as discussed in section 2.1. The calculated performance can then be compared to the typical performance of active and passive heave compensators to say something about the potential of the novel concept.

2.3. Hydromechanics

Before using software that calculates vessel and payload motions, it is important to know what the underlying wave theory is that these computer programs use. At first, ship motions in general are discussed. Secondly, the modelling of waves and wave spectra is explained. At last, wave modelling software programs and how they are applied, are considered.

2.3.1. Ship motions and response amplitude operators

To say something about ship motions, first, the forces on a ship need to be determined. For linear behaviour, or relatively small motions, this is done in three separate steps as shown below (Naaijen, 2019). The forces of all three contributing parts are in the end summed up.

1. **Static equilibrium**. Both ship and water are not moving. Equilibrium exists between buoyancy and gravity. Equation 2.3 shows this relation in which ∇ represents the displaced volume of the ship.

$$-mg + \rho g \nabla = 0 \tag{2.3}$$

2. **Reaction forces**. In this situation, waves are still ignored and ship motions are prescribed. The forces experienced by the ship consist of a hydrostatic part and a hydrodynamic part. The former refers to additional or reduced buoyancy due to a difference in displaced volume. The latter is called the radiation force and refers to the forces that the ship experiences by radiating waves due to its own movement.

3. **Excitation forces**. This force also consists out of two parts. The first force is the Froude-Krilov force and resembles the force acted on the vessel by waves, assuming that the waves themselves are not influenced by the presence of the ship. The second force is the diffraction force and resembles the force the ship experiences due to reflection of waves.

To simplify, only heave motion is considered for now. The forces in the static equilibrium cancel out and are of no importance for the motions of the ship. For a pure heave motion, or motion in z-direction, Equation 2.4 shows the equation of motion. The hydrostatic reaction force is a function of the position in z-direction and is denoted by coefficient c_3. The index 3 indicates that it is the hydrostatic coefficient for heave motion. The coefficients a_3 and b_3 are related to the radiation force. Since the radiation force is a function of the ship's vertical acceleration and velocity, the coefficients are added mass and damping coefficients respectively. This is done in analogy with a simple spring-damper system. The Froude-Krilov force (F_{w3}) and diffraction force (F_{d3}) act as external forces and are placed at the right hand side of the equation.

$$(m + a_3)\ddot{z} + b_3\dot{z} + c_3 z = F_{w3} + F_{d3} \tag{2.4}$$

A vessel can be considered as a rigid body since the deflections of the vessel are significantly smaller than the motions of the vessel itself. On top of that, the vessel is not constrained; it is able to move in any direction. This means that the vessel in total must have six degrees of freedom (Greenwood, 2006). It moves in surge, sway, heave, roll, pitch and yaw direction. The first three motions are translational in respectively x-, y-, and z-direction. The last three motions are rotational around respectively x-, y-, and z-axis. Equation 2.5 shows the equation of motion in matrix form for all six degrees of freedom. In this equation, ζ_i is the position in direction i. For $i = 1,2,3$ the unit is m, for $i = 4,5,6$, the unit is rad. The mass plus added mass matrix $[\mathbf{m}+\mathbf{a}]$ consists of the mass of the ship on the first three diagonal entries and its moments of inertia on the last three diagonal entries. The other entries contain all added mass coefficients. The damping matrix $[\mathbf{b}]$ contains all damping coefficients and the stiffness matrix $[\mathbf{c}]$ contains all restoring coefficients. All matrices are 6 by 6. On the right hand side of Equation 2.5, the external forces are shown; forces for the translational degrees of freedom, moments for the rotational degrees of freedom.

$$[\mathbf{m}+\mathbf{a}]\begin{bmatrix}\ddot{\zeta}_1\\\ddot{\zeta}_2\\\ddot{\zeta}_3\\\ddot{\zeta}_4\\\ddot{\zeta}_5\\\ddot{\zeta}_6\end{bmatrix} + [\mathbf{b}]\begin{bmatrix}\dot{\zeta}_1\\\dot{\zeta}_2\\\dot{\zeta}_3\\\dot{\zeta}_4\\\dot{\zeta}_5\\\dot{\zeta}_6\end{bmatrix} + [\mathbf{c}]\begin{bmatrix}\zeta_1\\\zeta_2\\\zeta_3\\\zeta_4\\\zeta_5\\\zeta_6\end{bmatrix} = \begin{bmatrix}F_1\\F_2\\F_3\\M_4\\M_5\\M_6\end{bmatrix} \tag{2.5}$$

The calculation of the coefficients for a, b and c is an extensive process depending on the radiation potential and ship geometry. This is not considered in this report. Note that the use of dynamic positioning (DP) also contributes to the damping and stiffness matrix. The focus is on the calculation of the Froude-Krilov force. To determine this force, the pressure of the water has to be determined first. This is done by using Equation 2.6 (Naaijen, 2019). Note that the last term will yield a pressure that is of second order and can therefore be neglected in the linear approximation.

$$p = -\rho g z - \rho\frac{\partial\Phi}{\partial t} - \frac{1}{2}\rho(\nabla\Phi)^2 \tag{2.6}$$

To calculate the force, the pressure has to be integrated over the surface of the ship. For the linear approximation, this means integrating over the mean wetted surface of the ship, i.e. the surface that is under water in static equilibrium. In reality, of course, this surface is also a function of time. The integrals for determining the Froude-Krilov force are given by Equation 2.7 and Equation 2.8. In these equations, S stands for the mean wetted surface of the hull, p is the pressure, n is a normal vector perpendicular and pointing outward of the hull and r is a vector from the origin, or another point around the moments are to be calculated, to a location on the hull. The same integration should be done for the diffraction potential. In principle, this works the same as for the undisturbed wave potential, only the potential should now describe the reflected waves instead of the incoming. More details about the wave potential are given in Appendix A, however, the calculations regarding wave potentials are not discussed in this report.

$$\overline{F} = -\iint_S (p\cdot\overline{n})\,dS \tag{2.7}$$

$$\overline{M} = -\iint_S p \cdot (\overline{r} \times \overline{n}) dS \tag{2.8}$$

When the forces and moments acting on a vessel are determined, the vessels motions, ζ_1 until ζ_6 from Equation 2.5, can be calculated. When looking at only the heave motion again, the steady state motion of the vessel can be described by Equation 2.9 (Journée and Massie, 2001). In this equation, $\hat{\zeta_3}$ represents the amplitude of the ships heave motion, ω is the same frequency as the incoming wave, and $\epsilon_{\zeta_3,\zeta_a}$ is the phase difference between the movement of the ship and the incoming wave at the origin of the ship. The ratio between the amplitude of the motion of the ship and the amplitude of the incoming wave, $\frac{\hat{\zeta_3}}{\zeta_a}$, is called the response amplitude operator (RAO). The RAO exists for all six degrees of freedom and is not only a function of wave frequency ω, but also a function of the direction of the incoming wave. Typically, tables or graphs are used for the RAO and phase of a ship as a function of frequency. Each table or graph then represents the ship behaviour for a certain direction of the incoming wave.

$$\zeta_3(t) = \hat{\zeta_3} \cos(\omega t + \epsilon_{\zeta_3,\zeta_a}) \tag{2.9}$$

2.3.2. Waves

Figure 2.8 shows a time trace of a water level and the definition[3] of elevation η, wave height H and wave period T. The elevation is the water level at a given time, the wave height is the maximum difference in elevation within one period. The period, or downward zero-crossing period in Figure 2.8, represents the time between two successive downward crossings of the water elevation with the mean elevation. Figure 2.9 shows the definitions as used by DNV GL (2019a). Note that Figure 2.8 shows a time trace of a water elevation at a fixed point in space, whereas Figure 2.9 shows the wave profile in space at a fixed point in time.

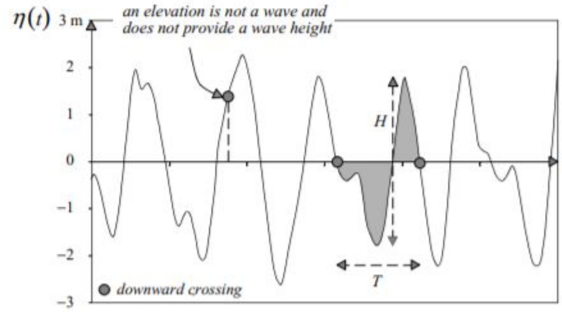

Figure 2.8: Example of a time trace of a wave elevation (Holthuijsen, 2007).

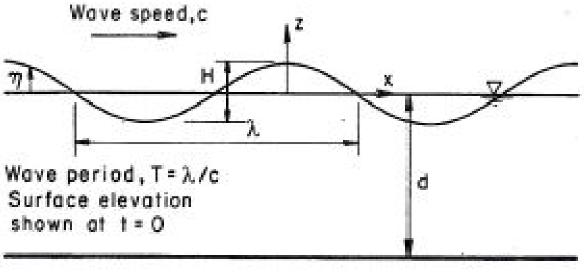

Figure 2.9: Terminology of a travelling wave (DNV GL, 2019a).

The elevation as a function of time can be expressed as a Fourier series as described in Equation 2.10 (Holthuijsen, 2007).

$$\eta(t) = \sum_{i=1}^{\infty} a_i \cos(2\pi f_i t + \alpha_i) \tag{2.10}$$

In which a_i is the wave amplitude, f_i the frequency and α_i the phase for each component i. Waves can be described as a summation of harmonic components, thus a spectrum can be used to describe the behaviour of waves at a certain location. This can be done by means of a variance density spectrum as defined in Equation 2.11 (Holthuijsen, 2007). The procedure for calculating such a spectrum for a given time trace of a wave elevation is not considered in this report.

$$E(f) = \lim_{\Delta f \to 0} \frac{1}{\Delta f} E\{\frac{1}{2}\underline{a}^2\} \tag{2.11}$$

In Equation 2.11, $\underline{a}$ is underlined to indicate that the wave amplitude is considered a random variable. An example of such a spectrum is shown in Figure 2.10. The reason why the variance $E\{\frac{1}{2}\underline{a}^2\}$ is chosen rather than, for instance, the expected value $E\{\underline{a}\}$ is that the energy of waves per unit surface is proportional to the variance. This relation is shown in Equation 2.12 and Equation 2.13. The average of the wave elevation

---

[3] Different sources use different symbols. For consistency, some symbols in this report are changed.

squared, or $\overline{\eta^2}$, is equal to the variance. Therefore, the energy density spectrum is equal to the product of the variance density spectrum, the water density and the gravitational acceleration.

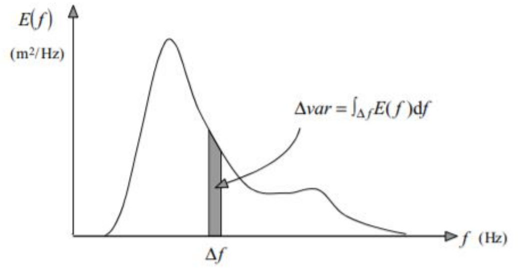

Figure 2.10: Example of a variance density spectrum (Holthuijsen, 2007).

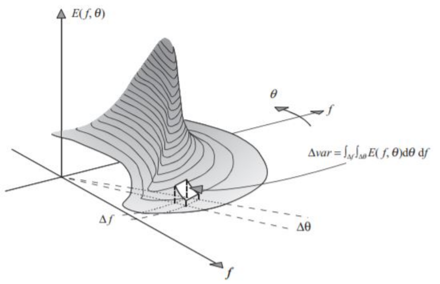

Figure 2.11: Example of a directional spectrum (Holthuijsen, 2007).

$$E_{total} = \rho g \underline{\overline{\eta^2}} \tag{2.12}$$

$$E_{energy}(f) = \rho g E_{variance}(f) \tag{2.13}$$

The variance density spectrum provides a full statistical description of the wave elevation. This means that all kinds of statistical characteristics can be calculated with this spectrum. These characteristics can call be expressed as a function of the spectrum's spectral moments. Equation 2.14 (Holthuijsen, 2007) shows how these spectral moments are calculated. In this equation, n has to be an integer. Furthermore, m_0 is called the zeroth order moment and m_2 is the second order moment of the spectrum.

$$m_n = \int_0^\infty f^n E(f)df \tag{2.14}$$

Two important statistical characteristics that can be calculated are H_{m0}, and T_0. The former represents the estimated significant wave height and has subscript m_0 to indicate that it is estimated from a spectrum rather than measured from a time trace. The latter is the mean zero-crossing period and represents the average time between two successive up or downward crossings with the mean water elevation. The same principle can also be used for other parameters than the wave elevation, this is discussed in chapter 3. The derivation of equations below is not considered in this report.

$$H_{m0} \approx 4 \cdot \sqrt{m_0} \tag{2.15}$$

$$T_0 = \sqrt{\frac{m_0}{m_2}} \tag{2.16}$$

So far, only unidirectional waves have been considered. In reality, ocean waves can be represented by the summation of harmonic components with not only different amplitudes, frequencies and phases but directions as well. This is shown in Figure 2.12. The surface elevation as a function of space and time of one of those components can be written as in Equation 2.17 (Holthuijsen, 2007).

$$\eta(x,y,t) = a\cos(\omega t - kx\cos\theta - ky\sin\theta + \alpha) \tag{2.17}$$

Note that Equation 2.17 now represents a propagating wave as a function of both time and space, whereas a component from Equation 2.10 only resembles an elevation as a function of time. Also, the frequency is now a radial frequency. Furthermore, θ represents the direction of the wave component, and k is the wave number, calculated by $2\pi/L$, in which L is the length of a wave.

In the same way as the spectrum is constructed for a unidirectional spectrum, a directional spectrum can be made, as shown in Equation 2.18. Again, the method to construct a spectrum from a time series of waves is not considered in this report. An example of such a directional spectrum is shown in Figure 2.11. It is also common to use the radial frequency for spectra. Described spectra are useful tools to describe the behaviour of a certain sea in a compact manner. The use of these spectra is considered in subsection 2.3.3.

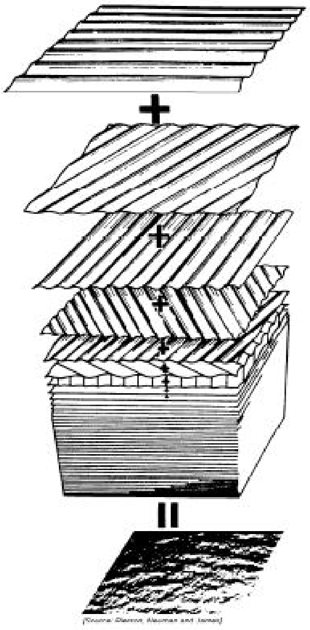

Figure 2.12: The sea surface can be described by a sum of regular waves (Journée and Massie, 2001).

$$E(f,\theta) = \lim_{\Delta f \to 0} \lim_{\Delta\theta \to 0} \frac{1}{\Delta f \Delta\theta} E\{\frac{1}{2}\underline{a}^2\} \tag{2.18}$$

2.3.3. Wave spectra

So far, only the behaviour of a vessel and wave spectra have been discussed seperately. When the RAO's and the wave spectrum are known, a response spectrum of the ship can be constructed according to Equation 2.19 (Journée and Massie, 2001). In this equation, $S_r(\omega)$ is the response spectrum of the ship, $\frac{\zeta_i}{\zeta_a}$ is the RAO for degree of freedom i and $S_\zeta(\omega)$ is the wave spectrum.

$$S_r(\omega) = \left|\frac{\zeta_i}{\zeta_a}(\omega)\right|^2 \cdot S_\zeta(\omega) \tag{2.19}$$

Wang et al. (2018) model the vessel motions as simple sinusoidal motions for heave, roll and pitch, while Gu et al. (2013) model the vessel motions only as a sinusoidal heave motion. Zhao et al. (2018, 2019) model multiple load cases with varying wave directions, irregular waves and correlated wind and wave conditions. The used spectrum is a Pierson-Moskowitz spectrum given in Equation 2.20 (DNV GL, 2019c). In which S_{PM} is the spectral density, H_s the significant wave height, ω the wave frequency and $\omega_p = \frac{2\pi}{T_p}$ the peak frequency.

$$S_{PM}(\omega) = \frac{5}{16} H_s^2 \omega_p^4 \omega^{-5} \exp\left(-\frac{5}{4}\left(\frac{\omega}{\omega_p}\right)^{-4}\right) \tag{2.20}$$

In this report, a JONSWAP spectrum is used with a peak shape parameter of $\gamma = 3.3$, which is typical for the North Sea (DNV GL, 2019c). A JONSWAP spectrum is basically a modified Pierson-Moskowitz spectrum, and is calculated as follows:

$$S_J(\omega) = A_\gamma \cdot S_{PM}(\omega) \cdot \gamma^r \tag{2.21}$$

Where:

$$A_\gamma = \frac{0.2}{0.065\gamma^{0.803} + 0.135} \tag{2.22}$$

$$r = \exp\left(-0.5\left(\frac{\omega - \omega_p}{\sigma\omega_p}\right)^2\right) \tag{2.23}$$

In these equations, ω_p is the peak frequency, $\sigma = 0.07$ for $\omega \leq \omega_p$ and $\sigma = 0.09$ for $\omega > \omega_p$.

2.3.4. Wave modelling software

To simulate ship motions, software is used. In this section four software programs are discussed. Also, the relevance of each program for the research of earth fixed heave compensation is discussed. Since there is some overlap of the different types of software, it sometimes is a matter of the engineer's preference what software to use.

- **aNySIM** is a hydromechanics tool developed by MARIN. The tool can be used to perform time domain analyses of, for example, ships moored to a quayside or buoy mooring but also for crane motions during installation work (MARIN, 2014). aNySIM also has the option to be coupled with bridge simulations in case of human interaction.

- **MOSES**, developed by Bentley Systems, is a tool specifically for modelling offshore installation and platform design. It can be used for both frequency and time domain simulations (Bentley Systems, 2018). The tool also provides diffraction analysis. In essence, a diffraction analysis is performed to determine all coefficients of the matrices mentioned in subsection 2.3.1. On top of that, MOSES can be coupled to Bentley SACS, which is structural solver widely used in the offshore industry. Although MOSES is a versatile program, within Heerema it is usually only used for transportation analysis, jacket launch and jacket upend analysis.

- **OrcaFlex**, developed by Orcina, is also a tool for hydromechanic modelling. OrcaFlex is wideley used in the offshore industry for, amongst others, installation, decommissioning and mooring analysis. It can model in both time and frequency domain, but is not able to perform a diffraction analysis. Orcina offers a module specifically designed for offshore wind (Orcina, 2020). This means detailed aerodynamic loads can be coupled with the hydrodynamic loads on the structure. For this research, however, wind loads are not considered.

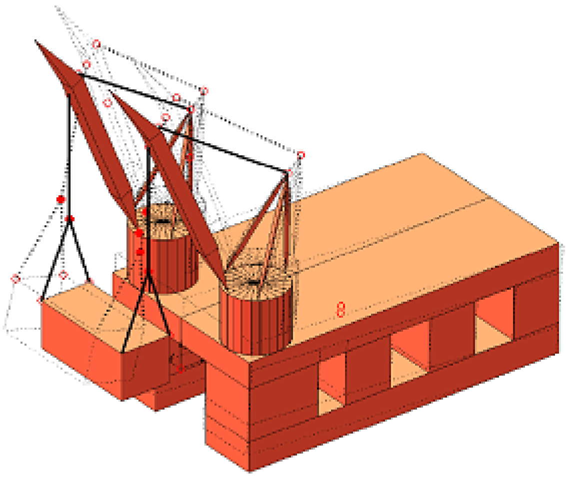

Figure 2.13: Mode shape for a dual crane lift with an SSCV in LiftDyn. Source: Heerema.

- **LiftDyn** is an in-house tool developed by Heerema to solve the equations of motions in the frequency domain. The program is able to solve systems consisting of rigid bodies that are connected to each other or fixed to the earth. These connections can be either springs, damper or hinges. Even though MOSES and OrcaFlex are able to do this as well, LiftDyn is within Heerema most popular for solving in the frequency domain.

In general, two types of analyses can be performed. A time domain analysis and a frequency domain analysis. In a time-domain analysis, the response of a system in time will be analyzed, whereas in a frequency-domain analysis the behaviour as a function of frequency is considered. In a timedomain analysis, non-linear hydrodynamic effects can be simulated, whereas in a frequency-domain analysis only linearized effects can be captured (DNV GL, 2019a). Normally, when behaviour of a system in case of extreme conditions is desired to investigate, such as the slamming of waves, a time-domain analysis is done. However, this comes at the price of generally longer computational time. Another advantage of a time-domain analysis is that transient effects can be seen. This is not necessarily desired, both Jiang et al. (2018) and Zhao et al. (2018), for example, mention that their time domain simulations only start after the effects of transients have disappeared. For a frequency-domain analysis only the steady state behaviour of a system can be analyzed. For this research, both frequency domain and time domain simulations are done. This is explained in chapter 4. WAMIT is used for the diffraction analysis of HLV Aegir with a standard operational draft of 9 m. Liftdyn is used in chapter 3 to determine global vessel and RNA motions in the frequency domain. At last, OrcaFlex is used for the time domain analysis. Both programs can easily be controlled by means of an application programming interface (API).

2.4. Structural modelling

2.4.1. Wires

The steel wire in the system can basically modelled in two ways. The first method is to consider the wire as a tensile bar. In this model, the bar is assigned a cross-sectional area A, a density ρ, the Young's modulus E, and a Length l (Spijkers et al., 2005). This type of model is shown in Figure 2.14 The displacement and stress are a function of x-coordinate and time. An advantage of this method, for example, is that the weight of the wire is realistically distributed over the full length of the wire. On top of that, external friction can be modelled as an external force acting on the wire. Zhao et al. (2019) use bar elements to model the crane wires for a feasibility study of offshore single blade installation by floating crane vessels.

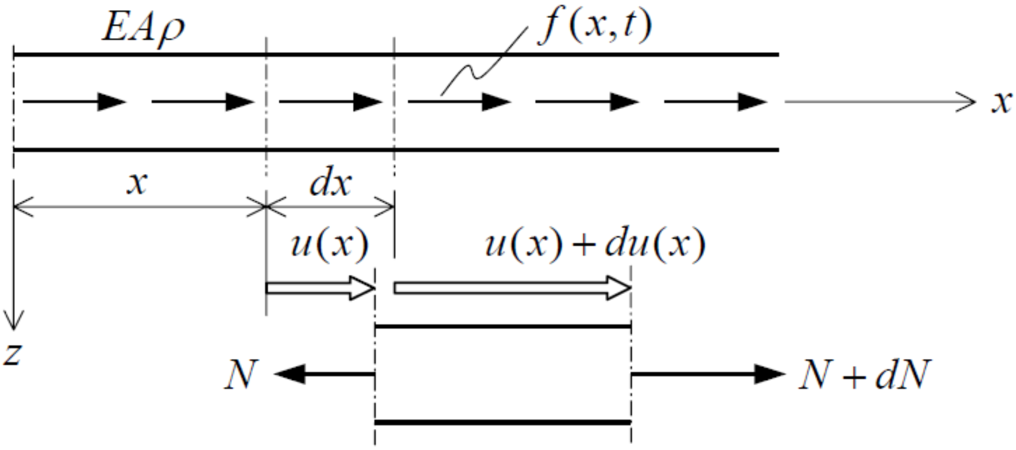

Figure 2.14: Tensile bar (Spijkers et al., 2005).

A simpler way of modelling wires is by means of a spring-damper combination. This is done by Gu et al. (2013) and Ren et al. (2018). Since the crane wires are relatively long, inertia is could play a significant role in the behaviour of earth fixed heave compensation. Therefore, a mass should be added to the model as well. An example of how this could be done is shown in Figure 2.15. The mass of the wire is modelled as a block at the end of that wire, the wire itself is modelled as a spring-damper combination.

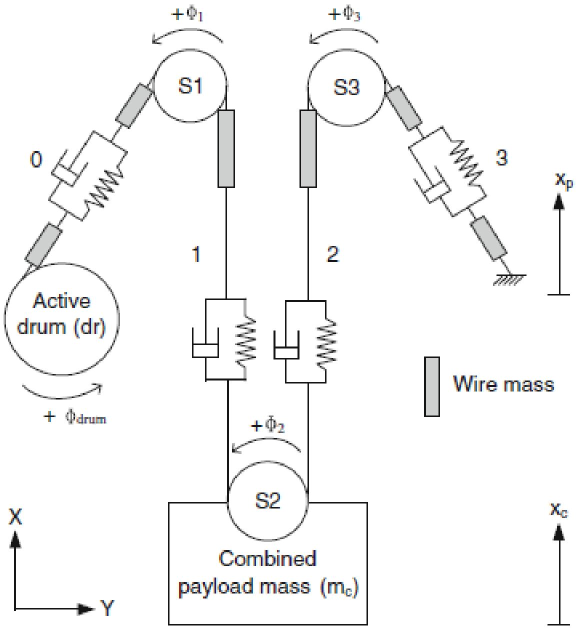

Figure 2.15: Model of an active heave compensation system (Gu et al., 2013).

This spring-damper model seems easy at first sight, since the stiffness of a wire is known in general. However, determining the damping of such a wire can be problematic. This damping consists of material damping and frictional damping between the multiple wires (Chaplin, 1991). Gu et al. (2013) use a damping coefficient of 10% of the spring coefficient[4] but states that this is only a rough estimate. Zhao et al. (2018, 2019) do the same, but use a value of 1%. Ren et al. (2018) also use a specific damping coefficient, but do not provide why this value is chosen. Another way to choose a damping coefficient is by looking at the critical damping. van der Valk (2017) uses Equation 2.24 to determine the damping coefficient of a steel wire but also mentions that damping in reality is a function of elongation amplitude, frequency and the history of wire vibrations.

$$b = \zeta b_{crit} = \frac{1}{\sqrt{1+(\frac{2\pi}{\delta})^2}} 2\sqrt{km} \tag{2.24}$$

In Equation 2.24, ζ is the dimensionless damping coefficient, b_{crit} the critical damping, δ is a logarithmic decrement which should, according to Chaplin (1991), be between 0.02 and 0.20 for multi-strand ropes. Furthermore, k and m stand for the wire's stiffness and mass respectively. For this research, stiffness-proportional damping is used. A sensitivity analysis for the damping value is performed in chapter 4.

2.4.2. Sheaves

The most simple way of modeling the sheaves would be to model them without inertia and friction, but for a large amount of sheaves of considerable size this is not deemed realistic. A simplified moment of inertia of a sheave around its rotating axis can be calculated according to Equation 2.25, when the sheave is considered as a simple disk or ring with inner radius R_1 and outer radius R_2. Sheaves are in general not shaped as a simple disk, therefore, it would be more accurate when the moment of inertia is calculated numerically by solving the integral of Equation 2.26. However, this the difference between this exact integral and the disk approximation is considered negligible. Gu et al. (2013) also model the moment of inertia of the sheaves, as if they are simple disks, according to Equation 2.25.

$$I = \frac{1}{2} m(R_1^2 + R_2^2) \tag{2.25}$$

$$I = \iiint_V \rho r^2 dV \tag{2.26}$$

2.4.3. Wire-sheave interaction

While the moment of inertia can be calculated relatively straightforward, the energy losses due to wire-sheave interaction are difficult to assess. First of all, there is two types of friction that occur and need to be distinguished. One being the bearing-pin friction and the other one being the friction between the sheave and the wire. Both types of friction result in a loss of tension in the wire that is bent over the sheave. Gu et al. (2013) model the bearing-pin friction as coulomb friction according to Equation 2.27, in which F_f is the frictional force, μ the friction coefficient between the bearing and the pin and N is the normal force between bearing and pin. This is only an approximation since kinetic friction would occur during rotation of the sheave, as mentioned by Gu et al. (2013).

$$F_f = \mu N \tag{2.27}$$

To calculate whether slippage occurs between the sheave and the wire, Gu et al. (2013) use Equation 2.28, which is known as the capstan equation or Eytelwein's formula. In this equation, μ_{wsh} is the friction coefficient between the wire and the sheave, and β is the angle of the wire around the sheave, which is equal to π in Figure 2.16. The forces in either part of the wire are denoted by W_{0umax} and W_{1u}. This formula can be used to determine the maximum friction before slippage occurs, but does not describe the behaviour when there is actual slippage. Also it should be born in mind that this formula does not take into account the diameter of both sheave and wire. Heller Jr (1970) proposed a modified equation, taking these two into account. However, both formulas do not take into account the rotation of sheaves.

$$W_{0umax} = W_{1u} e^{\mu_{wsh}\beta} \tag{2.28}$$

---

[4] By spring coefficient, the numerical value of the spring stiffness is meant. The unit of damping is Ns/m whereas the unit of stiffness is N/m. To obtain the correct unit for stiffness proportional damping, the stiffness should be multiplied by 1 s as well.

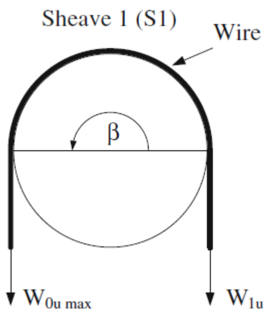

Figure 2.16: Illustration of Equation 2.28 (Gu et al., 2013).

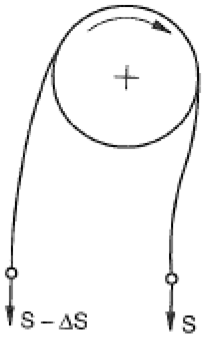

Figure 2.17: Wire bending over sheave (Feyrer, 2007).

Wire-sheave interaction might have a significant impact on the behaviour of the heave compensation system, but the effect is not known yet. Therefore, a sensitivity analysis is performed on the effect of the tensile losses on the system's behaviour. This is also of importance since objects in the offshore environment tend to suffer from corrosion which will most certainly increase the friction in sheaves. Nabijou and Hobbs (1994) concluded that the fatigue life of wires decreases with a decreasing D/d ratio. D being the sheave diameter and d the wire diameter. Although fatigue of the wires is not considered in this report, it should be taken into account when further designing earth-fixed heave compensation.

As mentioned before, a difference in tension occurs between the two sides of the wire when a wire moves over a sheave. This difference, or loss, is denoted by ΔS, as shown in Figure 2.17. The efficiency of the wire bending over a sheave is calculated by Equation 2.29.

$$\eta = \frac{S - \Delta S}{S} \tag{2.29}$$

Generally, the tensile force S in a wire is known. However, the frictional loss is not known yet and should be calculated. Feyrer (2007) states that the total loss of force in the wire consists out of 3 parts:

1. Loss due to wire bending over the sheave.
2. Loss due to friction in the bearing of the sheave.
3. Loss due to friction in the seal of the sheave bearings.

The total sheave friction yields:

$$\frac{\Delta S_{tot}}{d^2} = \frac{\Delta S_{wire}}{d^2} + \frac{\Delta S_{bear}}{d^2} + \frac{\Delta S_{seal}}{d^2} \tag{2.30}$$

The first term, which is based on empirical values, can be calculated according to Equation 2.31. In this equation, d stands for the diameter of the wire, D for the diameter of the pulley. The constants c_0 and c_1 are depending on the wire properties and are provided by Feyrer (2007).

$$\frac{\Delta S_{wire}}{d^2} = \left(\frac{D}{d}\right)^{-1.33} \cdot \left(c_0 + c_1 \cdot \frac{S}{d^2}\right) \tag{2.31}$$

In Equation 2.32, μ_{bear} is the friction coefficient of the bearing, d_{axle} the diameter of the axle and θ_d the deflection angle of the wire around the sheave. Feyrer (2007) states that according to SKF[5] $\mu_{bear} \leq 0.0024$ and friction resistance is $q = 0.01$ N/mm. However, higher values are found by Müller (1990) for the friction resistance. In chapter 4 is calculated whether this is significant for the total friction loss. In this research, Equation 2.30 is used to calculate the total losses due to wire-sheave interaction. For this calculation, the load is assumed to be constant. The validity of this assumption is also assessed in chapter 4.

$$\frac{\Delta S_{bear}}{d^2} = \frac{\mu_{bear} \cdot d_{axle}}{D} \cdot \frac{S}{d^2} \cdot 2 \cdot \sin\frac{\theta_D}{2} \tag{2.32}$$

---

[5] SKF, Svenska Kullagerfabriken is a bearing manufacturer.

$$\frac{\Delta S_{seal}}{d^2} = \frac{2 \cdot \pi \cdot q \cdot d_{axle}^2}{D \cdot d^2} \tag{2.33}$$

2.4.4. Payload

Modelling of the payload, which is suspended in the crane, can be done in various ways. The easiest way to do so is to model the payload as a point mass, as done by Wang et al. (2018). In this way, the mass has no moment of inertia. Zhao et al. (2019) modelled a wind turbine blade as a rigid body with six degrees of freedom. Since the payload is relatively stiff compared to the rigging arrangement and other wires, this is an acceptable approach. Note that not only the payload itself needs to be modelled, but also the crane block which is used to lift it since it has a significant mass. In LiftDyn, as discussed in subsection 2.3.4, the payload will be modelled as a block with a mass and moments of inertia connected to the crane block via a straightforward rigging arrangement of three lower and three upper slings. The crane block is modelled as a point mass. In the OrcaFlex model, the effect of the heave compensation system is of interest at first. Therefore, the RNA, spreader frame and the crane block are modelled as one rigid block. In a later stage, the actual rigging arrangement and spreader frame can be modelled separately. Normally, a payload is connected to the crane via horizontal tugger lines as well. This is done to prevent the payload of having excessive pendulum motions. The tugger lines normally have a relatively low tension and are positioned more or less horizontal which means that the effect of the lines on the heave compensation system is expected to be limited. To simplify modelling, the payload will be constrained in OrcaFlex in such a way that only vertical motions for the payload are allowed. For a more detailed response calculation, realistic tugger behaviour needs to be implemented in the OrcaFlex model.

2.4.5. Constant tension winch

Proposed heave compensation system uses a constant tension winch to keep the transmission on board of the vessel in equilibrium, see section 1.3. A value for the load will be set to the constant tension winch, if the load varies from this value, the winch will pay in or out to maintain the same load value (SMI Offshore, 2020). YMV (2019) provides constant tension winches for towing purposes with capacities varying from 5 up to 100 tonnes. The capacity of these constant tension winches is important for dimensioning the transmission of earth-fixed heave compensation. In the OrcaFlex model, constant tension winch is modelled as a pure constant tension. Inertia and control mechanisms of the winch are in this model not taken into account.

2.5. Delineations and assumptions

Below is summarized under what assumptions the research is done. Furthermore, the delineations of this research are listed.
Assumptions:

- All bodies are considered rigid. The mass of the crane block is 35 t, the RNA is 625 t and the spreader frame is assumed to have a mass of 60 t. This last mass is approximately 10% of the to be lifted mass and considered acceptable according to Heerema Marine Contractors (2016). A straightforward rigging arrangement is designed based on stock sling information, provided by Heerema, to resemble realistic stiffness properties.
- All wires are assumed to act as spring-damper combinations. Stiffness values are provided by manufacturers, the effect of damping is investigated by a sensitivity analysis.
- The rotating lever arm is considered rigid, having a mass of 50 t.
- The seabed is considered rigid.
- The sheaves in the model are modelled as disks with an inner and outer radius.
- No stick-slip of the sheave around the axle occurs.
- The simulations are executed using a JONSWAP wave spectrum with a significant wave height of 1.5 m and a zero-crossing-period of 7.5 s, the gamma-factor is 3.3 and the heading of the waves equals 180°. These are typical conditions for the North Sea (DNV GL, 2019c).
- The properties of HLV Aegir are determined for a water depth of 60 m and a vessel draft of 9 m. The latter is the normal operational draft of HLV Aegir.
- The tension in the wires, excluding the earth fixed wire, is assumed to be constant. This results in an absolute loss that in principle does not change over time and can be calculated according to the formula presented by Feyrer (2007).
- Instead of modelling the tugger lines, a constraint is added to the model. This constraint allows the payload to travel solely in vertical direction.
- The RNA that is used in the model is based on a representative 10 MW offshore wind turbine for which the properties have been provided by HMC.

Delineations:

- The goal is not to perform a full operability analysis. Instead, the behaviour of the system is assessed for a specific load case to show the potential of proposed concept.
- With HLV Aegir's current crane setup, the lifting height of the auxiliary crane block is not enough to install this type of turbine, although upgrades of the crane are already at the drawing board at Heerema. The 750 t capacity auxiliary crane block of HLV Aegir is used in the model due to the relatively easy reeving plan.
- The purpose of this thesis is to assess the behaviour of the heave compensation system rather than designing a full heave compensation system.
- The additional operational aspects for making the earth-fixed connection, and the connection itself are not considered.

3

Motions during Regular Installation

To understand which motions should be reduced, it is important to know the RNA motions without a heave compensation system. In this chapter, modelling choices for the vessel and its payload are discussed. Secondly, the motions of the RNA are calculated in the frequency domain.

3.1. Vessel modelling

3.1.1. Hull

The equations of motion of a vessel can be written as shown in Equation 3.1. The mass matrix [**m**] consists of the mass of the ship on the first three diagonal entries and its moments of inertia on the last three diagonal entries. The added mass matrix [**a**] contains the added mass coefficients. The damping matrix [**b**] contains the damping coefficients and the stiffness matrix [**c**] contains the restoring coefficients. The matrices are 6 by 6. On the right hand side of Equation 3.1, the external forces are shown. Forces for the translational degrees of freedom, moments for the rotational degrees of freedom. These external forces consist of the froude-krilov forces and the diffraction forces. The mass matrix, the damping matrix and the external forces are all dependent of wave frequency and wave direction. A diffraction analysis has been conducted to calculate the hydrodynamic database containing all these frequency and wave dependent matrix coefficients using WAMIT. A water depth of 60 meters is used for this analysis, which is assumed to be a a reasonable water depth for offshore turbines in the coming years. The draft is assumed to be 9 meters, this is the standard operational draft for HLV Aegir.

$$[\mathbf{m}+\mathbf{a}]\begin{bmatrix}\ddot{\zeta}_1\\ \ddot{\zeta}_2\\ \ddot{\zeta}_3\\ \ddot{\zeta}_4\\ \ddot{\zeta}_5\\ \ddot{\zeta}_6\end{bmatrix}+[\mathbf{b}]\begin{bmatrix}\dot{\zeta}_1\\ \dot{\zeta}_2\\ \dot{\zeta}_3\\ \dot{\zeta}_4\\ \dot{\zeta}_5\\ \dot{\zeta}_6\end{bmatrix}+[\mathbf{c}]\begin{bmatrix}\zeta_1\\ \zeta_2\\ \zeta_3\\ \zeta_4\\ \zeta_5\\ \zeta_6\end{bmatrix}=\begin{bmatrix}F_1\\ F_2\\ F_3\\ M_4\\ M_5\\ M_6\end{bmatrix} \tag{3.1}$$

3.1.2. Crane

In reality, the crane boom, the mast and the suspension wires are not rigid bodies but have a certain stiffness. However, for simplicity, the crane boom and mast are modelled as rigid bodies. To take the mast and crane boom stiffness into account, an equivalent stiffness is used for both hoist wires and suspension wires. This can be seen in Figure 3.1. Table 3.1 shows the amount of wires, the diameter, the equivalent Young's Modulus and the total equivalent stiffness. Internal research within Heerema has that the error using this approximation is lower than 10%. The crane can be set to a certain slew angle, of which the definition is shown in Figure 3.5. Lengths for the suspension wires and hoist wires can be chosen in order to attain the right boom angle, lifting height and radius.

The crane block consists from top to bottom out of the sheavehouse, stem and hook, but is modelled as a block. The crane boom is connected to the crane boom via two wires to the crane boom. In reality, the reeving consists of 6 wires, but for modelling purposes this is modelled as 2 wires with equivalent stiffness. The length of the hoist wires is 4 meters and considered to be long enough to obtain enough clearance between the crane block and crane boom, also for the situation in which heave compensation is used.

Item	n	d	E_{eq}	EA_{eq}
Suspension wires	38	72 mm	$10.5\ \text{kN/mm}^2$	$1.62 \cdot 10^6$ kN
Hoist wires	6	72 mm	$40\ \text{kN/mm}^2$	$9.77 \cdot 10^5$ kN

Table 3.1: Equivalent stiffness values for Aegir mast crane.

3.2. RNA and rigging arrangement

The RNA properties are presented in Table 3.2 and are based on a representative offshore wind turbine of 10 MW, of which the properties are provided by Heerema. Although the blades are not displayed in the figures, they are part of the assembly and included in the properties. An overview of the dimensions and the locations of the lift points is given in Appendix B.

Parameter	**Value**	**Unit**
L_x	20.5	m
L_y	9.6	m
L_z	11.3	m
m	625	t
CoG_x	4	m
CoG_y	0	m
CoG_z	-1.27	m
I_{xx}	$1.80 \cdot 10^8$	kg m^2
I_{yy}	$1.10 \cdot 10^8$	kg m^2
I_{zz}	$1.10 \cdot 10^8$	kg m^2

Table 3.2: RNA properties.

The proposed rigging arrangement for lifting the RNA consists out of 3 lower slings, 3 upper slings and a spreader frame to prevent the introduction of horizontal loads in the nacelle. This is a configuration often used for wind turbine installation. The spreader frame, rather than the nacelle itself, withstands the horizontal loads caused by the upper slings. The mass of the spreader frame is assumed to be 60 t, roughly 10% of the total RNA mass. The mass of the slings is neglected in this analysis. The properties of the slings, as shown in Table 3.3 are chosen in such a way that the following conditions are met:

- RNA and spreader frame tilt are almost tuned to zero[1]
- A minimum clearance of 3 meters between nacelle and spreader frame
- A minimum rigging angle of 60 degrees with respect to the spreader frame, as recommended by Heerema Marine Contractors (2016)
- Unfactored loads in the slings are around 40% to 60% of the sling´s safe working load (SWL). This is not a direct requirement according to Heerema's standard criteria (Heerema Marine Contractors, 2016), but chosen to have enough capacity when safety factors are used to represent realistic sling properties.

The stiffness as presented in Table 3.3 is calculated by multiplying the effective Young's Modulus of a steel cable times the effective area of the sling. The effective Young's modulus is one third of the Young's modulus of steel, i.e. 70 GPa, the effective section area is equal to 44% of the nominal section area of the sling (Heerema Marine Contractors, 2018b).

---

[1] Although Heerema's guidelines provide a maximum tilt of 2%, lengths are tuned to minimize the tilt to only 0.023% .

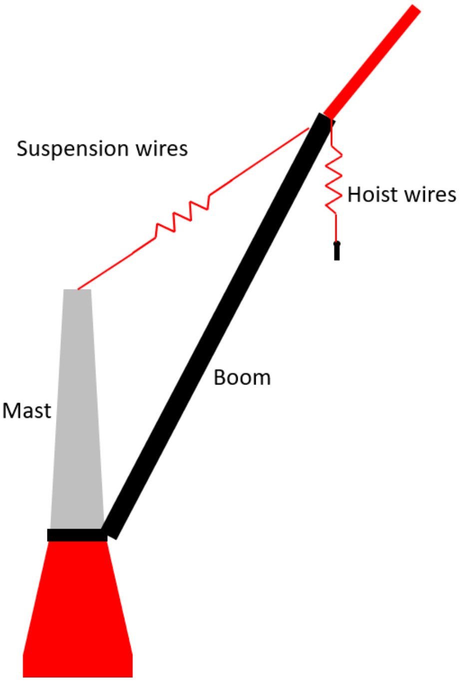

Figure 3.1: Equivalent crane stiffness.

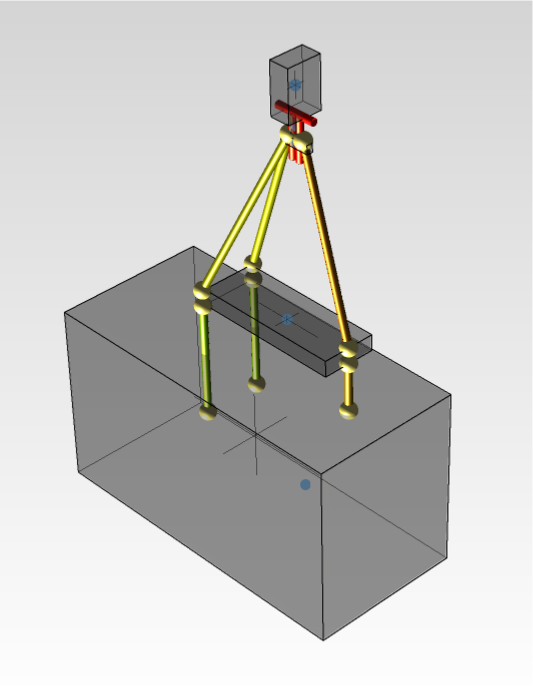

Figure 3.2: RNA lifting arrangement.

Item	Length [m]	Diameter [mm]	SWL [t]	EA [kN]
Upper sling 1	11.4	210	700	$1.07 \cdot 10^6$
Upper sling 2	12.2	150	300	$5.44 \cdot 10^5$
Upper sling 3	12.2	150	300	$5.44 \cdot 10^5$
Lower sling 1	3.00	210	700	$1.07 \cdot 10^6$
Lower sling 2	7.05	150	300	$5.44 \cdot 10^5$
Lower sling 3	7.05	150	300	$5.44 \cdot 10^5$

Table 3.3: Sling properties for RNA lift.

3.3. Liftdyn

When the vessel hull, crane, crane block, spreader frame and RNA are coupled, the system is complete. This total system is shown in Figure 3.4. The total set of equations for the combined system can be solved in the frequency domain. Solving these equations is done using Liftdyn, Heerema's in-house validated frequency domain solver for linear hydrodynamic problems. In this program, one can solve equations of motion for rigid bodies, which are connected via springs, dampers or hinges and excited by external forces (Heerema Marine Contractors, 2018a).

In principle, the hydrostatic spring matrix [**c**] in Equation 3.1, is a function of vessel geometry. However, to control the position of the vessel, the vessel uses dynamic positioning (DP) during operations. Although the exact behaviour of the DP system is not of importance for this matter, the the position of the vessel should be controlled to some extent. The values of Table 3.5 are used by Heerema to obtain realistic natural periods for the horizontal vessel motions. The values for the stiffness in surge, sway and yaw direction due to dynamic positioning can easily be added to the hydrostatic spring matrix. These values are respectively added to coefficients $c_{1,1}$, $c_{2,2}$ and $c_{6,6}$[2]. The wave direction is defined as shown in Figure 3.3. Conventional names for these waves are *head waves* (180°), *following waves* (0°) and *beam waves* (90° and 270°).

---

[2] The coefficients i and j in $c_{i,j}$ denote a coupling between two motions. $c_{i,j}$ relates to a restoring force in direction i due to motion in direction j. The same holds for damping and added mass coefficients.

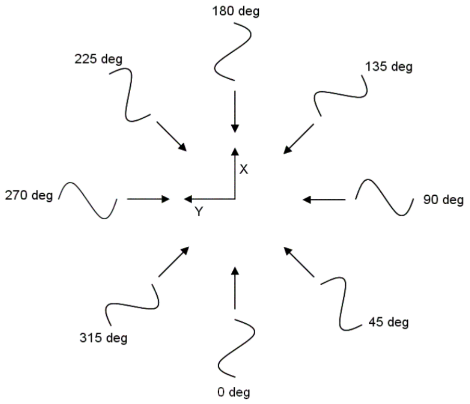

Figure 3.3: Wave direction definition.

The following wave properties are used for the frequency domain analysis:

- Spectrum type: JONSWAP
- Significant wave height: H_s = 1.5 m
- Peak period: T_p = 9.64 s (T_z = 7.5 s)
- Wave directions: θ_{wave} = [0°,45° ... 315°]
- Wave spreading: No

The diffraction analysis, as discussed in subsection 3.1.1, is based on linear wave theory. This theory does not take into account viscous forces on a floating structure. Generally, this is not a problem for modelling a vessel since the viscous forces are relatively small compared to the wave (reaction) forces. However, when looking at the roll motion of vessels, such as HLV Aegir, the frictional forces of the water on the hull are significant. To take this loss of energy into account, an additional roll damping is added to the damping matrix [**b**] at coefficient $b_{4,4}$. The value of this additional roll damping is shown in Table 3.5. Table 3.4 shows all connection in the Liftdyn model.

Body	Inertia	Connected to	Via connector
Aegir	Mass Moment of inertia Added mass (ω,θ_{wave})	Earth	Spring matrix (including DP springs) Damping matrix (ω,θ_{wave})
Crane boom	Mass Moment of inertia	Aegir	Hinge Suspension wire
Crane block	Mass Moment of inertia	Crane boom	Hoist wire
Spreader frame	Mass Moment of inertia	Crane block	Upper rigging
RNA	Mass Moment of inertia	Spreader frame	Lower rigging

Table 3.4: Liftdyn model.

Parameter	Value	Unit
Surge stiffness	100	kN/m
Sway stiffness	200	kN/m
Yaw stiffness	200000	kNm/rad
Roll damping	870000	kNm/rad

Table 3.5: Additional stiffness due to dynamic positioning and roll damping.

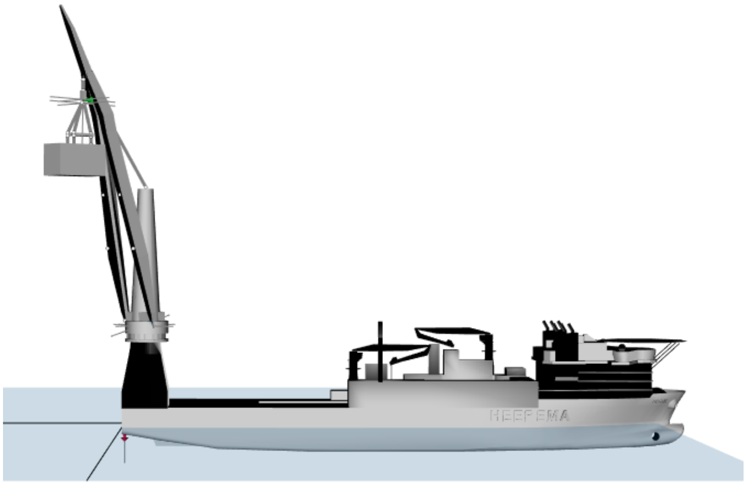

Figure 3.4: Aegir model.

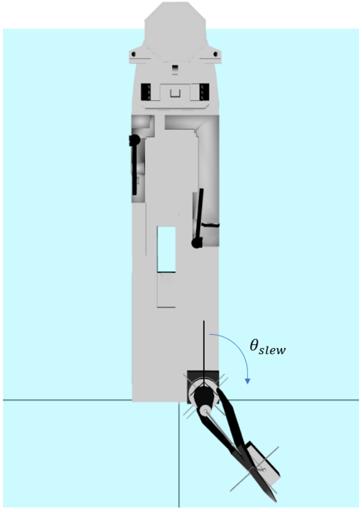

Figure 3.5: Slew angle definition.

3.4. Response amplitude operator: RNA

For the vertical motion of the RNA, RAO's are calculated in Liftdyn. For this calculation, a slew angle of $\theta_{slew} = 90°$ is used. Figure 3.5 shows how this slew angle is defined. Figure 3.6 and Figure 3.7 show the RAO's. Although the concept of RAO's is readily discussed in section 2.3, a quick explanation is given again. The graph should be interpreted as follows. Consider the vessel subjected a simple sinusoidal wave or *Airy* wave. This wave has a certain amplitude and frequency and excites the system with the same frequency. In a linear system, the response of the system for each degree of freedom has the same frequency but often a different amplitude and phase shift. The RAO's provide the ratio between the amplitude of the incoming wave and the amplitude of the vertical motion of the RNA as a function of both frequency and wave direction. For clarity, the graphs are split up in Figure 3.6 and Figure 3.7.

It can directly be seen that the vertical RNA motions are significantly amplified at frequencies around 0.35 rad/s and 0.63 rad/s, except for following and head seas. These peaks are caused by natural frequencies of the system with mode shapes in which roll motion of the vessel is dominant. The peaks are especially high for wave directions of 90° and 270°. This can be explained by the the fact that the vessels response in roll direction is significantly higher for waves from these directions. The effect of pitch motions of the vessel is less visible in these RAO's, which is contrary to expectations at first. For following and head seas, one would expect to observe large vertical RNA motions due to vessel pitch motions. Although pitch motions of the vessel are largest for 0° and 180° waves, they result in relatively low vertical RNA motions. This effect of pitch motions is expected to be bigger for a slew angle of 180°, since the horizontal distance between the RNA and the centre of the vessel is larger. For this same slew angle, the effect of vessel roll motion is expected to be lower due to the smaller horizontal distance between RNA and centre of the vessel. For some wave directions, a small peak can be seen around 0.48 rad/s. This is the frequency at which the vessel's pitch motion is largest. The vessel barely moves at frequencies above 1.5 rad/s, therefore, the vertical response of the RNA in that frequency range is also negligible.

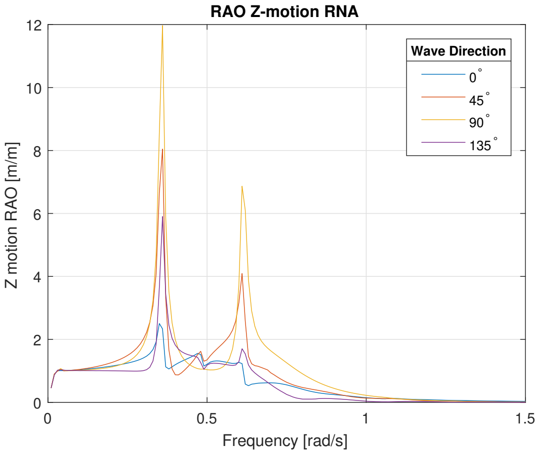

Figure 3.6: RAO of Z-motion of RNA for 0° – 135° waves.

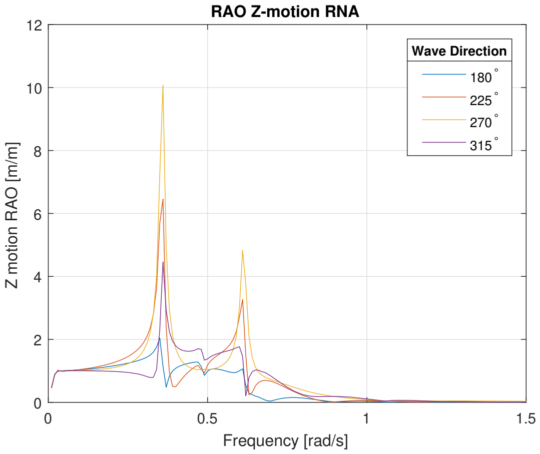

Figure 3.7: RAO of Z-motion of RNA for 180° – 315° waves.

3.5. Spectral response

In the previous section, the behaviour of the vertical motions of the RNA has been discussed as a function of wave direction and frequency. In order for the system to be excited at a certain frequency, waves should also be present at that specific frequency. The spectrum that is used in this research is a JONSWAP spectrum with a significant wave height of 1.5 m and a mean zero-crossing period of 7.5 s, which is a typical sea state for the North Sea (DNV GL, 2019c), see section 3.3 for more details. It is needless to say that other wave spectra do occur at this location, however, for the purpose of this research only one specific sea state is chosen. This spectrum is displayed in Figure 3.8. More details about wave spectra are given in section 2.3.

The spectral response can be calculated according to Equation 2.19 (Journée and Massie, 2001). In this formula, the spectral response of a system is calculated by multiplying the RAO squared with the wave spectrum.

$$S_r(\omega) = \left|\frac{\zeta_i}{\zeta_a}(\omega)\right|^2 \cdot S_\zeta(\omega) \tag{3.2}$$

Energy is present in the given wave spectrum at frequencies higher than 1.5 rad/s, however, as mentioned before, the RAO's of the vertical RNA motion approach zero in this frequency range. This means that the response will also approach zero in this frequency range. For clarity, the range of the graphs is reduced to 0 - 1.5 rad/s. Also, the amount of wave directions is reduced to give a better overview.

In section 2.3 is explained how the significant wave height can be obtained by calculating the zeroth order spectral moment of that spectrum. For a response spectrum, as calculated in Equation 3.2, the same calculation can be done (Journée and Massie, 2001). The only difference is that not the significant wave height is calculated, but a significant double amplitude (SDA) of the motion that is considered. The SDA is defined as the average value of the highest one-third of the response double amplitudes and is calculated as follows:

$$SDA = 4 \cdot \sqrt{m_{0,r}} \tag{3.3}$$

In this equation, the spectral moment $m_{0,r}$ is given the additional subscript r to indicate that this is the spectral moment of the response spectrum and not the wave spectrum.

Figure 3.8 shows the graphs of the wave spectrum, the RAO's and the response spectrum. The first thing that can be seen is that the first peak of the RAO's is not present in the response. This is the result of absence of waves at this frequency in the used wave spectrum. The second observation is that the response depends on the incoming wave direction. The spectral response can be used to quantitatively compare the responses for different wave directions. The SDA is something that can be calculated from this spectrum.

For operability calculations, it is convenient to show the SDA as a function of the peak period of the spectrum and the significant wave height. This is shown in Figure 3.9. These graphs show the SDA of a motion for a JONSWAP spectrum with peak period T_p and a significant wave height of 1 m. Such a graph is calculated in the following way:

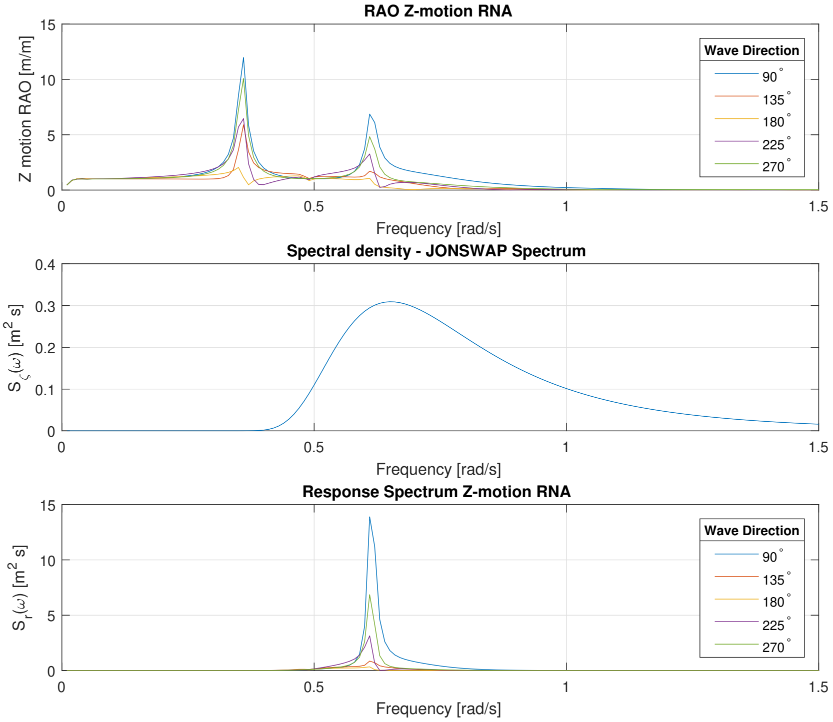

Figure 3.8: RNA Z-motion RAO, wave spectrum, and RNA Z-motion response spectrum.

- A JONSWAP spectrum is generated for a certain peak period T_p, and a significant wave height of 1 m. Such wave spectra are displayed in Figure 3.10.
- The spectral response is calculated for this specific wave spectrum according to Equation 3.2.
- The SDA of this response spectrum is calculated via Equation 3.3
- Above steps are repeated for a range of peak periods and wave directions.

The SDA of the Z-motion of the RNA can now be calculated directly, using the response graphs in Figure 3.9. For example, consider 90° waves, and a wave spectrum with a peak period of 12 s and a significant wave height of 1.2 m. The blue graph in Figure 3.9 shows that the Z-motion response is 2 m/m. The SDA for given sea state is thus $2 \cdot 1.2m = 2.4$ m. In principle, the SDA response graph can be calculated for every significant wave height. Since linear behaviour is considered in the frequency domain, output (response) scales with the same factor as input (significant wave height). Therefore, it is convenient to display the response per meter significant wave height. Such a graph is also called a unit response graph.

The behavior that was observed in Figure 3.8, is again seen in Figure 3.9. The response spectrum showed that that the 90° waves resulted in the largest peak, 180° waves showed the lowest. The same is seen in the unit response graph. For the mean-zero crossing period of 7.5 s (which corresponds[3] to a peak period of approximately 9.6 s), 90° waves result in the biggest response, 180° waves in the lowest response. This time, however, it can immediately be seen that the motions for the 180° waves are lowest for all considered peak periods. No matter what the peak period of the waves is, head seas will always result in the smallest vertical RNA motions for given vessel configuration. This is also expected since the RAO of the vertical RNA motion was generally the lowest for this wave direction.

A general trend that is observed is that the SDA of the vertical RNA motion tends to increase for wave spectra with increasing peak period. On top of that, the peaks that are clearly seen for the 90° and 270° around the peak periods of 10 s and 18 s correspond to the natural frequencies with roll motion dominated mode shapes.

---

[3] The peak period T_p and mean zero-crossing period T_z are related wave spectrum parameters. For a JONSWAP spectrum with $\gamma = 3.3$, $T_p = 1.2859 T_z$ (DNV GL, 2019c)

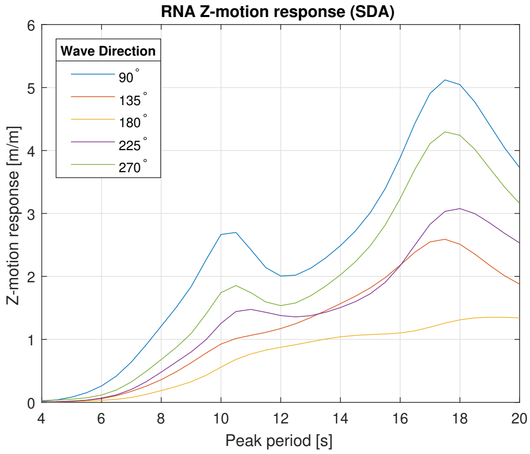

Figure 3.9: Unit response of Z-motion of the RNA

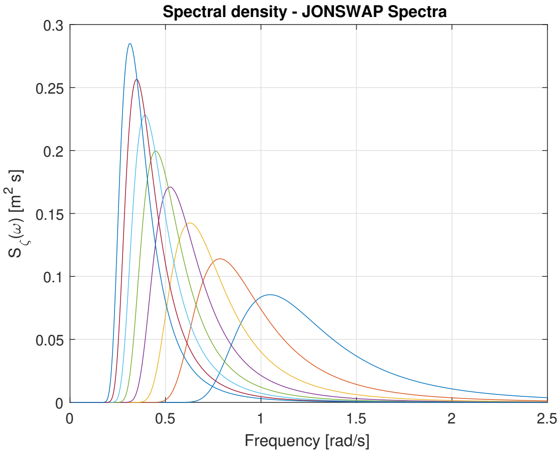

Figure 3.10: JONSWAP spectra for different peak periods.

3.6. Crane block, spreader frame and RNA motions

The analysis that is done for the RNA is also performed for the crane block and the spreader frame. This time, only for 180°. In the previous section was shown that this wave direction resulted in lowest vertical RNA motions. Figure 3.11 shows the RAO's of the vertical motion for the RNA, spreader frame and crane block and their response spectra for a JONSWAP spectrum with a mean zero-crossing period of 7.5 s and a significant wave height of 1.5 m. Figure 3.12 shows the unit response of the vertical motion of the same bodies, for JONSWAP spectra with peak periods varying from 4 to 20 s.

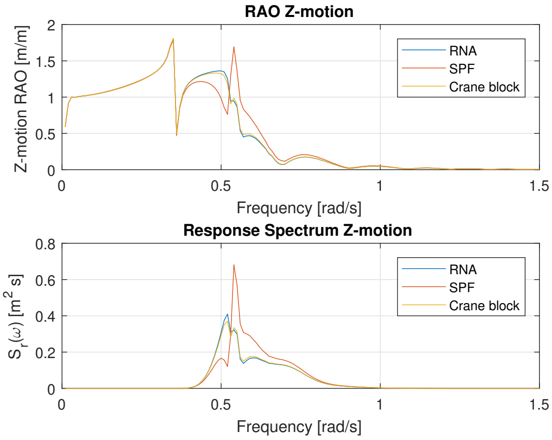

Figure 3.11: RAO and response spectrum for RNA, spreader frame and crane block Z-motion for 180° waves.

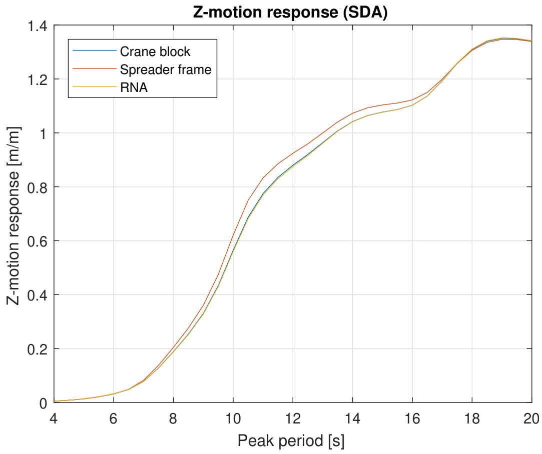

Figure 3.12: Unit response of Z-motion of the RNA, spreader frame and crane block for 180° waves.

It can be seen that the SDA of the spreader frame is somewhat bigger for spectra with peak periods approximately between 7 and 17 s, whereas the responses of the RNA and crane block do not differ much. The average difference between the SDA of the spreader frame and the RNA is 3.3%, whereas the average difference between the crane block and RNA is only 0.07%. Modal analysis shows that a mode shape is present in which the spreader frame oscillates vertically between the crane block and the RNA. This unfavorable motion is a result of the combination of sling stiffness and spreader frame weight. In this analysis, the properties of the simplified rigging arrangement are determined from a static analysis and standard guidelines, as discussed in section 3.2. In reality, however, a dynamic analysis would be performed for such lifts in order to prevent such oscillations. In the following chapters, the RNA, spreader frame and crane block are modelled as a single mass. This is considered to be acceptable since the focus of this research is on the vertical motions of the RNA. If detailed analyses would be performed in a later stage, the crane block, spreader frame and RNA should be modelled separately. Not only should this vertical behaviour be investigated, also the horizontal motions should be considered to make sure no unfavorable pendulum motions will occur.

4

Model Verification

In this chapter, the OrcaFlex model is built up step by step simultaneously with analytical solutions. The goal of the analytical solution is twofold. First, it gives insight in the physics of the system. Secondly, some of the modelling choices that are made in OrcaFlex can be verified with this analytical solution.

4.1. Stage 1

For the first modelling step, a simple 1-dimensional system, as represented in Figure 4.1, is considered. In this model, the lever arm hinges at the left hand side, and its hinge has a prescribed vertical motion $u(t)$. The same prescribed motion is given to the sheaves. In reality, these sheaves can rotate and therefore new degrees of freedom would be introduced. However, for now, the sheaves are assumed to be frictionless, to have no inertia and to have an infinitely small radius, without bending losses in the wires. This means the sheaves are solely in place to change the direction of the earth-fixed wire and there still is only one degree of freedom, θ_{lever}. On top of that, no losses occur due to bending of the wire around the sheaves. The seabed is assumed to be completely rigid. The beam is considered to be a prismatic beam with its centre of gravity in the middle. The 3 wire segments (14, 15 and 16) are modelled as 1 wire with equivalent stiffness and damping. The stiffness of the earth-fixed wire is based on the 100 mm diameter Oceanmax 35 (Oceanmax, 2014), which is normally recommended as a hoisting wire. For springs and dampers in series, Equation 4.1 and Equation 4.2 hold.

$$\frac{1}{k} = \frac{1}{k_{14}} + \frac{1}{k_{15}} + \frac{1}{k_{14}} \tag{4.1}$$

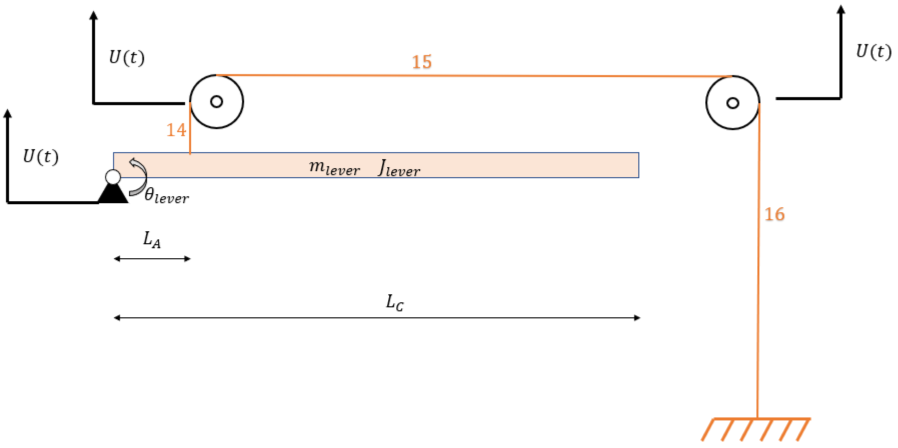

Figure 4.1: Modelling stage 1.

#	DoF	Unit	Parameter	Value	Unit	Parameter	Value	Unit
1	θ_{lever}	rad	m_{lever}	50.000	kg	l_{16}	66.5	m
			J_{lever}	$3.75 \cdot 10^6$	$\text{kg} \cdot \text{m}^2$	k_{14}	$2.41 \cdot 10^8$	N/m
			L_A	2	m	k_{15}	$2.88 \cdot 10^7$	N/m
			L_C	15	m	k_{15}	$1.09 \cdot 10^7$	N/m
			l_{14}	2.1	m	k	$7.64 \cdot 10^6$	N/m
			l_{15}	25.1	m			

Table 4.1: Degrees of freedom and parameter values for modelling stage 1.

$$\frac{1}{c} = \frac{1}{c_{14}} + \frac{1}{c_{15}} + \frac{1}{c_{14}} \tag{4.2}$$

The equation of motion for this single degree of freedom function can be calculated using Lagrange's equation[1] (Greenwood, 2006). Other methods, such as the *displacement method* (Spijkers et al., 2005), can also be used to obtain equations of motion. However, using Lagrange's equation is considered most suitable for problems in which motions are coupled due to hinges, which is the case in this situation. Equation 4.3 shows the linearized equation of motion for stage 1.

$$J_{lever} \cdot \ddot{\theta}_{lever}(t) + L_A^2 \cdot c \cdot \dot{\theta}_{lever}(t) + L_A^2 \cdot k \cdot \theta_{lever}(t) = \frac{1}{2} \cdot L_C \cdot m_{lever} \cdot g + c \cdot L_A \cdot \dot{u}(t) + k \cdot L_A \cdot u(t) \tag{4.3}$$

Or, in a more generalized form:

$$M\ddot{\theta}_{lever}(t) + C\dot{\theta}_{lever}(t) + K\theta_{lever}(t) = F_{static} + F_{dynamic} \tag{4.4}$$

In which the following expressions are substituted:

$$\begin{aligned} M &= J_{lever} \\ C &= L_A^2 \cdot c \\ K &= L_A^2 \cdot k \\ F_{static} &= \frac{1}{2} \cdot L_C \cdot m_{lever} \cdot g \\ F_{dynamic} &= c \cdot L_A \cdot \dot{u}(t) + k \cdot L_A \cdot u(t) \end{aligned} \tag{4.5}$$

The vertical prescribed motion is harmonic, $u(t) = A \cdot \sin(\omega t) = A \cdot \text{Im}(e^{i\omega t})$. For a linear system, the response is also an harmonic motion (Cool, 2006). This response, however, can have a different amplitude and a phase difference with respect to the prescribed motion or external force.

Assuming that statically $\theta_{lever} = 0$, the solution yields:

$$\theta_{lever}(t) = \text{Im}(\hat{\theta}_{dyn} e^{i\omega t}) \tag{4.6}$$

With $\hat{\theta}_{dyn}$ being the complex amplitude of the lever arm motion. This complex amplitude can be found by substituting Equation 4.6 in Equation 4.4 and rearranging. The complex amplitude is:

$$\hat{\theta}_{dyn} = A \cdot \frac{k \cdot L_A + i\omega \cdot c \cdot L_A}{-\omega^2 \cdot M + i\omega \cdot C + K} \tag{4.7}$$

Equation 4.7 contains both phase and amplitude of the response motion. The response amplitude can be calculated by taking the absolute value of Equation 4.7 and dividing by the input amplitude A. This is shown in Equation 4.8 and is in essence the same as the RAO's described in section 2.3. The unit of this value is rad/m, it denotes ratio between the lever arm amplitude and the amplitude of the prescribed vertical motion as a function of frequency. In the next section, this unit is transformed from rad/m to deg/m.

---

[1] In this method, a so called *Lagrangian function* is defined, a function of a system's potential and kinetic energy. Using this function and Lagrange's equation, the equations of motion of a multi-degree of freedom system can be obtained. How this should be done is not discussed in this report.

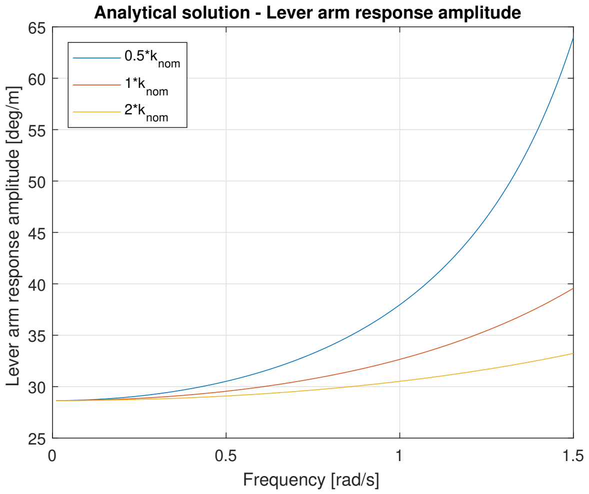

Figure 4.2: Response amplitude of lever arm for stage 1 without damping.

$$\frac{\theta_{dyn,a}}{A} = \left| \frac{k \cdot L_A + i\omega \cdot c \cdot L_A}{-\omega^2 \cdot M + i\omega \cdot C + K} \right| \tag{4.8}$$

4.1.1. Wire stiffness

Figure 4.2 shows the response amplitude of the lever arm as calculated by Equation 4.8. This calculation is done for the nominal stiffness, as given in Table 4.1, and for half and twice this stiffness while keeping the inertia of the beam the same. It can be seen that the stiffness of the system has a large influence on the response of the lever arm. This difference basically shows a shift of the natural frequency peak. The stiffer the system, the higher the natural frequency and the lower the response in the low frequency range. The stiffness of the system is not solely determined by the stiffness of the wire, it is the relative stiffness that determines the behavior. The undamped natural frequency of the system for the nominal stiffness is calculated by $\sqrt{\frac{K}{M}}$ and equals 2.85 rad/s according to the analytical solution for the nominal stiffness. It is also clear that the system cannot be analyzed quasi-statically for this frequency range.

As a quick and easy check, this modelling step is also done in OrcaFlex and shows an undamped natural frequency of 2.86 rad/s. The difference of approximately 0.3% is considered acceptable and can be explained by the linearization that OrcaFlex performs around the static state of the system. The lever arm in OrcaFlex is not at an exact horizontal position at equilibrium which results in small error in the frequency domain analysis.

4.1.2. Wire damping

Within Heerema, there are no specific damping coefficients known for the crane wires. A wire damping coefficient could be calculated by performing a decay test, as explained by Feyrer (2007). However, not one value can be found for the wire since the damping is, amongst other things, dependent of the mean stress in the wire. van der Valk (2017) mentions that wire damping also depends on amplitude, frequency and history of the wire's vibration. As mentioned in subsection 2.4.1, values varying from 0.01% up to 10% were found in the literature for stiffness-proportional wire damping. Note that the unit of damping is Ns/m, whereas the unit of stiffness is N/m. To obtain the correct unit for stiffness-proportional damping, the stiffness should be multiplied by 1 s. Choosing a value for the stiffness-proportional damping seems arbitrary but Figure 4.3 and Figure 4.4 show that in the difference in response is limited. Within the considered frequency range, the maximum difference between response for a situation with and without damping is only 1%. This difference is found for the highest stiffness-proportional damping value found in literature. For modelling stage 1, the difference in response for the different damping values is considered negligible when using stiffness-proportional wire damping values in the range that is found in literature. The same assessment is performed for modelling stage 3 in subsection 4.3.1.

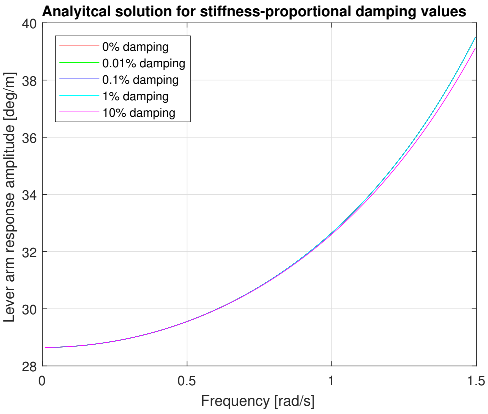

Figure 4.3: Lever arm response for various stiffness-proportional damping values.

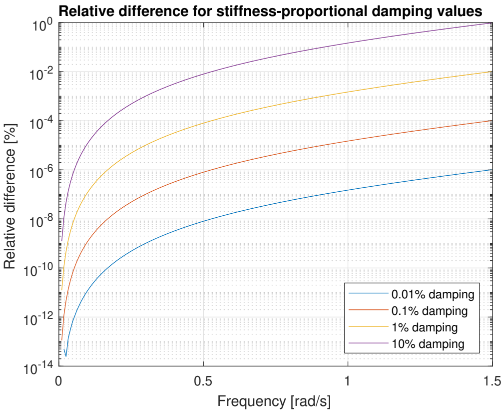

Figure 4.4: Relative difference of lever arm response for various stiffness-proportional damping values.

4.2. Stage 2

For stage 2, as seen in Figure 4.5, the following items are added. $F_{payload}$ and F_{ctw} acting as a constant force over time and sheave 13 and 14 including rotational inertia. By adding the sheaves, two new degrees of freedom are added to the system. Table 4.2 shows all parameters used for the calculations in stage 2.

#	DoF	Unit	Parameter	Value	Unit	Parameter	Value	Unit
1	θ_{s13}	rad	J_{lever}	$3.75 \cdot 10^6$	$\mathrm{kg \cdot m^2}$	l_{16}	66.5	m
2	θ_{s14}	rad	m_{lever}	$50 \cdot 10^3$	kg	k_{14}	$2.41 \cdot 10^8$	N/m
3	θ_{lever}	rad	L_A	2	m	k_{15}	$2.88 \cdot 10^7$	N/m
			L_B	12	m	k_{16}	$1.09 \cdot 10^7$	N/m
			L_C	15	m	k	$7.64 \cdot 10^6$	N/m
			l_{14}	3	m	$F_{payload}$	$1.18 \cdot 10^3$	kN
			l_{15}	25.1	m	F_{ctw}	$7.36 \cdot 10^3$	kN
			J_{s13}	418	$\mathrm{kg \cdot m^2}$	J_{s14}	418	$\mathrm{kg \cdot m^2}$

Table 4.2: Degrees of freedom and parameter values for modelling stage 2.

For modelling purposes, the wire is modelled as a *winch* in OrcaFlex. This means that the wire can only pass over points of interest that have no radius or friction. If necessary, the sheave inertia and losses due to wire sheave interaction have to be modelled differently.

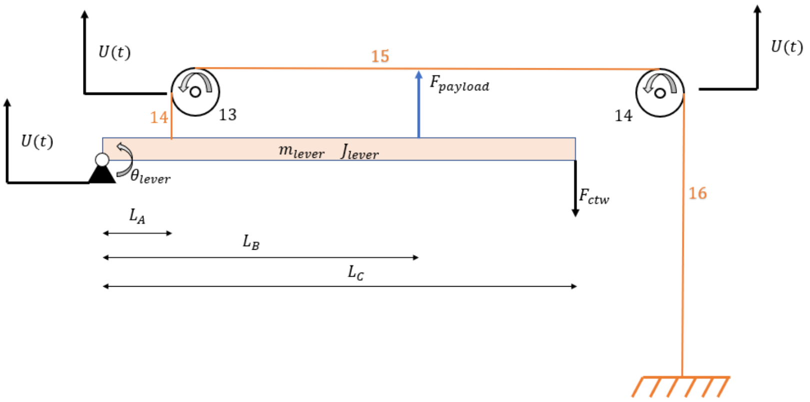

Figure 4.5: Modelling stage 2.

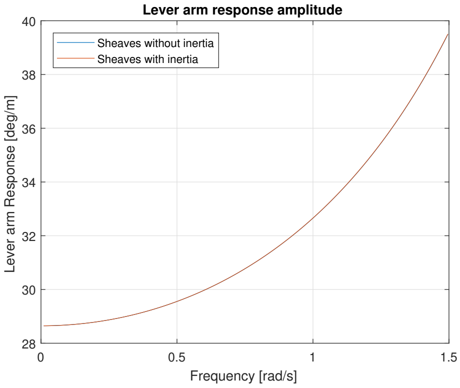

Figure 4.6: stage 2: the effect of sheave inertia on lever arm response.

4.2.1. Simplified analytical solution - sheave inertia

To determine whether the inertia of sheave 13 and 14 have to be modelled at all, the analytical solution of the system is calculated for sheaves with and without inertia. The response of the lever arm with parameters as given in Table 4.2 is shown in Figure 4.6. For given frequency range, the maximum relative error that is made by neglecting the inertia of the sheaves is 0.03%. The average relative error made is 0.009%. The error made for given parameters is considered acceptable. This error, however, depends on chosen parameter values. The two main design parameters that are likely to change in a later design stage are the mass of the lever arm and the wire stiffness.

Figure 4.7 shows that the maximum relative error and average relative error made when neglecting the sheave inertia are 0.047% and 0.012% respectively, when increasing the lever arm mass significantly by a factor of 2. Although it is not likely that the lever arm mass would increase with a factor 2, the maximum relative and average relative error are still acceptable. When the stiffness is reduced by 50%, the maximum relative error and average relative error become 0.094% and 0.023% respectively. Again, this is unlikely to happen but still contains an acceptable error.

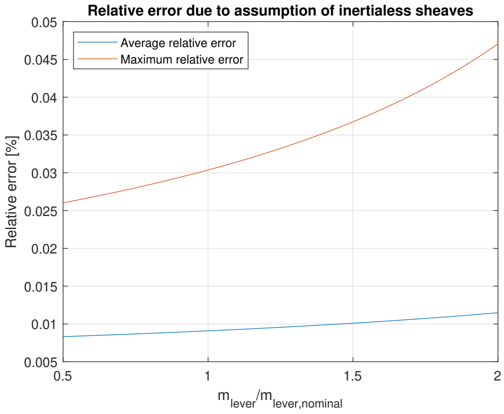

Figure 4.7: Relative error of lever arm response due to assumption of inertialess sheaves as a function of lever arm mass.

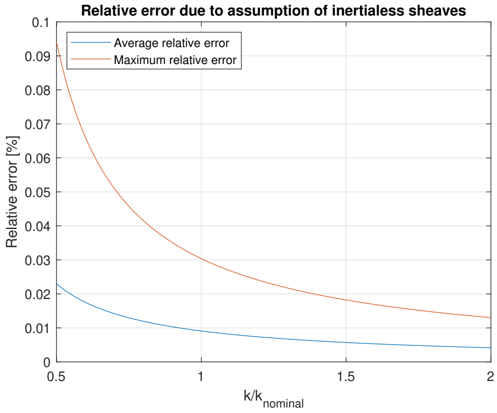

Figure 4.8: Relative error of lever arm response due to assumption of inertialess sheaves as a function of wire stiffness

For a reasonable range of lever arm masses and wire stiffnesses, it is shown that the inertia of sheave 13 and 14 can be neglected. Nevertheless, the combination of a big increase of leaver arm mass and a big decrease in wire stiffness could result in significant errors made by neglecting the sheave inertia. In this case, a new assessment should be executed to determine whether the error is acceptable.

The losses due to the sheave friction and the wire that is bent over the sheaves is neglected for now. These losses depend on the force in the wire, which is not yet known. This is considered in a later stage. It is expected that these losses are smaller than the losses in the crane due to the relatively large number of sheaves in the reeving and crane boom.

4.3. Stage 3

The drawing and a table with all degrees of freedom for modelling stage 3 are given in Appendix C. Sheaves, crane wire and reeving and the crane block are added. The masses of the RNA and the spreader frame are added to the mass of the crane block, as discussed in chapter 3. This combined mass is referred to as payload.

4.3.1. Wire damping

In subsection 4.1.2 it was concluded that the influence of wire damping was limited for the values found in literature. The same assessment has been done for stage 3. Figure 4.9 and Figure 4.10 respectively show the response of the crane block and the relative differences between the damped and undamped system. The maximum error is found at 1.5 rad/s for 10% stiffness proportional damping. This error is considered acceptable since the damping is likely to be lower and the maximum error occurs at the very end of the relevant frequency spectrum where motions are hardly present. The spikes that are observed at the low frequencies for low damping are the result of numerical errors in Matlab. In the rest of the report, a stiffness-proportional damping value of 1% is used.

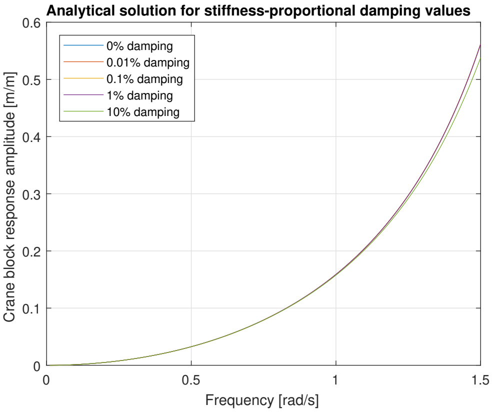

Figure 4.9: Stage 3: crane block response for various stiffness-proportional damping values.

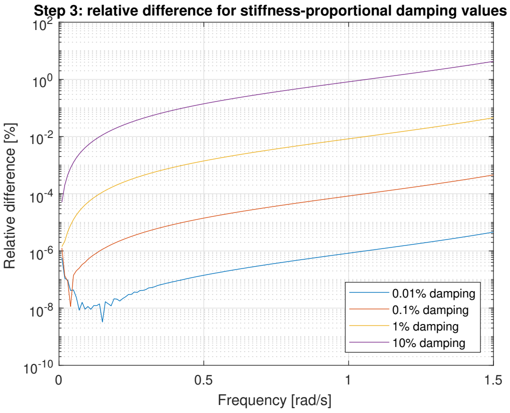

Figure 4.10: Stage 3: relative difference of lever arm response for various stiffness-proportional damping values.

4.3.2. Simplified analytical solution - sheave inertia and wire mass

In subsection 4.2.1 it was concluded that the inertia of the sheaves for modelling stage 2 can be neglected. A same analysis is performed for modelling stage 3. In Figure 4.11 and Figure 4.12 can immediately be seen that there is a difference in response for both lever arm and payload when neglecting the wire and sheave inertia. The average relative errors are 3.3% and 22.9% respectively. The effect of neglecting the inertia on the response of the lever arm can be considered acceptable, however, the error made for the crane block response is significant and cannot be neglected.

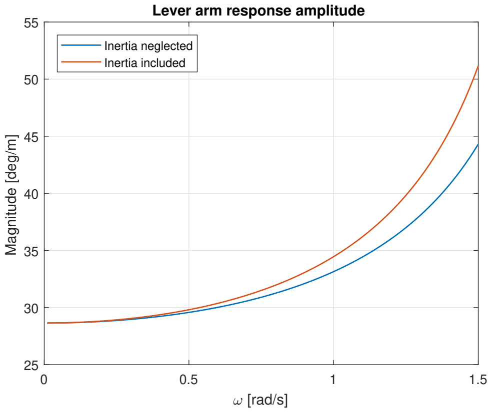

Figure 4.11: Response amplitude of lever arm for stage 3 for with and without inertia of wire and sheaves.

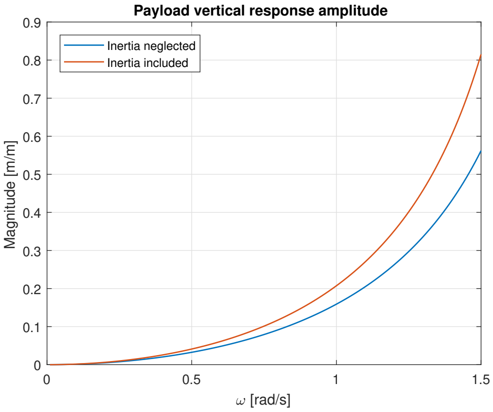

Figure 4.12: Vertical response amplitude of crane block for stage 3 for sheaves with and without inertia of wire and sheaves.

The moment of inertia of a sheave can be modelled by means of a single point mass having only translational motions. First, the equivalent inertia of that block needs to be calculated. The moment of inertia of a point mass m rotating around an axis with radius r, equals $m \cdot r^2$. The equivalent inertia, or m_{eq} should be calculated such that it reflects the moment of inertia of the sheave and the wire segment that is connected to the sheave, this is also shown in Figure 2.15. This is done by using Equation 4.9. Secondly, the equivalent inertia is not attached to the sheave, but to a wire between two sheaves. For modelling purposes, a clever spot would be between sheave 9 and 10. The wire in between sheave 9 and 10 is horizontal, and there is enough space for the block to travel when it is modelled in the middle between sheave 9 and 10. On top of this, the influence of gravity on this block is minimized for this location, since it travels along a horizontal path. Figure 4.14 shows how this looks like in OrcaFlex.

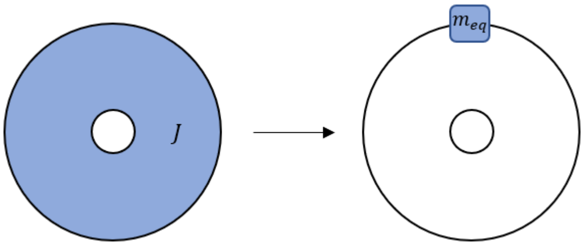

Figure 4.13: Moment of inertia modelled as equivalent inertia.

$$m_{eq} = \frac{J}{r^2} + m_{wire} \tag{4.9}$$

Adding up all equivalent inertias to find the total equivalent inertia would be incorrect. Due to the reeving, the sheaves have different response amplitudes which need be considered in order to represent a correct equivalent inertia. In Figure 4.15 can be seen that sheave 1 to 6 all behave differently, whereas sheave 7 to 12 behave similarly. This is caused by the reeving of crane wire. Small differences in response of sheave 7 to 12 occur due to wire stiffness.

Since the equivalent inertia is added to a block that is solely able to move in one translational direction, the relative motion of the sheaves with respect to the equivalent inertia block is of interest. Again, an analytical solution has been found for modelling stage 3, this time including the equivalent inertia block between

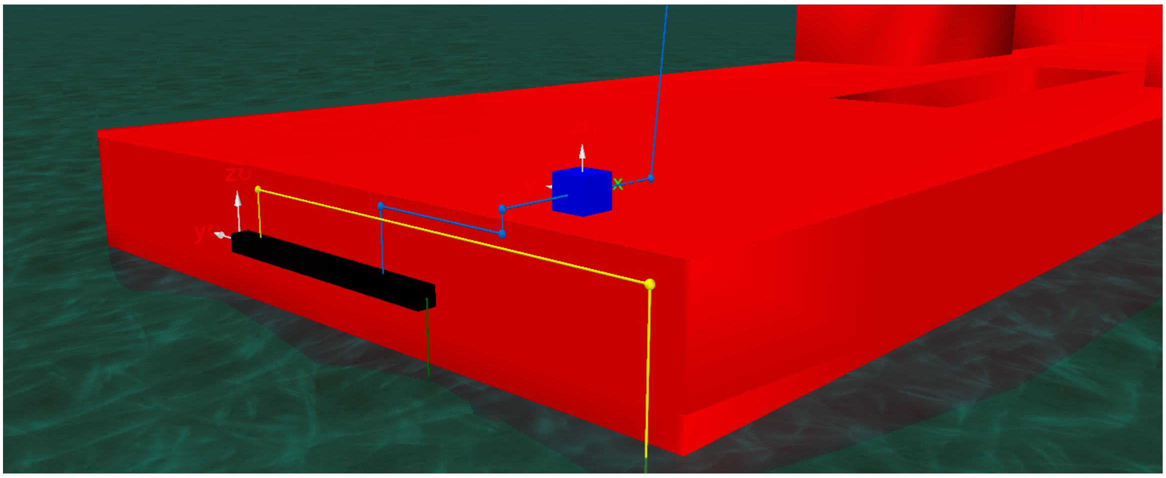

Figure 4.14: Modelling the sheave and wire inertia by means of an equivalent inertia. The equivalent inertia block and hoist wire in blue, earth-fixed wire in yellow and CTW in green. For clarity, the crane pedestal is removed.

sheave 9 and 10 (and thus with an additional degree of freedom, being the position of the block). The ratio between the sheave motion and the motion of the equivalent block inertia can be calculated according to Equation 4.10. In this equation, $\theta_{A,i}(\omega) \cdot r_i$ represents the product of the response amplitude of sheave i and its radius. This multiplication is performed to transform the sheave's rotational motion to a translational one. The response amplitude of the equivalent block is denoted as $x_A(\omega)$. The ratio is also a function of frequency, however, Figure 4.16 shows that the ratios are almost constant over the relevant frequency range. Considering that the vessel and RNA motions in the higher frequencies are relatively low, the small frequency dependency for these frequencies can be neglected. To do this, a frequency of 0.75 rad/s is used to determine the ratio for all sheaves.

$$\alpha_i(\omega) = \frac{\theta_{A,i}(\omega) \cdot r_i}{x_A(\omega)} \tag{4.10}$$

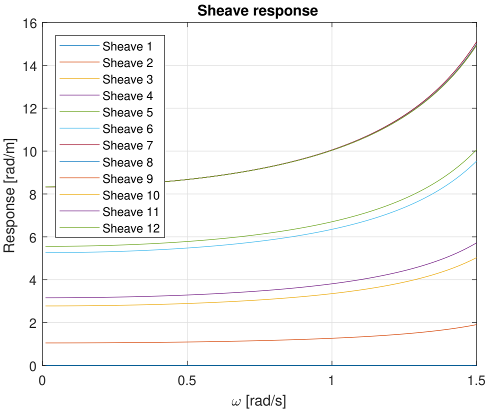

Figure 4.15: Response amplitude of sheaves 1 to 12.

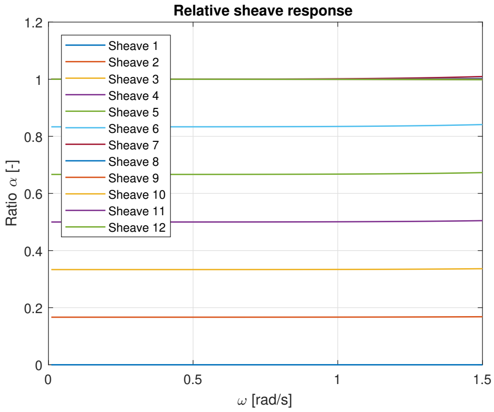

Figure 4.16: Relative response amplitude of sheaves 1 to 12 with respect to the response amplitude of the equivalent inertia block.

The formula for the total equivalent inertia yields:

$$\sum_{i=1}^{12} \alpha_i \cdot m_{eq,i} \tag{4.11}$$

Figure 4.17 and Figure 4.18 show the response amplitudes of the lever arm and the payload again. The orange graphs show the response amplitude for the analytical model including all sheave and wire inertia, as also shown in Figure 4.11 and Figure 4.12. The blue graphs show the response amplitude that is calculated for the new analytical solution, including the block with the equivalent inertia. It can immediately be seen that the the responses almost fully overlap. The average error of the response amplitudes is reduced from 3.3% to 0.9% and from 22.9% to 0.24% for the lever arm and payload respectively. These errors are considered acceptable and therefore is concluded that the an equivalent inertia block can be used to model the inertia of the hoist wires and the sheaves in the crane and crane block.

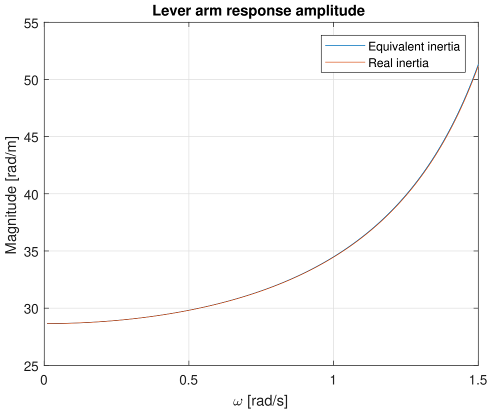

Figure 4.17: Response amplitude of lever arm for stage 3 with real inertia and equivalent inertia.

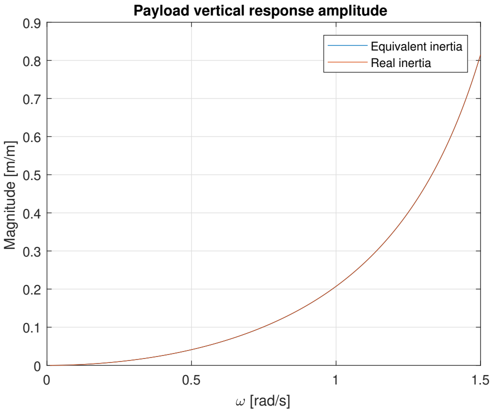

Figure 4.18: Vertical response amplitude of crane block for stage 3 with real inertia and equivalent inertia.

4.4. Wire-sheave losses

As discussed in subsection 2.4.3, there is a difference in tension between both sides of a wire, when bent over a sheave. This loss consists out of three parts. Loss due to: wire bending over the sheave, friction in the bearing of the sheave and friction in the seal of the sheave bearing. The losses are calculated respectively:

$$\Delta S_{wire} = \left(\frac{D}{d}\right)^{-1.33} \cdot \left(c_0 + c_1 \cdot \frac{S}{d^2}\right) \cdot d^2 \tag{4.12}$$

$$\Delta S_{bear} = \frac{\mu_{bear} \cdot d_{axle}}{D} \cdot \frac{S}{d^2} \cdot 2 \cdot \sin\frac{\theta_D}{2} \cdot d^2 = \frac{\mu_{bear} \cdot d_{axle}}{D} \cdot S \cdot 2 \cdot \sin\frac{\theta_D}{2} \tag{4.13}$$

$$\Delta S_{seal} = \frac{2 \cdot \pi \cdot q \cdot d_{axle}^2}{D \cdot d^2} \cdot d^2 = \frac{2 \cdot \pi \cdot q \cdot d_{axle}^2}{D} \tag{4.14}$$

$$\Delta S_{tot} = \Delta S_{wire} + \Delta S_{bear} + \Delta S_{seal} \tag{4.15}$$

The loss due to the wire bending over the sheave consists of a constant term, and a term that is depending on the tension S in the wire. The values chosen for the constants in Equation 4.12 are $c_0 = 3.06 N/mm^2$ and $c_1 = 2.029$ which correspond to an 8x36 zinc coated wire rope with steel core (Feyrer, 2007). This is the type of wire that is used as crane wire for HLV Aegir. Note that the equations are multiplied by d^2 to calculate the absolute loss of tension. The second loss due to bearing friction is proportional to the normal force on the bearing, which equals $S \cdot 2 \cdot \sin\frac{\theta_D}{2}$, in which θ_D represents the angle of the wire around the sheave. The last part, the seal loss, is constant.

First, the loss of sheaves 1 to 12 is determined, assuming that the tension in the wire is constant over time. Time-domain simulations have shown that this assumption is valid. The total weight of the RNA, spreader frame, and crane block is divided by 6 (crane reeving consists of 6 wire segments) to determine the static load in the hoist wire. The nominal load that is considered is $S = 1.18 \cdot 10^6 N$. Sheave 1 is neglected in this analysis, wire 1 is assumed to be stiff which result in a stationary sheave 1. In reality, wire 1 runs towards the driven crane winch via a number of sheaves. For future research, it is recommended to also model the wire and sheaves by means of an equivalent stiffness and inertia.

Sheave 2 to 12 are divided into four groups depending on diameter, and the deflection angle of the wire around each sheave. Set A consists of sheaves 3, 5, and 7, set B 2, 4, 6, set C is only sheave 8. Sheave 9 to 12 form set D. The results are shown in Table 4.3. The efficiency η shows the effiency per sheave in each set.

Set	A	B	C	D
η	99.4%	99.5%	99.5%	99.4%
$\Delta S_{wire}/\Delta S_{tot}$	0.74	0.73	0.97	0.80
$\Delta S_{bear}/\Delta S_{tot}$	0.26	0.27	0.03	0.20
$\Delta S_{rope}/\Delta S_{tot}$	0.00	0.00	0.00	0.00

Table 4.3: Sheave efficiency.

The loss seems to be dominated by the losses due to wire bending. More than 70% of the loss is caused by wire bending. The remainder of the loss is due to bearing friction. The friction due to the seal of the bearing can be considered negligible. The total loss of tension in the hoist wire, taking into account the same ratio of relative sheave response amplitude as in the previous section, is now calculated by Equation 4.16 for given parameters and equals 57.6 kN.

$$\sum_{i=1}^{12} \alpha_i \cdot (1-\eta_i) \cdot S \tag{4.16}$$

It should be borne in mind that the use of this single number might be oversimplified. It is not known yet how the tension in the hoist wire varies over time, this is discussed in chapter 5. Figure 4.19 already shows how the force loss depends on wire tension. Furthermore, Feyrer (2007) states that the the constant c_0, as used in Equation 4.12 has a large standard deviation of 1.73 $\mathrm{N/mm^2}$ and strongly depends on manufacturing conditions. The standard deviation of c_1 equals 0.031. Although the standard deviation of c_1 is much lower than c_0, it has a much bigger influence on the total force loss. Calculations show that the influence of c_0 is negligible, but Figure 4.20 shows that the effect of c_1 is significant. Although the statistical distribution of c_1 is not mentioned by Feyrer (2007), an increase of 1 time its standard deviation (0.259 + 0.031 = 0.29) results in an additional force loss of 5.5 kN. This is an increase of 9% compared to the mean value.

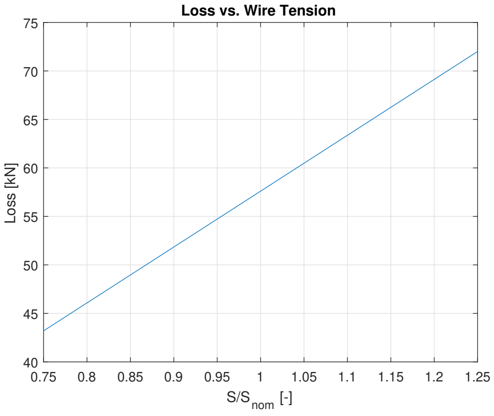

Figure 4.19: Loss in tension in hoist wire as a function of nominal wire tension.

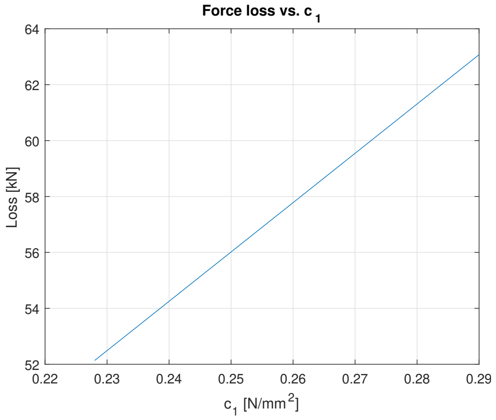

Figure 4.20: Loss in tension in hoist wire as a function of nominal wire tension.

4.4.1. Modelling losses

Ideally, the force loss or resistance, is added to the model in the following way:

$$F_{loss} = -\hat{F}_{loss} \cdot sgn(\dot{x}) \tag{4.17}$$

In which $\hat{F}_{loss}$ is the absolute value of the force loss, and $sgn(\dot{x})$ the *signum* function that yields 1 when $\dot{x} > 0$ and -1 when $\dot{x} < 0$. The argument $\dot{x}$ denotes the velocity of body to which the force is exerted. In practice, this means that when the block is moving in positive x-direction, a force is exerted on the block in the negative direction, and vice versa. The *signum* function is a discontinuous function which results in numerical problems when solving differential equations (Gear, C.W., Østerby, O, 1984). Schüthe et al. (2016) use a continuous and differentiable *sigmoid* function to approximate the *signum* function to overcome this numerical problem.

For modelling losses in OrcaFlex, a *sigmoid* function is used as well. The force that is exerted on the block is:

$$F_{loss} = 2 \cdot \left(\frac{1}{1+e^{-\beta \dot{x}}} \right) \cdot \hat{F}_{loss} \tag{4.18}$$

Figure 4.21 shows how such functions look like. The function approaches the discontinuous *signum* function with increasing β. For low β values, the force loss is underestimated for lower velocities. A convergence study has shown that for a value of $\beta = 70$, the simulations are still stable and the results are congverged. This value is used for the time-domain simulations.

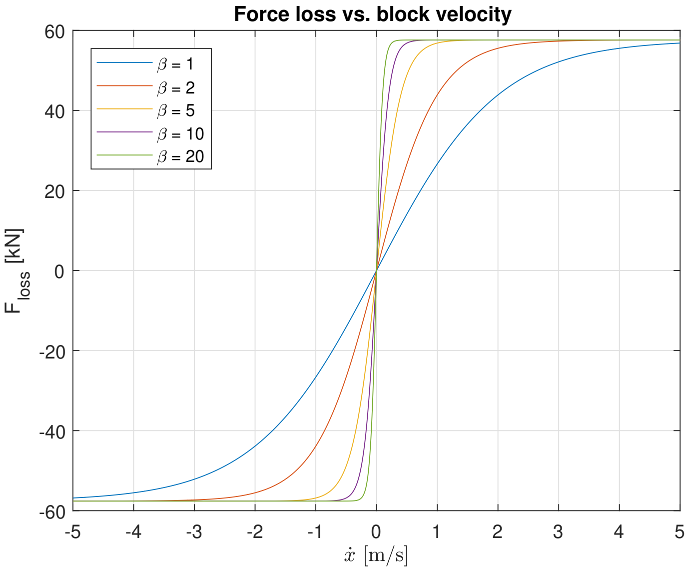

Figure 4.21: Force loss characteristics for various β-values.

5

Time Domain Simulations: Results & Discussion

In this chapter, the results of the time-domain simulations are discussed. At first, a simulation is done without earth-fixed heave compensation. Secondly, simulations are performed including earth-fixed heave compensation. The vessel motions and the system's behavior are assessed and adjustments are made before a parameter study is done. In this section, the effect of stiffness, inertia and the losses is discussed. Furthermore, the system is tuned by adjusting the transmission ratio to improve efficiency of the heave compensator. Lastly, a comparison is made with conventional heave compensation systems.

5.1. RNA and vessel motions without earth-fixed heave compensation

Before the earth-fixed heave compensation is added to the model in OrcaFlex for the time-domain simulations, a simulation is done for the vessel and payload without earth-fixed heave compensation. In chapter 3, these motions have been presented. These calculations were, however, in the frequency domain. In the frequency domain, it is assumed that all motions are linear and can be superimposed, which is not necessarily the case in the time-domain. To make a proper comparison between the cases with and without earth-fixed heave compensation, a separate time-domain simulation is done with following wave conditions:

- Spectrum type: JONSWAP
- Significant wave height: $H_s = 1.5$ m
- Peak period: $T_p = 9.64$ s ($T_z = 7.5$ s)
- Wave direction: $\theta_{wave} = 180°$
- Wave spreading: No

The significant double amplitudes of the vessel, vertical crane tip and vertical payload motions are given in table below.

Motion	SDA	Motion	SDA
Heave	0.28 m	Crane tip (vertical)	0.54 m
Roll	0.17 deg	Payload (vertical)	0.54 m
Pitch	0.58 deg		

Table 5.1: Significant double amplitude of vessel motions, crane tip and payload without earth-fixed heave compensation.

The time-domain simulation has a duration of 3 hours, of which only the last two hours are used to determine the statistical values. In this way, the effect of transient responses in the simulations is minimized. The time traces of the first simulation can be found in Appendix D. In the following sections, the behaviour of the earth-fixed heave compensation system and its effect on the vessel motions are assessed.

5.2. RNA and vessel motions with heave compensation

In this section, the earth-fixed heave compensator is added to the model. The vessel and heave compensation behaviour are also considered. Following the first simulation as described in the previous section, the model is adjusted and prepared for the rest of the simulations for the parameter study and tuning phase.

5.2.1. Vessel motions

Table 5.2 shows that some of the vessel and payload motions are significantly affected by the presence of the earth-fixed heave compensation system. Although the pitch motion of the vessel decreases, the roll motion increases by more than 140%. This results in a net increase of the vertical crane tip motion. The difference can be caused by one, or a combination, of the following aspects:

1. Different mean position of the vessel due to additional forces. The additional force of the earth-fixed wire and the weight of the lever arm cause a difference in static heeling, trim and draught of the vessel.
2. Different vessel behaviour due to changing inertia of total system. The inertia of the system, mainly around x- and y-axis and in heave direction, is different when the heave compensation system is included. If the system works properly, the payload moves less than in the situation without heave compensation. Therefore, the contribution of the payload weight, or a part of it, can be neglected for the calculation of the total moment of inertia around x- and y-axis.
3. Different vessel behaviour due to the presence of the earth-fixed wire. The earth-fixed wire works as a spring and creates additional stiffness in all vessel directions which changes the response of the vessel.

Motion	SDA	SDA (EFHC included)	Motion	SDA	SDA (EFHC included)
Heave	0.28 m	0.30 m	Crane tip (vertical)	0.54 m	0.60 m
Roll	0.17 deg	0.41 m	Payload (vertical)	0.54 m	0.31 m
Pitch	0.58 deg	0.50 m			

Table 5.2: Significant double amplitude of vessel, vertical crane tip and vertical payload motions with and without earth-fixed heave compensation.

A simulation with updated ballast conditions of the vessel showed that the first aspect can be neglected. The slightly different static and mean values of heeling, trim and draught have no significant influence on the vessel behaviour. Therefore, this difference is neglected. The second aspect cannot be neglected but has a limited influence. The contribution of the RNA to the total moment of inertia around the x-axis of the vessel is approximately 6% for given vessel configuration. The big difference in vessel response is thus caused by the presence of the earth-fixed wire.

It is concluded that the vessel motions and the earth-fixed heave compensation system cannot be considered separately as done for the analytical solution. Originally, the earth-fixed wire was located on the vessel to be as close as possible to the projection of the crane tip on the horizontal plane. In this way, roll, pitch and heave motions of the vessel would be transferred to the heave compensation system in the best possible way. However, the location of the earth-fixed wire turns out to cause large unwanted roll motions of the vessel. This increases the vertical crane tip motions and might reduce performance of the heave compensation as well. The influence of this location of the earth-fixed wire is discussed in subsection 5.2.4.

5.2.2. Constant tension winch

The first simulation with earth-fixed heave compensation was done for a force of 736 kN (≈ 75 t) in the constant tension winch. All nominal parameters, as presented in chapter 4, are used for this simulation. Again, a total duration of 3 hours is used, of which only the last 2 hours are taken into account to calculate statistical parameters. Figure 5.1 shows what the model looks like.

Although the first simulation itself with a constant tension winch of 736 kN was successful, the heave compensation system did not work as expected. The SDA of the vertical crane tip motion was the same for the payload and thus no motion was compensated. It is also observed that the tension in the earth-fixed wire regularly dropped to zero. This is something that should be avoided at all times since this can result in very high

Figure 5.1: HLV Aegir including earth-fixed heave compensation modelled in OrcaFlex.

peak loads, or even snapping of the earth-fixed wire. Figure 5.2 shows the time traces of the tension in the earth-fixed wire for constant tension forces from 736 kN (≈ 75 t) up to 932 kN (≈ 95 t). As expected, the higher the tension of the winch, the higher the average tension in the earth-fixed wire. Looking at these results, the most preferable tension for the CTW is 932 kN since it results in the lowest probability of the earth-fixed wire becoming slack. However, this means a heavier winch is needed. In the 2 hours of the simulation, the wire became slack only one time during approximately 840 oscillations. A detailed analysis in further research should provide an acceptable chance of slackening for the earth-fixed wire. From this limit, a pretension should be determined. In this research, a value of 932 kN is used for further simulations. In subsection 2.4.5 is mentioned that commercial constant tension winches are available up to a capacity of 100 t (981 kN). The tension of 932 kN is acceptable but it should be noted that this is almost at the maximum currently available capacity.

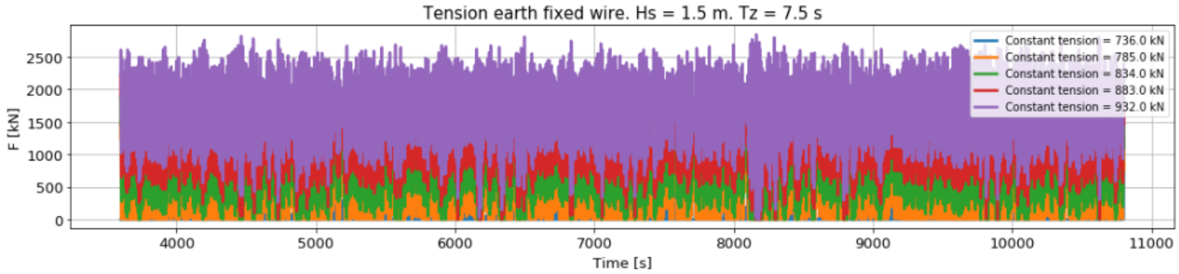

Figure 5.2: Tension earth-fixed wire for various CTW tensions.

5.2.3. Earth-fixed wire and hoist wire

In chapter 4, it was assumed that the tension in the hoist wire was constant to determine the losses in this wire. The losses due to the wire-sheave interaction at the earth-fixed wire were so far neglected. Figure 5.3 shows the tension in the hoist wire for the time domain simulation for F_{CTW} = 932 kN. The mean tension is 1183 kN and it has a standard deviation of 13 kN over the full simulation. It is therefore considered acceptable to calculate the losses as a function of the constant mean tension in the hoist wire.

The tension in the earth-fixed wire, as shown in Figure 5.2, has a mean tension of approximately 1620 kN, but

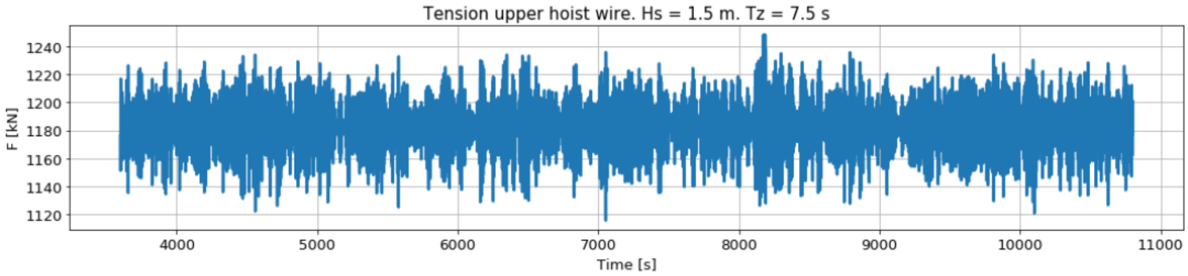

Figure 5.3: Tension hoist wire for F_{CTW} = 932 kN

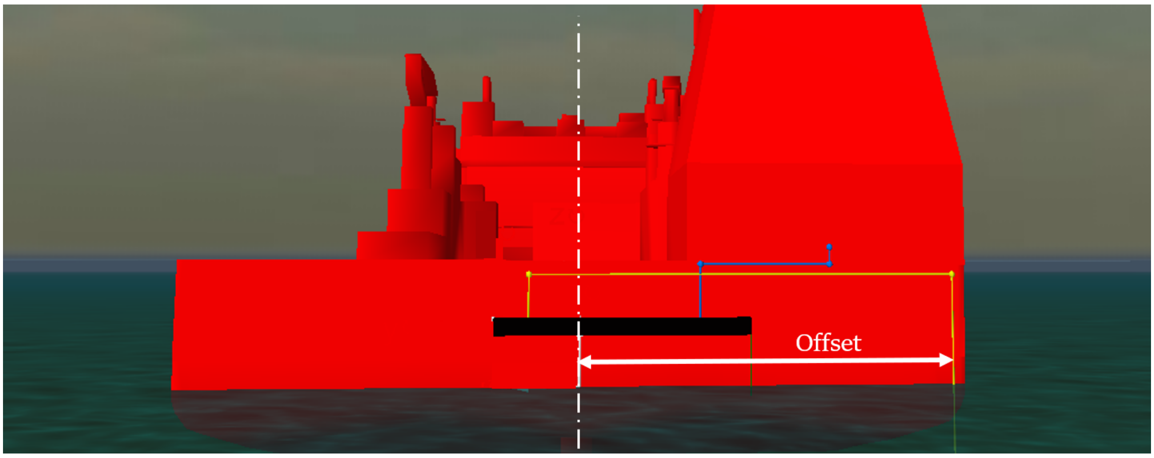

Figure 5.4: Offset of -22.1 m of the earth-fixed wire.

a large standard deviation of 398 kN. The loss due to wire-sheave interaction for the earth-fixed wire for this mean tension is 24 kN (approximately 1.5 % of the mean tension), when calculated according to the method in section 4.4. Although the tension in this wire is far from constant, a separate simulation has been done for a loss of 24 kN in this wire. This means an overestimation of the loss is made when the tension is lower than the mean, and vice versa. The simulation showed a difference in vessel response up to 1.1% and a reduction of lever arm motion of 1.6%. Simulations for losses based on the earth-fixed wire mean tension plus and minus twice its standard deviation also showed no significant differences. Therefore, the losses due to the sheaves for the earth-fixed wire are neglected.

5.2.4. Lateral offset earth-fixed wire

In section 5.2 is shown that the presence of the heave compensation system has a significant influence on the roll motion of the vessel, and therefore on the crane tip and vertical payload motions. The current location of the earth-fixed wire on the vessel creates moments around the x- and y-axis of the vessel. The moment arm that the earth-fixed wire has with respect to the y-axis of the vessel cannot be changed since the system has to be placed on the stern of the vessel due to limited deck capacity. The moment arm with respect to the x-axis, however, is a parameter that can be changed. This moment arm, or offset, is shown in Figure 5.4 for the original position of the earth-fixed wire. Time-domain simulations are performed for offsets of -22.1 m, -15 m, -10 m, -5 m, 0 m, 5 m, 10 m, 15 m and 22.1 m. Note that the positive y-direction is pointing from starboard to portside. In the figures in this section, the values of the x-axis are mirrored so that the left hand side of the graphs represent portside, the right hand side starboard.

Figure 5.5 up to Figure 5.7 show the significant double amplitude of the heave, roll and pitch motion of the vessel for all 9 simulations. The blue graphs denote the actual SDA, the orange graphs are normalized such that the SDA for the earth-fixed wire at starboard (-22.1 m) equals one. The graphs show that the heave and pitch motion are hardly affected by the lateral position of the earth-fixed wire, as expected. The SDA of the roll motion, however, is reduced by almost 75% when the earth-fixed wire is located at the centerline. This difference cannot be explained by only the tension in the earth-fixed wire, the SDA differs only 2.4% when comparing the tension for starboard and centerline position.

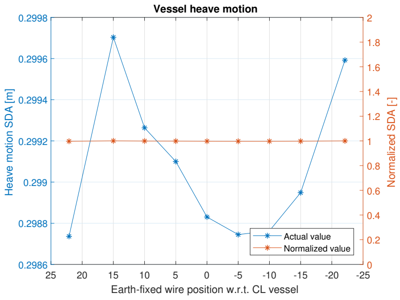

Figure 5.5: Vessel heave motions for different lateral positions of earth-fixed wire.

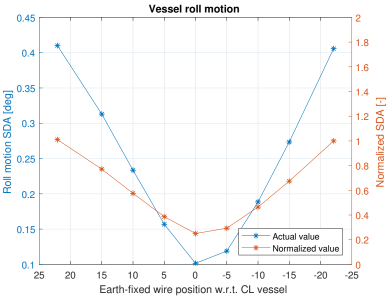

Figure 5.6: Vessel roll motions for different lateral positions of earth-fixed wire.

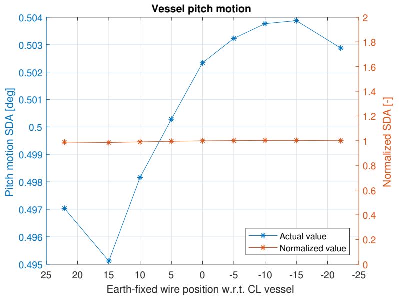

Figure 5.7: Vessel pitch motions for different lateral positions of earth-fixed wire.

This large difference in roll motion of the vessel can be explained by looking at the graphs in Figure 5.8. These graphs show the time traces of four simulations, all with a different offset of the earth-fixed wire. The x-axis shows the roll angular velocity of the vessel. Looking at the stern of the vessel (as also shown in Figure 5.4), the roll velocity is positive when the vessel rolls clockwise, negative when rotating counterclockwise. The y-axis shows the additional roll moment that is caused by the tension in the earth fixed wire and is calculated as follows. First, the mean tension is subtracted from the earth-fixed wire tension. This mean tension is balanced by ballasting the vessel and is not relevant for the dynamic behavior. Secondly, the calculated tension is multiplied by the moment arm around the centerline of the vessel. This moment arm is equal to the absolute value of the earth-fixed wire offset. Note that a negative roll moment does not mean that the earth-fixed wire 'pushes' the vessel, this is impossible. A negative roll moment shows that the moment caused by the earth-fixed wire is lower than its mean, resulting in a net moment on the vessel due to centre of gravity of the vessel. A positive moment is defined as a clockwise moment, when looking at the stern of the vessel.

Figure 5.8 can be split up in 4 quadrants:

- Quadrant 1 (top-right): Positive additional moment and positive angular roll velocity. Additional moment works in the same direction as the roll motion of the vessel.
- Quadrant 2 (top-left): Positive additional moment and negative angular roll velocity. Additional moment works in opposite direction of the roll motion of the vessel.
- Quadrant 3 (bottom-left): Negative additional moment and negative angular roll velocity. Additional moment works in the same direction as the roll motion of the vessel.
- Quadrant 4 (bottom-right): Negative additional moment and positive angular roll velocity. Additional moment works in opposite direction of the roll motion of the vessel.

In quadrant 1 and 3, the roll motions of the vessel are increased, in quadrant 2 and 4, roll motions are reduced. Not only is the additional roll moment on the vessel bigger for the larger earth-fixed wire offset, also the amount of time in quadrants 1 and 3 is bigger for larger offsets. For instance, for an offset of -22.1 m, the additional moment is in the same direction of the roll motion 62% of the time. For the offset of -5 m, this is only the case 21% of the time. On top of that, the average additional roll moment in this time is respectively $7.3 \cdot 10^3$ kNm and $1.1 \cdot 10^3$ kNm. This means the roll motions are increased significantly for bigger offsets.

Figure 5.9 and Figure 5.10 respectively show the significant double amplitudes of the vertical crane tip and payload motion. A reduction for the SDA of the crane tip motion is observed for earth-fixed wire positions close to the centerline of the vessel. The vertical crane tip motions are reduced with 26% for an earth-fixed wire position of 5 m. The vertical payload motion SDA is lowest for the centerline position of the wire. This motion is reduced by 42% from an SDA of 0.31 m to 0.18 m. The performance of the heave compensation system significantly increased from 49% to 61% for the centerline position.

As mentioned in subsection 5.2.1, the location of the earth-fixed wire was chosen to be at the starboard side of the vessel to be as close as possible to the horizontal projection of the crane tip. Geometrically, this would mean that the motions of the crane tip would also be experienced in the earth-fixed wire to some extent.

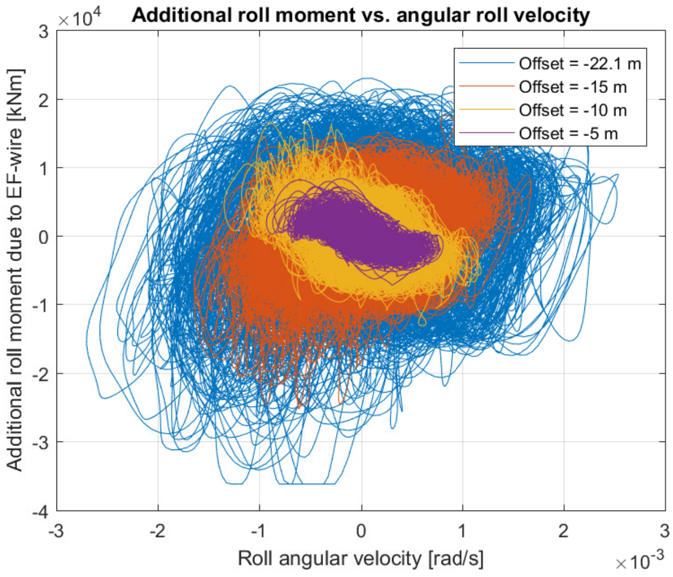

Figure 5.8: Additional roll moment due to earth-fixed wire and roll velocity of the vessel.

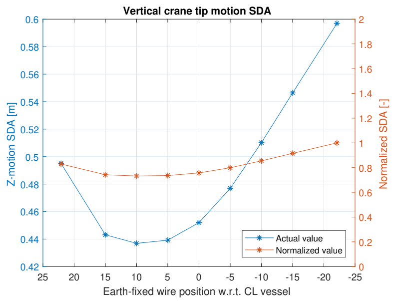

Figure 5.9: Crane tip motion for different lateral positions of earth-fixed wire.

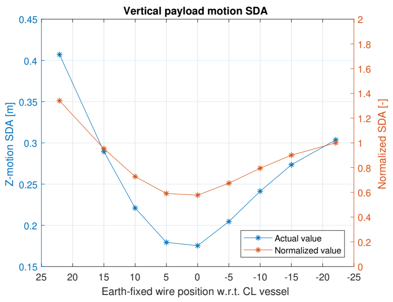

Figure 5.10: Payload motion for different lateral positions of earth-fixed wire.

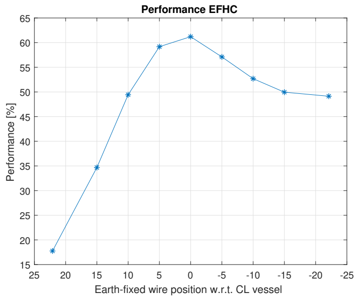

Figure 5.11: Earth-fixed heave compensation performance for different lateral positions of earth-fixed wire.

However, the simulations in this section have shown that this earth-fixed wire location creates large roll motions that significantly increases vertical crane tip and payload motions. This means that for given crane slew angle, a centerline position of the earth-fixed wire gives best performance and lowest vertical payload motions. It should be noted that the differences in vessel and heave compensation behaviour are not solely caused by a difference in lateral position of the earth-fixed wire. It is expected that a small contribution is caused by the stiffness difference of the earth fixed wire. For example, when the earth-fixed wire is located at the centerline of the vessel, the total length of the wire is smaller than when it is located on portside or starboard. This change in length causes a change in stiffness as well. The effect of wire stiffness is discussed in subsection 5.3.1.

5.2.5. Performance definition

The performance of the system is defined according to Equation 5.1 and equals 61% for the system without any tuning of its parameters, except for the lateral position of the earth-fixed wire. In the following sections is investigated whether this system can be tuned to increase the performance of the heave compensation system. It should be noted that the performance can be a good parameter to compare various EFHC configurations, but is not the only parameter to consider when choosing a configuration. For instance, in a system with a performance of 80% and a crane tip heave of 1 m, the payload heave is 0.2 m. In a system with 75% performance and a crane tip heave of 0.6 m, the payload only heaves 0.15 m. Since simulations showed that EFHC significantly affects the vessel behaviour, situations might occur in which a configuration with lower performance yields a lower absolute payload motion.

$$P = \left(1 - \frac{SDA_{payload}}{SDA_{cranetip}}\right) \cdot 100\% \tag{5.1}$$

5.3. Parameter study

In the following sections, the effects of stiffness, inertia and losses of the systems are discussed. In the time-domain simulations, the earth-fixed wire is located at the centerline of the vessel.

5.3.1. Stiffness

Two main elements in earth-fixed heave compensation determine the stiffness of the system. The first one is the crane wire, the second one the earth-fixed wire. The crane wire wire stiffness is known and expected error for this stiffness is small since this value is tested by the manufacturer. The earth-fixed wire, however, is yet to be chosen. The nominal stiffness of this wire was based on the Oceanmax 35, as mentioned in chapter 4. Investigating the effect of this stiffness is useful to determine what wire stiffness should be chosen if the system would be further developed. On top of that, it tells how the system will behave in shallower and deeper waters since the wire stiffness is inversely proportional to the length of the wire.

For this section, 7 time-domain simulations are performed. The earth-fixed wire is mounted at the centerline of the vessel. The stiffness is varied from 50% to 200% of the nominal stiffness. Figure 5.12 to Figure 5.14 show results of these simulations. While the cranetip motions only differed up to 2%, the payload motions were increased by 48% for half of the nominal earth-fixed wire stiffness. This resulted in a performance drop from 61% to 43%. When the stiffness is increased by a factor 2, the payload motions reduce with 13%, resulting in a 66% performance.

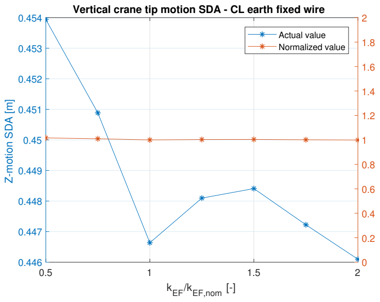

Figure 5.12: Crane tip motion for different earth-fixed wire stiffnesses, earth-fixed wire mounted at centerline of vessel.

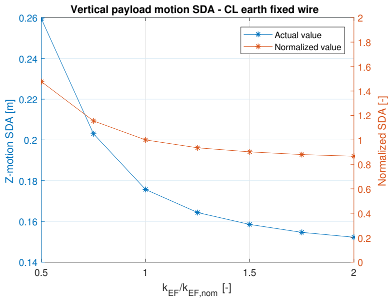

Figure 5.13: Payload motion for different earth-fixed wire stiffnesses, earth-fixed wire mounted at centerline of vessel.

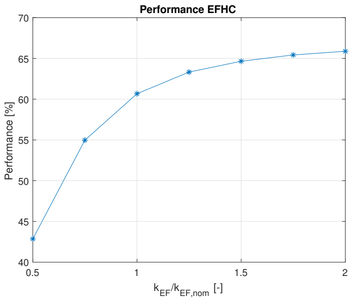

Figure 5.14: EFHC performance for different earth-fixed wire stiffnesses, earth-fixed wire mounted at centerline of vessel.

It is of importance to mention that this significant response difference of the vertical payload motions is not only caused by a difference in SDA of the lever arm motion. This SDA is only increased by 1% for half of the nominal stiffness. To understand what happens, Figure 5.15 and Figure 5.16 are considered. The first graph shows the relation between the lever arm rotation and the relative vertical difference between the crane tip and the payload, for three of the 7 simulations. For instance, when the lever arm rotates to -5 degrees (counterclockwise), the distance between the payload and the cranetip increases by approximately 0.18 m. This graph shows that for the full range of wire stiffnesses, there is no significant phase lag between the motion of the lever and the payload.

Since there is no significant difference in lever arm amplitude, nor a significant phase lag between the lever arm and the payload, the large difference in payload motion has to be the result of phase differences between lever arm and vessel motion. This phenomenon can be seen in Figure 5.16. It shows the relation between the vertical cranetip motion and the lever arm motion. If the earth-fixed wire was located at starboard, quasistatic behaviour would show an almost[1] perfect linear relation. The graphs show how the vessel motions, and thus cranetip motions, are transferred to the lever arm. Although the SDA of the lever arm motion is not significantly different for the three simulations, it can be seen that the stiffer the wire is, the better the response of the lever arm rotation. The graphs show that there is a relatively large phase difference between cranetip and lever arm motion when a low stiffness is used.

---

[1] When the lever arm is horizontal, the earth-fixed wire is perpendicular to the lever arm. When the lever arm rotates, the wire is not perpendicular to the arm anymore. Due to this rotation, the relation between the lever arm rotation and the cranetip motion is not perfectly linear, even when considered quasistatic. The maximum error is below 1% for a maximum lever arm rotation of 14 degrees.

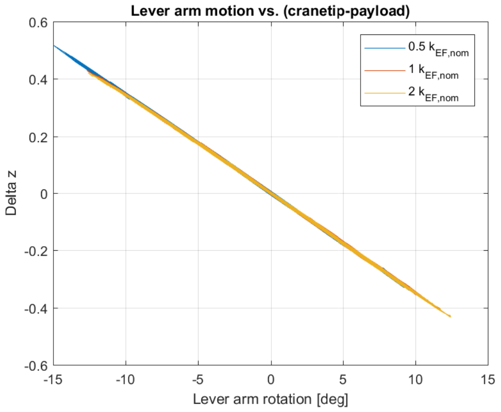

Figure 5.15: Lever arm motion versus relative payload motion for different earth-fixed wire stiffnesses.

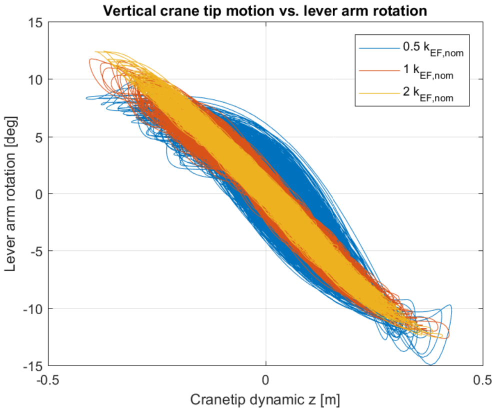

Figure 5.16: Vertical crane tip motion versus lever arm motion for different earth-fixed wire stiffnesses.

The simulations have shown that the stiffness of the earth-fixed wire is an important design parameter for earth-fixed heave compensation. Performance of the system drops down rapidly for a more flexible wire. For deeper waters this might be a problem since the wire has to be long which results in a lower stiffness. It is recommended to use a combination of wire rope (top) and chains (bottom) to increase stiffness of the system and therefore improve performance, taking the relatively heavy weight of the chain links into account.

5.3.2. Transmission inertia

The mass, and therefore inertia, of the lever arm is an important design parameter. The beam is considered to be prismatic and to have a mass of 50 t. The rotational moment around the hinge is calculated by $J = \frac{1}{3} \cdot m \cdot l^2$ and is therefore proportional to its mass. Time-domain simulations with a lever arm moment of inertia varying from 0.5 to 2 times the nominal inertia show the results as presented in Figure 5.17 to Figure 5.19. To compensate for the difference in weight of the lever arm, the CTW tension is adjusted. The pretension in the earth-fixed wire remains equal.

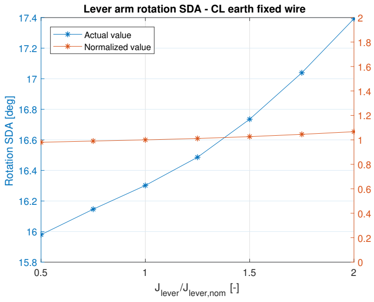

Figure 5.17: Lever arm motion for different values of lever arm rotational inertia.

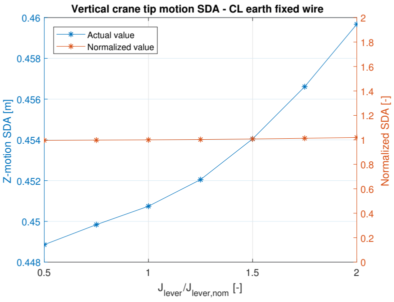

Figure 5.18: Cranetip motion for different values of lever arm rotational inertia.

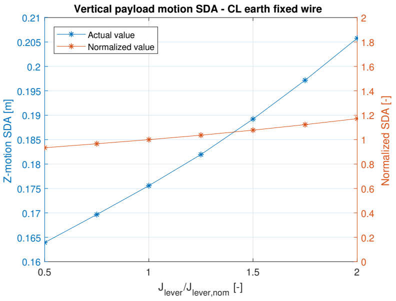

Figure 5.19: Payload motion for different values of lever arm rotational inertia

When the inertia is increased by a factor 2, the vertical payload motions increase by 17%. This time, there is not one main aspect that causes this increase. First of all, the SDA of the lever arm motion increases by 7%. Secondly, there is more out-of-phase behaviour of the lever arm with respect to the vessel motions for a higher inertia. Furthermore, the crane tip motion is increased by 2% due to small differences in heave, roll and pitch amplitude.

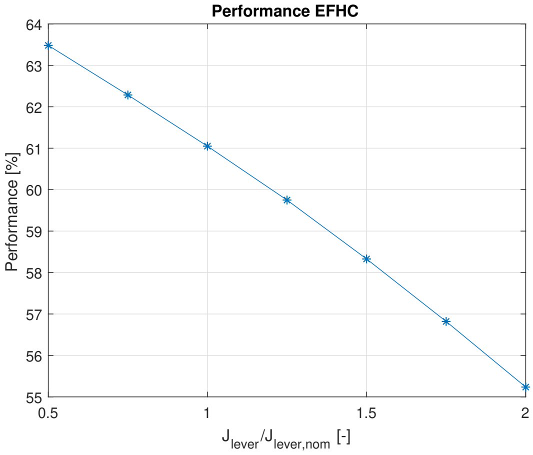

Figure 5.20: EFHC performance for different values of lever arm rotational inertia.

All these effects combined influence the performance of the system, as shown in Figure 5.20. To optimize performance, it is preferable to minimize the inertia of the lever arm. However, this comes at a price. A lowered inertia and weight of the lever arm result in a higher mean force that the constant tension winch needs to exert on the lever arm, which increases the power needed by the CTW. Another aspect that should be considered is the structural integrity of the lever arm. The beam should be able to withstand the stresses that occur due to bending moments and shear forces in the beam. This design is not in the scope of this report.

In Appendix E, a sensitivity analysis is shown for the mass of the payload. It is shown that within reasonable contingency limits of the payload mass, the performance does not vary significantly. The simulations show that there is a positive relation between the mass of the payload and the performance. However, this does not have to be the case for significantly smaller or larger masses. This does not only affect the behavior of the heave compensator, but also the rotational inertia of the vessel and payload. On top of this, the static heeling angle, trim angle and draught of the vessel change.

5.3.3. Losses

The losses of the system have the largest uncertainty of all parameters, even in a later design stage. It is therefore important to know how the system behaves when the losses are different than expected. Time-domain simulations with different losses due to wire-sheave interaction are done to investigate the sensitivity to a varying loss. For these simulations, all parameters remain the same except for the total loss of tension in the hoist wire. The losses are modelled as explained in subsection 4.4.1, with a varying $\hat{F}_{loss}$. The results of these simulations are shown below.

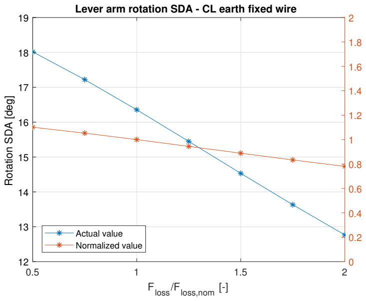

Figure 5.21: Lever arm motion for varying loss.

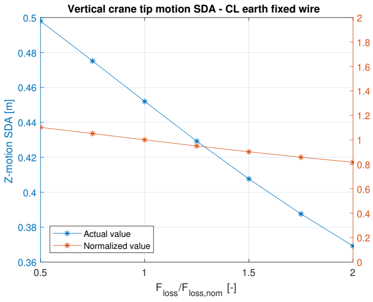

Figure 5.22: Vertical cranetip motion for varying loss.

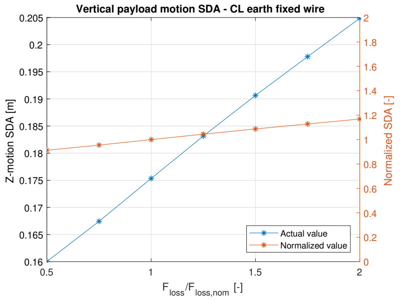

Figure 5.23: Vertical payload motion for varying loss.

It is remarkable to see that the vertical payload motion SDA increases for an increasing loss. The vertical crane tip motion, on the contrary, decreases for increasing losses due to different vessel motions. This clearly indicates that the performance of the system decreases for increasing losses, which is also shown in Figure 5.24 and Figure 5.25. The latter graph shows the relation between the vertical cranetip motion and the rotation of the lever arm, in the same way as in subsection 5.3.1. It is observed that generally there is a larger phase lag between the lever arm rotation and the vertical crane tip motion for increasing losses. Earlier simulations have shown that an increasing loss does not result in a significant change of amplitude of the lever arm rotation. This means that the decreasing SDA of the lever arm motion is not only caused directly by losses, but also by reduced vessel motions.

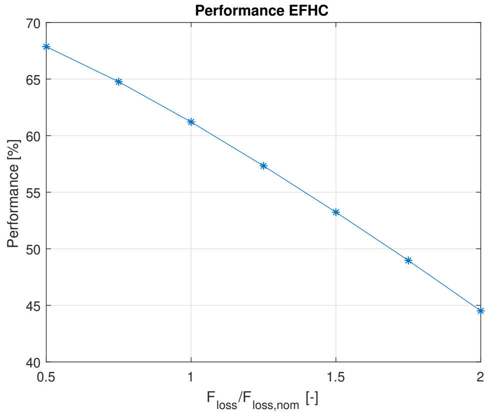

Figure 5.24: EFHC performance for varying loss.

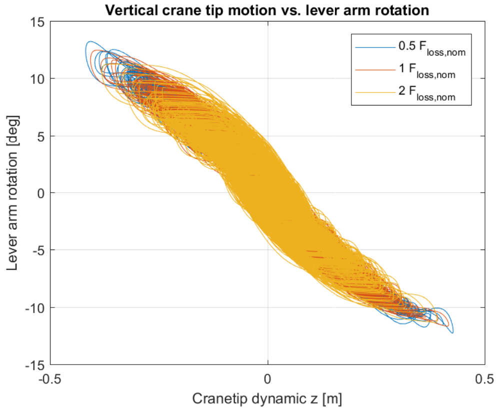

Figure 5.25: Vertical cranetip motion versus lever arm rotation.

Figure 5.26 to Figure 5.28 show that there is decrease in pitch motion of the vessel, whereas roll and heave motions do not significantly change for increasing losses. The SDA of the pitch moment is reduced to 91% of its nominal value for a loss increase of a factor 2.

To understand why this pitch motion reduction is happening, the tension in the earth-fixed wire as a function of the losses has to be considered. Figure 5.29 shows the standard deviation of the earth-fixed wire tension, as a function of losses in the system. The graph shows a significant increase in standard deviation of the tension. This phenomenon can be explained by the following example. When the stern of the vessel moves upwards, tension in the earth-fixed wire increases. The only way to reduce this tension, is by rotating the lever arm counter-clockwise. This rotation is damped by the losses in the hoist wire. Therefore, the standard

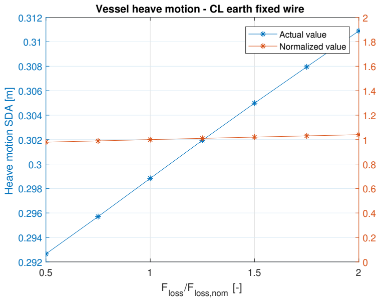

Figure 5.26: Vessel heave motion for different tensile losses.

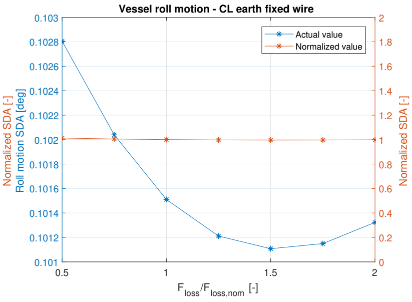

Figure 5.27: Vessel roll motion for different tensile losses.

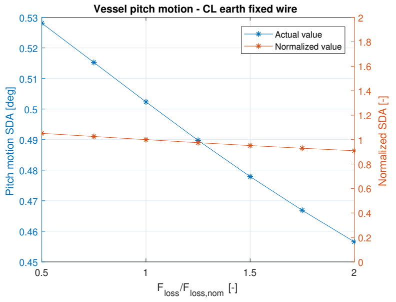

Figure 5.28: Vessel pitch motion for different tensile losses.

deviation of the earth-fixed wire tension increases for increasing losses. The second important aspect causing reduced pitch motions is shown in Figure 5.30. In this figure, time traces of the angular pitch velocity versus the additional pitch moment created by the earth-fixed wire are shown for varying losses. In the quadrants where the additional moment on the vessel has the same sign as the angular velocity (quadrant 1 and 3), the moment is adding energy to the system and therefore increasing vessel motions. In the quadrants where the additional moment on the vessel has the opposite sign of the angular velocity (quadrant 2 and 4), the earth-fixed wire is reducing vessel motions. It is observed that for increasing losses, the phase of the additional pitch moment with respect to the angular pitch velocity is, on average, moving. More data points are present in quadrants 2 and 4 for increasing losses.

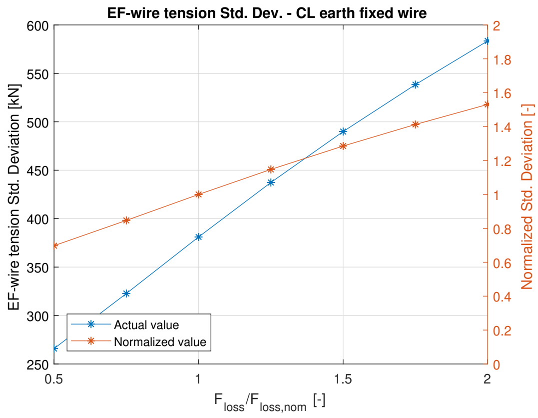

Figure 5.29: Earth-fixed wire tension standard deviation for different tensile losses.

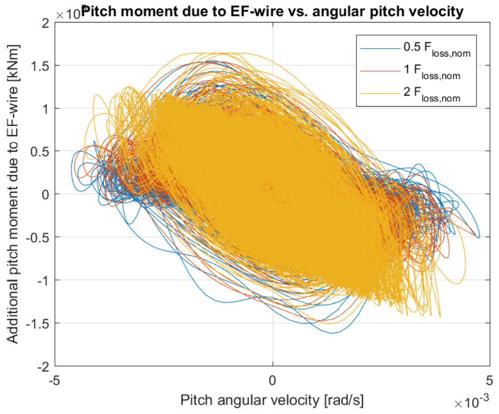

Figure 5.30: Angular pitch velocity of vessel versus additional pitch moment of earth-fixed wire.

The combination of an increasing standard deviation of the earth-fixed wire tension and a phase shift of the additional pitch moment with respect to the angular pitch velocity decrease vessel motions. The last check to be performed is to determine the order of magnitude of the moment created by the earth-fixed wire and compare it with the total force on the vessel. The earth-fixed wire tension standard deviation varies from approximately 270 kN to 580 kN for the considered range of losses. Multiplying this force with the distance between the earth-fixed wire (in y-direction) and the vessel origin yields standard deviations of $2.57 \cdot 10^4$ kNm to $5.50 \cdot 10^4$ kNm. Comparing these moments to the standard deviation of the total force on the vessel, which equals $3.96 \cdot 10^5$ kNm, it is plausible that the losses result in a decrease of pitch motion. The standard deviation of the earth-fixed wire tension for given losses are between 6% and 14% of the standard deviation of the total force on the vessel.

Furthermore, decay tests show pitch natural periods between 9.3 and 10 seconds. Since the used wave spectrum has a peak period of 9.6 seconds, i.e. most energy is present in waves with this period, a relatively small additional amount of damping can result in a significant decrease of motion amplitude.

5.4. Tuning performance of earth-fixed heave compensation

In this section, it is investigated whether performance can be improved by tuning earth fixed heave compensation. Figure 5.31 shows a schematic drawing of the lever arm and the earth fixed wire. Again, the original parameters were determined based on the geometry of the vessel and crane. The transmission ratio of the system is defined by $\frac{L_B}{L_A}$. The original ratio that was chosen is 6 because the reeving of the crane wire consists out of 6 wire segments. This would mean that the motion is completely reduced for small and quasistatic motions. The behaviour of the system in real waves, however, cannot be considered quasistatic. In this section, the effect of the transmission ratio on the vessel and payload behaviour is discussed.

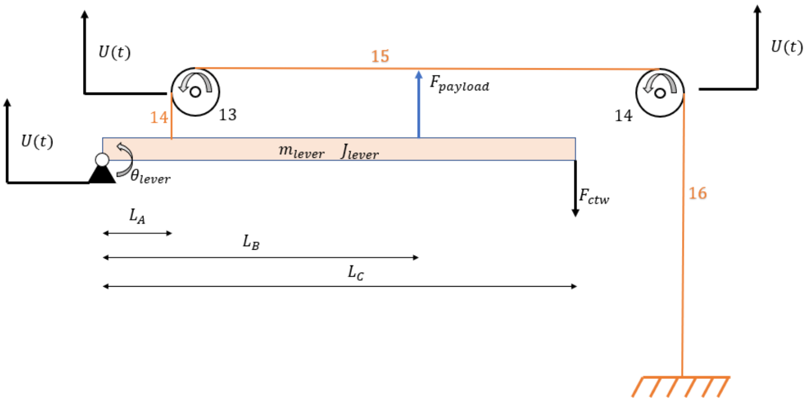

Figure 5.31: Lever arm parameters.

A set of 15 time-domain simulations is considered. The variables that are changed are the transmission ratio, and the tension of the constant tension winch. The former is changed by changing length L_B while keeping length L_A equal. The latter has to be done to position the lever arm horizontally in static equilibrium. Table 5.3 shows the force that the constant tension winch has to exert for some of the transmission ratios. The winch forces that are shown in red are exceeding the capacity of what is found commercially available.

The vertical payload motion shows a significant decrease for a decreasing transmission ratio. Payload motions are reduced from an SDA of 0.18 m to 0.09 m for a transmission ratio of 4.5. The performance increased to 80% for this transmission ratio.

Transmission ratio [-]	3.5	4	4.5	5	5.5	6	6.5	7
F_{CTW} [kN]	538	616	695	774	853	932	1011	1090

Table 5.3: Transmission ratios and correspondingly constant tension winch force.

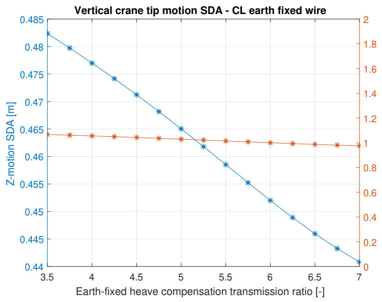

Figure 5.32: Crane tip motion for different transmission ratios, earth-fixed wire mounted at centerline of vessel.

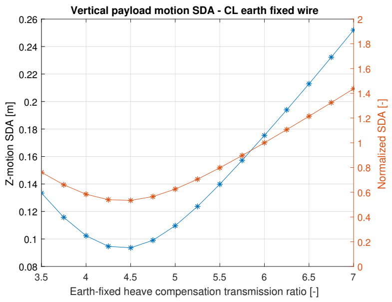

Figure 5.33: Payload motion for different transmission ratios, earth-fixed wire mounted at centerline of vessel.

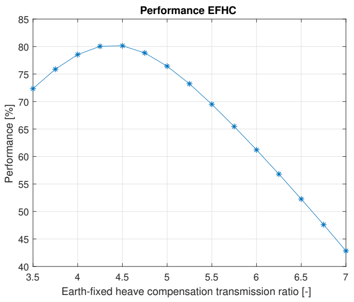

Figure 5.34: EFHC performance for different transmission ratios, earth-fixed wire mounted at centerline of vessel.

In the first simulations for the untuned EFHC, a performance of 43% was achieved which reduced the vertical payload motions from an SDA of 0.54 m to 0.31 m. By using a combination of a different lateral position of the earth-fixed wire and a different tranmission ratio, it was possible to reduce crane tip motions and payload motions. For a given sea state, earth-fixed wire at centerline and a transmission ratio of 4.25, vertical payload motions are reduced to a SDA of 0.09 m. This is equal to a performance of 80%. This performance is calculated using Equation 5.1 and takes into account the cranetip SDA of the same simulation. If the vertical payload motion is compared to the situation of the free floating vessel, a performance of 83% is achieved.

5.5. Comparison conventional heave-compensation

In chapter 2, the performance of both active and passive heave compensators is discussed. A typical motion reduction of 80-85% is achieved by passive heave compensation. Active heave compensation systems, on the other hand, achieve a performance up to 95%. The maximum performance of earth-fixed heave compensation that is found in this research is 80% but is specific for the used environmental conditions, water depth, crane slew angle, vessel heading, payload mass, and first estimates of properties for the earth-fixed wire and lever arm inertia. This performance is found by tuning the transmission ratio, but keeping all other parameters the same. It is concluded that, in principle, the system has the potential to be competitive with conventional heave when looking only at this performance.

Nevertheless, it should be borne in mind that this performance includes a large uncertainty. Variations in inertia, stiffness and losses can significantly affect the behavior of both the vessel and EFHC. Secondly, additional simulations should point out whether a comparable performance is obtained for different vessel headings, wave periods and water depths. A sensitivity analysis in Appendix E shows that the vessel motions strongly depend on wave direction and mean zero-crossing (or peak) period. The performance depends strongly on the wave period but less on wave direction. Although this is not further discussed in this report, it should be taken into account when designing a system like this.

HLV Aegir has an installed power supply of 3 MW for heave compensation, as mentioned in chapter 1. Other heave compensation systems such as DSMC and CSMS respectively consume up to 3.2 MW and 0.8 MW respectively for a mass of only 10 t, as explained in chapter 2. When considering the simulation of the optimized EFHC with a transmission ratio of 4.25, the mean power of the CTW for pay-in of the wire is 0.3 MW, but a maximum power of 2.1 MW is also observed. Note that the power needed in reality is higher since winches have an efficiency that is, of course, below 100%. It is not possible to make a fair comparison between the power usage of EFHC since no data has been found regarding average and maximum power of conventional heave compensation.

6

Conclusion & Recommendation

This chapter provides the drawn conclusions based on literature research, modelling and simulation results. Secondly, recommendations are given for future research.

6.1. Conclusions

In this thesis, a novel earth-fixed heave compensation concept has been investigated. An analytical model has been developed including the inertia, stiffness and transmission of the system to explore the working of the concept in principle. It has been found that the inertia of individual sheaves can be modelled by means of an equivalent inertia block, to significantly simplify the model for time-domain simulations.

Simulations in Liftdyn showed that vertical motions of the RNA are large for seas other than head and following waves. These peaks are caused by large roll responses of the vessel at frequencies of 0.35 rad/s and 0.63 rad/s. These frequencies are in the range of wave frequencies which means that the heading of the vessel during installation is of importance. An increasing peak period generally leads to bigger RNA motions, although small peaks are observed at natural periods of the vessel.

Analytical solutions show that earth-fixed heave compensation can be accurately modelled in OrcaFlex using a simplified model. The sheaves can be modelled by means of equivalent inertia, which significantly reduces the number of degrees of freedom of the system, saving computational time. An analytical solution is proven useful to investigate the local behavior of the sheaves in this system. Although this model only takes into account vertical motions, it shows that the individual sheaves do not rotate with significant phase difference and that their relative amplitude remains constant over a relevant frequency range. It should be noted that the losses that occur due to wire-sheave interaction are a function of tension in the wire, but simulations show that this tension can be assumed to be constant. Uncertainty in the coefficients for determining the losses result in uncertainty of the total loss in tension. Therefore, a sensitivity analysis regarding this tension should always be done. Furthermore, the analytical solution showed that wire damping has a negligible influence on the response of the system. This solves the problem of the diverse values for damping found in literature.

Modelling of the losses has confirmed that losses should be approximated by a *sigmoid* function. This function is used to approximate a *signum* function, while being continuous and differentiable. It is found that, when the slope of the sigmoid function is too high around zero, simulations become unstable. Therefore, additional simulations close to zero with increasing slope are found to be useful to determine whether results are converging.

In principle, earth-fixed heave compensation can be used to reduce vertical RNA motions. Time-domain simulations showed that it is possible to tune the transmission ratio in such a way that a motion reduction of 80% can be achieved for given environmental conditions and crane configuration. For comparison, passive and active heave compensators have a typical motion reduction of 80% and 90% respectively. Although the results are encouraging, it must be noted that large uncertainties remain. For example, the inertia of the lever arm and the stiffness of the earth-fixed wire are still unknown. On top of that, there is a large uncertainty in the losses that occur due to wire-sheave interaction. Lastly, sensitivity analyses show a strong dependency of wave period on EFHC performance, but a relatively small dependency of wave direction.

It has been proven that by altering the transmission ratio on the rotating lever arm, it is possible to improve performance of an earth-fixed heave compensator. The performance of the system remains frequency dependent. Since a range of frequencies is present in the waves, the performance has a limit. In practice, the system should be tuned on site. This needs to be considered if the system is designed in more detail.

Simulations showed that when the earth-fixed wire is connected to the seabed on the starboard side of the vessel, vessel roll motions are significantly larger than when located at the centerline of the vessel. For head waves, this is the most favorable position of the earth-fixed wire.

6.2. Recommendations

The following recommendations are given for future research. They are divided into the categories *modelling choices*, *design* and *additional research*.

6.2.1. Modelling choices

The simulations in this research were performed with a very specific sea state. Future simulations for different wave heights, peak periods and directions (including spreading) should tell how the system behaves in other sea states. In this way, it can be concluded whether the overall performance of the heave compensator is competitive.

The earth-fixed wire is in this research assumed to be rigidly attached to the seabed. In reality, the seabed has a certain stiffness. Calculations should show whether this stiffness is significantly higher than the stiffness of the earth-fixed wire and therefore can be neglected.

An analysis should be performed for the stiffness of the transmission. In this research, a beam is used as a transmission. A more detailed design of this beam would provide a stiffness and only then can be concluded whether the stiffness of the beam can be neglected or should be added to the system. This can be done by giving the beam a certain bending stiffness, but this greatly increases model complexity. An alternative method for taking the bending of the beam into account would be to add an equivalent stiffness to the earth-fixed wire, hoist wire and the constant tension winch. Nevertheless, this is not expected to have a significant influence on the behavior of the system.

The constant tension winch is assumed to deliver a pure constant tension. In reality, this is not the case. Constant tension winches have a rotational inertia and use a controller to determine the tension. When a CTW is chosen, it is necessary to add more accurate properties of the winch to the model. OrcaFlex provides an option to give a winch detailed characteristics such as inertia, this means realistic properties can simply be added to the current model.

The end of the hoist wire in the model is fixed at the crane boom in the current model. This wire actually runs over an amount of sheaves to the winch that is normally used to control the pay-in and pay-out of the hoist wire. This extra wire segment reduces the total stiffness of the hoist wire, which might result in different behavior of the heave compensation system. The model can be improved by adding this wire segment, or by calculating an equivalent stiffness for the hoist wire that represents the full wire until the winch. The effect of this additional wire segment on the dynamics is expected to be limited since the load variations, and therefore elongation, in the hoist wire are relatively small.

6.2.2. Design

If in a later design stage it is shown that the inertia of the lever arm is significantly higher, and the earth-fixed wire stiffness is significantly lower than anticipated, large errors may occur when the inertia of sheave 13 and 14 is neglected. A new assessment should be made to check if this simplification is acceptable.

A certain pretension is needed for the earth-fixed wire to prevent the wire from becoming slack. To achieve a a higher pretension, two things can be changed:

1. Increasing the mass of the lever arm. A higher tension in the earth-fixed wire will occur in equilibrium of the lever arm. The tension of the CTW and the tension in the hoist wire remain the same in this static equilibrium.

2. Increasing the force of the constant tension winch. Again, the static earth-fixed wire tension increases with increasing CTW force.

Option 1 has as advantage that the power of the CTW can remain the same. However, increasing the mass increases the rotational inertia which is disadvantageous. When option 2 is chosen, the lever arm inertia remains the same, but the power of the CTW has to increase. A trade-off has to be made between these two options to determine the best combination.

The CTW has been modelled at a convenient location at the stern of the vessel, outside the hull. In reality, this CTW has to be placed somewhere on the vessel deck which means that, for the current configuration of the heave compensator, the wire of the CTW has to be rerouted to deck via sheaves. This increase in wire length and the presence of sheaves might affect the system's behaviour and should therefore be investigated.

The connection to the seabed is not considered in this report. Further research is necessary to determine how the wire should be connected. Options for this are an anchor, a suction bucket or a clump weight.

6.2.3. Additional research

The research in this thesis is mainly based on the response of the system without considering transient effects. How should the earth fixed wire be pre-tensioned? What happens at set-down? These questions should be answered when designing earth-fixed heave compensation.

As mentioned, crane upgrades might be executed in the near future for HLV Aegir. A larger boom length is necessary to reach higher lifting heights. This does not only change vessel, crane tip and RNA motions, but also affects the dynamic behavior of earth-fixed heave compensation. Wires will be longer and have a lower stiffness. A new crane boom and longer wires can be added to the model presented in this thesis to investigate the behavior for a larger crane boom.

In the current model, dynamic positioning is modelled as a set of springs to position the vessel. For first simulations this is considered acceptable since the horizontal motions do in principle not affect the vertical motions of the payload. The dynamic positioning system could, however, be affected by the presence of the earth-fixed wire. When the vessel moves in the horizontal plane, the earth-fixed wire has a horizontal force component that might disturb the dynamic positioning of the vessel. Detailed simulations should point out whether this is a problem.

A challenge in both earth-fixed heave compensation and conventional active heave compensation is the repetitive movement of the hoist wire over sheaves. This phenomenon tends to wear wires down and is not considered in this report. When designing earth-fixed heave compensation, this should also be taken into account.

Brakes for the hoist wire should be designed for engaging and disengaging the system. On top of this, the system should be designed to be fail-safe. If the system, for whatever reason, malfunctions or shows excessive behaviour, the system should be able to stop safely.

Simulations show that the performance of the system rapidly decreases for an earth-fixed wire with reduced stiffness. When this system would be used in deeper waters, the wire stiffness would become too low for the system to function properly. An alternative that is worth investigating is the use of stiff chain links for the lower part of the earth-fixed wire. These chain links might be beneficial for the performance of the system. Note that the weight of the relatively heavy chain links should be taken into account. On top of the chain link, a wire can be connected to connect to the lever arm via sheaves.

References

Barge Master. (2013). *Barge Master Crane Trials*. https://www.barge-master.com/item/barge-master-crane-trials/

Bentley Systems. (2018). *Offshore Platform Design and Simulation Software - MOSES*. https://www.bentley.com/en/products/product-line/offshore-structural-analysis-software/moses

Chaplin, C. R. (1981). *Damping in wire rope*.

Cool, J. C., & Plettenburg, D. H. (1987). *Werktuigkundige systemen* (3de editie). Vssd.

Cranemaster. (2018, 24 september). *Installation of transition pieces at Greater Gabbard –*. https://www.cranemaster.com/reference/installation-of-offshore-wind-turbine-greater-gabbard/

DNV GL. (2018). *DNVGL-ST-N001 Marine Operations and Marine Warranty*.

DNV GL. (2019a). *DNVGL-RP-N103 Modelling and Analysis of Marine Operations*.

DNV GL. (2019b). *DNVGL-RP-N201 Lifting Appliances used in Subsea Operations*.

DNV GL. (2019c). *DNVGL-RP-C205 Enivronmental Conditions and Environmental Loads*.

Feyrer, K. (2007). *Wire Ropes: Tension, Endurance, Reliability*. Springer Publishing.

Fred. Olsen Windcarrier. (2019, 28 october). *Case Study: Alstom Haliade Demonstrator*. https://windcarrier.com/alstom-haliade-demonstrator-9

Gear, C. W., & Osterby, O. (1984). Solving Ordinary Differential Equations with Discontinuities. *ACM Transactions on Mathematical Software*, *10*(1), 23–44. https://doi.org/10.1145/356068.356071

Greenwood, D. T. (2006). *Advanced Dynamics*. Cambridge University Press.

Gu, P., Walid, A. A., Iskandarani, Y., & Karimi, H. R. (2012). Modeling, simulation and design optimization of a hoisting rig active heave compensation system. *International Journal of Machine Learning and Cybernetics*, *4*(2), 85–98. https://doi.org/10.1007/s13042-012-0076-x

Hatleskog, J. T., & Dunnigan, M. W. (2006). Heave Compensation Simulation for Non-Contact Operations in Deep Water. *OCEANS 2006*, 1–6. https://doi.org/10.1109/oceans.2006.307096

Heerema Marine Contractors. (2016). *SC-201 Standard Criteria for Engineering Design - Single Crane Lift Systems*.

Heerema Marine Contractors. (2018a). *Heerema's DP3 Vessel Aegir Installs First Offshore Wind Turbine*. https://hmc.heerema.com/news-media/news/heeremas-dp3-vessel-aegir-installs-first-offshore-wind-turbine/

Heerema Marine Contractors. (2018). *LiftDyn Theory Manual*.

Heerema Marine Contractors. (2018b). *Rigging Spreadsheet Manual*.

Heerema Marine Contractors. (2019). *Parkwind, Heerema and MHI Vestas announce a revolutionary construction methodology for Arcadis Ost 1*. https://hmc.heerema.com/news-media/news/parkwind-heerema-and-mhi-vestas-announce-a-revolutionary-construction-methodology-for-arcadis-ost-1/

Heerema Marine Contractors. (2020). *Winches*. https://hmc.heerema.com/equipment-for-rentalsales/winches/

Heerema Marine Contractors. (2018a). *Heerema's DP3 Vessel Aegir Installs First Offshore Wind Turbine*. https://hmc.heerema.com/news-media/news/heeremas-dp3-vessel-aegir-installs-first-offshore-wind-turbine/

Heller, S. R. (1970). The Contact Pressure between Wire and Sheave. *Naval Engineers Journal*, *82*(1), 49–57. https://doi.org/10.1111/j.1559-3584.1970.tb05195.x

Herdzik, J. (2014). Utilization of an Active and/or Passive Heave Compensation in the Equipment of Dynamic Positioning Vessels. *Journal of KONES. Powertrain and Transport*, *21*(2), 89–95. https://doi.org/10.5604/12314005.1133875

Holthuijsen, L. H., & Leo H., H. (2010). *Waves in Oceanic and Coastal Waters*. Cambridge University Press.

Jiang, Z., Gao, Z., Ren, Z., Li, Y., & Duan, L. (2018). A parametric study on the final blade installation process for monopile wind turbines under rough environmental conditions. *Engineering Structures*, *172*, 1042–1056. https://doi.org/10.1016/j.engstruct.2018.04.078

Journée, J. M. J., & Massie, W. W. (2001). *Offshore Hydromechanics*. Delft University of Technology.

MARIN. (2014). *aNySIM, a Versatile Hydrodynamics Engineering Tool*. https://www.marin.nl/publication/anysim-a-versatile-hydrodynamics-engineering-tool

Müller, H. K. (1990). *Abdichtung bewegter Maschinenteile*. Medienverl. Müller.

Naaijen, P. (2019) *Motions and Loadings of Structures in Waves Course Notes*. Delft University of Technology.

Nabijou, S., & Hobbs, R. (1994). Fatigue of wire ropes bent over small sheaves. *International Journal of Fatigue*, *16*(7), 453–460. https://doi.org/10.1016/0142-1123(94)90195-3

Nielsen, F. G. (2007). *Lecture Notes in Marine Operations*. Department of Marine Hydrodynamics, Faculty of Marine Engineering, Norwegian University of Science and Technology.

Oceanmax. (2014). Ropes for Oil & Gas Applications. https://www.deruiterstaalkabel.nl/wp-content/uploads/2015/11/oceanmax-ropes-for-oil-gas-applications.pdf

Offshore Engineer. (2013, 30 july). *The heave compensation conundrum*. Offshore Engineer Magazine. https://www.oedigital.com/news/445743-the-heave-compensation-conundrum

Orcina. (2020). *Orcina Literature*. https://www.orcina.com/resources/literature/

Ormond, M. J. (2011). *Depth compensated subsea passive heave compensator*. US Patent 7934561.

Ren, Z., Jiang, Z., Skjetne, R., & Gao, Z. (2018). Development and application of a simulator for offshore wind turbine blades installation. *Ocean Engineering*, *166*, 380–395. https://doi.org/10.1016/j.oceaneng.2018.05.011

Saipem. (2020). *Hywind*. https://www.saipem.com/en/projects/hywind

Scaldis. (2020). *Transport and installation of two 5MW wind turbine generators for the Beatrice Demonstrator Project*. http://www.scaldis-smc.com/en/projects/groen-2007-jul-beatrice/

Schüthe, D., Wenk, F., & Frese, U. (2016). Dynamics Calibration of a Redundant Flexible Joint Robot based on Gyroscopes and Encoders. *Proceedings of the 13th International Conference on Informatics in Control, Automation and Robotics*, 335–346. https://doi.org/10.5220/0005976603350346

Segeren, M. L. A., van der Zee, T. J. J., Lourens, E.-M., & Tsouvalas, A. (2014). Investigation of a slip joint connection between the monopile and the tower of an offshore wind turbine. *IET Renewable Power Generation*, *8*(4), 422–432. https://doi.org/10.1049/iet-rpg.2013.0163

SMI Offshore. (2015, 14 september). *Constant tension winch systems*. https://www.smi-offshore.com/product/constant-tension-winch-systems/

Spijkers, J. M. J., Vrouwenvelder, A. W. C. M. & Klaver, E. C. (2005). Structural Dynamics CT4140 – Part 1: Structural Vibrations. Delft University of Technology, Faculty of Civil Engineering and Geosciences.

Temporary Works Design. (2019). *Offshore Wind - Installation Engineering of the Future*. https://twd.nl/wp-content/uploads/2019/10/Whitepaper-Offshore-Wind-Online.pdf

Thomsen, K. E. (2014). *Offshore Wind (Second Edition)*. Academic Press.

Valk, R van der. (2017). Master Thesis: *Hoist and Boom Wire Dynamics during Offshore Heavy Lifting*. Delft University of Technology.

WAMIT. (2019). *WAMIT*. https://www.wamit.com/index.htm

Wang, S., Sun, Y., Chen, H., & Du, J. (2017). Dynamic modelling and analysis of 3-axis motion compensated offshore cranes. *Ships and Offshore Structures*, *13*(3), 265–272. https://doi.org/10.1080/17445302.2017.1360981

Wind Europe. (2019). *Offshore wind in Europe - Key trends and statistics 2019*. https://windeurope.org/wp-content/uploads/files/about-wind/statistics/WindEurope-Annual-Offshore-Statistics-2019.pdf

Woodacre, J. K., Bauer, R. J., & Irani, R. A. (2015). A review of vertical motion heave compensation systems. *Ocean Engineering*, *104*, 140–154. https://doi.org/10.1016/j.oceaneng.2015.05.004

YMV. (2019). *YMV Constant Tension Winch*. http://www.ymvcrane.com/constanttensionwinch.html

Zhao, Y., Cheng, Z., Sandvik, P. C., Gao, Z., Moan, T., & Van Buren, E. (2018). Numerical modeling and analysis of the dynamic motion response of an offshore wind turbine blade during installation by a jack-up crane vessel. *Ocean Engineering*, *165*, 353–364. https://doi.org/10.1016/j.oceaneng.2018.07.049

Zhao, Y., Cheng, Z., Gao, Z., Sandvik, P. C., & Moan, T. (2019). Numerical study on the feasibility of offshore single blade installation by floating crane vessels. *Marine Structures*, *64*, 442–462. https://doi.org/10.1016/j.marstruc.2018.12.001

A

Potential Wave Theory

In subsection 2.3.2, the global behaviour of waves is described. To understand more of the motions of structures in waves, potential wave theory should be understood. Potential wave theory considers a *potential function*, or Φ_w, of which the first partial derivative with respect to a coordinate equals the particle velocity in that direction (Journée and Massie, 2001). Equation A.1 shows this relationship.

$$u = v_x = \frac{\partial \Phi_w}{\partial x} \qquad v = v_y = \frac{\partial \Phi_w}{\partial y} \qquad w = v_z = \frac{\partial \Phi_w}{\partial z} \tag{A.1}$$

In which u, v and w are the particle velocities in x-, y- and z-direction respectively. Assuming that the fluid is incompressible and homogeneous, the fluid has to fulfil the continuity equation as shown in Equation A.2 or Equation A.3 (Journée and Massie, 2001). The latter is the continuity equation in potential form, also known as the Laplace Equation.

$$\frac{\partial u}{\partial x} + \frac{\partial v}{\partial y} + \frac{\partial w}{\partial z} = 0 \tag{A.2}$$

$$\frac{\partial^2 \Phi_w}{\partial x^2} + \frac{\partial^2 \Phi_w}{\partial y^2} + \frac{\partial^2 \Phi_w}{\partial z^2} = 0 \tag{A.3}$$

To find a solution for the wave particle velocities, boundary conditions have to be found first. Water can, for instance, not protrude the seabed. On top of that, boundary conditions at the free water surface should be found. The potential for an undisturbed wave is given by Equation A.4 (Naaijen, 2019).

$$\Phi_w(x, y, z, t) = \frac{\zeta_a g}{\omega} \sin(kx\cos\mu + ky\sin\mu - \omega t) \tag{A.4}$$

B

RNA Dimensions

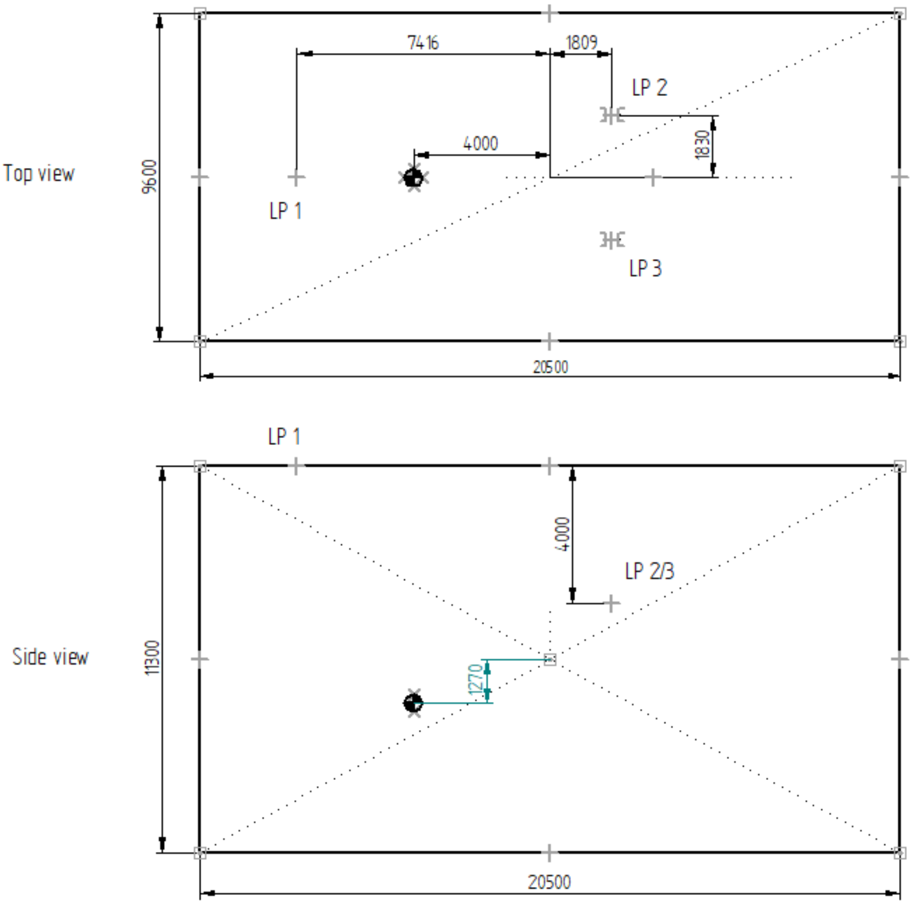

Figure B.1: RNA Dimensions and lift point locations.

C

Analytical Models

C.1. Analytical model stage 2 - equations of motion

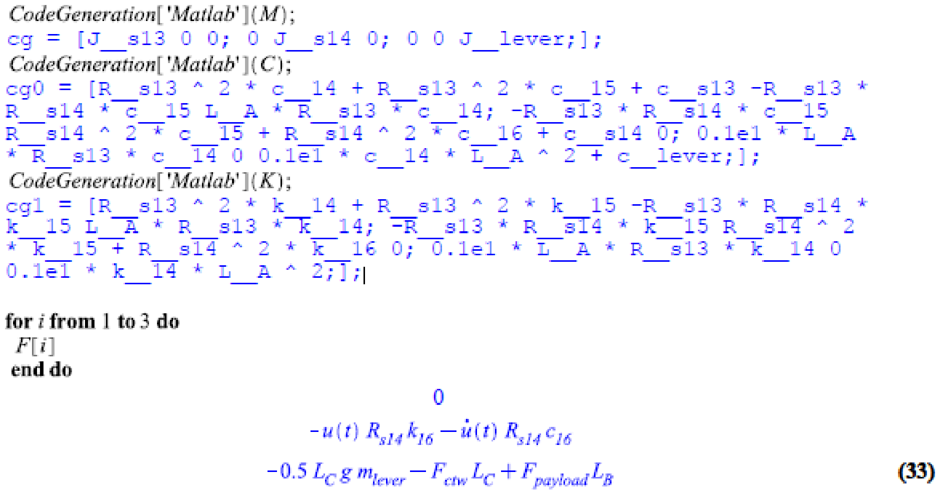

```
CodeGeneration['Matlab'](M);
cg = [J__s13 0 0; 0 J__s14 0; 0 0 J__lever;];
CodeGeneration['Matlab'](C);
cg0 = [R__s13 ^ 2 * c__14 + R__s13 ^ 2 * c__15 + c__s13 -R__s13 *
R__s14 * c__15 L__A * R__s13 * c__14; -R__s13 * R__s14 * c__15
R__s14 ^ 2 * c__15 + R__s14 ^ 2 * c__16 + c__s14 0; 0.1e1 * L__A
* R__s13 * c__14 0 0.1e1 * c__14 * L__A ^ 2 + c__lever;];
CodeGeneration['Matlab'](K);
cg1 = [R__s13 ^ 2 * k__14 + R__s13 ^ 2 * k__15 -R__s13 * R__s14 *
k__15 L__A * R__s13 * k__14; -R__s13 * R__s14 * k__15 R__s14 ^ 2
* k__15 + R__s14 ^ 2 * k__16 0; 0.1e1 * L__A * R__s13 * k__14 0
0.1e1 * k__14 * L__A ^ 2;];

for i from 1 to 3 do
 F[i]
end do
```

$$\begin{array}{c} 0 \\ -u(t)\, R_{s14}\, k_{16} - \dot{u}(t)\, R_{s14}\, c_{16} \\ -0.5\, L_C\, g\, m_{lever} - F_{ctw}\, L_C + F_{payload}\, L_B \end{array} \qquad \textbf{(33)}$$

Figure C.1: M, C and K matrix for the equations of motions of modelling stage 2 and the external force vector.

C.2. Analytical model stage 3 - schematic drawing

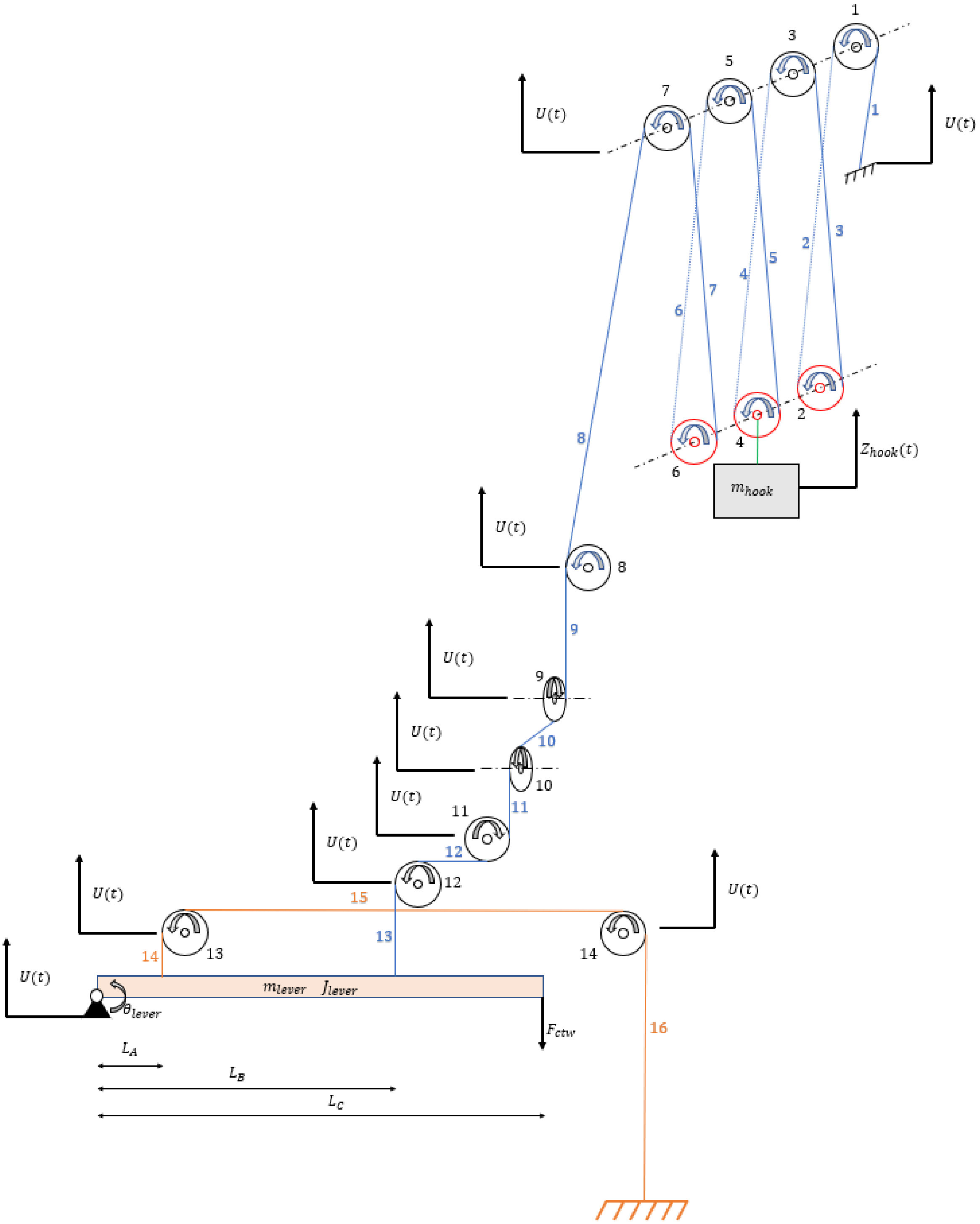

Figure C.2: Modelling stage 3.

C.3. Analytical model step 3 - degrees of freedom and parameters.

#	DoF	Unit	Parameter	Value	Unit	Parameter	Value	Unit
1	θ_{s1}	rad	l_1	0.1	m	r_1 (i-o)	0.25 - 0.72	m
2	θ_{s2}	rad	l_2	4	m	r_2 (i-o)	0.25 - 0.95	m
3	θ_{s3}	rad	l_3	4	m	r_3 (i-o)	0.25 - 0.72	m
4	θ_{s4}	rad	l_4	4	m	r_4 (i-o)	0.25 - 0.95	m
5	θ_{s5}	rad	l_5	4	m	r_5 (i-o)	0.25 - 0.72	m
6	θ_{s6}	rad	l_6	4	m	r_6 (i-o)	0.25 - 0.95	m
7	θ_{s7}	rad	l_7	4	m	r_7 (i-o)	0.25 - 0.72	m
8	θ_{s8}	rad	l_8	93.5	m	r_8 (i-o)	0.25 - 0.72	m
9	θ_{s9}	rad	l_9	29.1	m	r_9 (i-o)	0.25 - 0.72	m
10	θ_{s10}	rad	l_{10}	9.4	m	r_{10} (i-o)	0.25 - 0.72	m
11	θ_{s11}	rad	l_{11}	1	m	r_{11} (i-o)	0.25 - 0.72	m
12	θ_{s12}	rad	l_{12}	7.7	m	r_{12} (i-o)	0.25 - 0.72	m
13	θ_{s13}	rad	l_{13}	3.6	m	r_{13} (i-o)	0.25 - 0.95	m
14	θ_{s14}	rad	l_{14}	3	m	r_{14} (i-o)	0.25 - 0.95	m
15	θ_{lever}	rad	l_{15}	25.1	m	m_1	560	kg
16	z_{hook}	m	l_{16}	66.5	m	m_2	870	kg
(17	x_{block}	m)	k_1	$2.76 \cdot 10^9$	N/m	m_3	560	kg
			k_2	$6.9 \cdot 10^7$	N/m	m_4	870	kg
			k_3	$6.9 \cdot 10^7$	N/m	m_5	560	kg
			k_4	$6.9 \cdot 10^7$	N/m	m_6	870	kg
			k_5	$6.9 \cdot 10^7$	N/m	m_7	560	kg
			k_6	$6.9 \cdot 10^7$	N/m	m_8	560	kg
			k_7	$6.9 \cdot 10^7$	N/m	m_9	560	kg
			k_8	$2.95 \cdot 10^6$	N/m	m_{10}	560	kg
			k_9	$9.5 \cdot 10^6$	N/m	m_{11}	560	kg
			k_{10}	$2.95 \cdot 10^7$	N/m	m_{12}	560	kg
			k_{11}	$2.67 \cdot 10^8$	N/m	m_{13}	870	kg
			k_{12}	$3.58 \cdot 10^7$	N/m	m_{14}	870	kg
			k_{13}	$3.75 \cdot 10^7$	N/m	J_{lever}	$3.75 \cdot 10^6$	$kg \cdot m^2$
			k_{14}	$3.75 \cdot 10^6$	N/m	m_{lever}	50.000	kg
			k_{15}	$3.75 \cdot 10^6$	N/m	F_{ctw}	$7.36 \cdot 10^3$	kN
			k_{16}	$3.75 \cdot 10^6$	N/m	(m$_{block}$	6.700	kg)

Table C.1: Degrees of freedom and parameter values for modelling stage 3.

C.4. Analytical model stage 3 - equations of motion

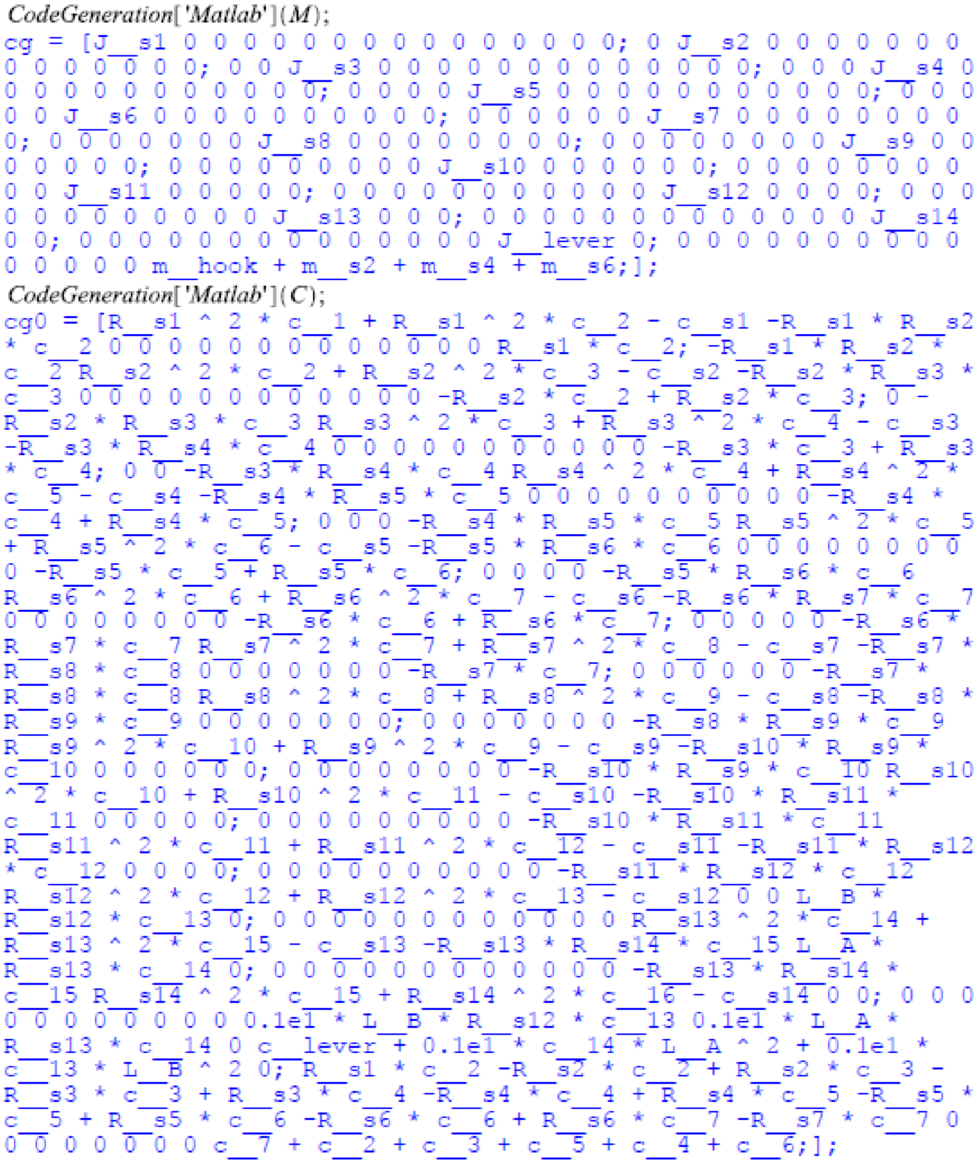

```
CodeGeneration['Matlab'](M);
cg = [J__s1 0 0 0 0 0 0 0 0 0 0 0 0 0 0 0; 0 J__s2 0 0 0 0 0 0 0
0 0 0 0 0 0 0; 0 0 J__s3 0 0 0 0 0 0 0 0 0 0 0 0 0; 0 0 0 J__s4 0
0 0 0 0 0 0 0 0 0 0 0; 0 0 0 0 J__s5 0 0 0 0 0 0 0 0 0 0 0; 0 0 0
0 0 J__s6 0 0 0 0 0 0 0 0 0 0; 0 0 0 0 0 0 J__s7 0 0 0 0 0 0 0 0
0; 0 0 0 0 0 0 0 J__s8 0 0 0 0 0 0 0 0; 0 0 0 0 0 0 0 0 J__s9 0 0
0 0 0 0 0; 0 0 0 0 0 0 0 0 0 J__s10 0 0 0 0 0 0; 0 0 0 0 0 0 0 0
0 0 J__s11 0 0 0 0 0; 0 0 0 0 0 0 0 0 0 0 0 J__s12 0 0 0 0; 0 0 0
0 0 0 0 0 0 0 0 0 J__s13 0 0 0; 0 0 0 0 0 0 0 0 0 0 0 0 0 J__s14
0 0; 0 0 0 0 0 0 0 0 0 0 0 0 0 0 J__lever 0; 0 0 0 0 0 0 0 0 0 0
0 0 0 0 0 m__hook + m__s2 + m__s4 + m__s6;];
CodeGeneration['Matlab'](C);
cg0 = [R__s1 ^ 2 * c__1 + R__s1 ^ 2 * c__2 - c__s1 -R__s1 * R__s2
* c__2 0 0 0 0 0 0 0 0 0 0 0 0 0 R__s1 * c__2; -R__s1 * R__s2 *
c__2 R__s2 ^ 2 * c__2 + R__s2 ^ 2 * c__3 - c__s2 -R__s2 * R__s3 *
c__3 0 0 0 0 0 0 0 0 0 0 0 0 -R__s2 * c__2 + R__s2 * c__3; 0 -
R__s2 * R__s3 * c__3 R__s3 ^ 2 * c__3 + R__s3 ^ 2 * c__4 - c__s3
-R__s3 * R__s4 * c__4 0 0 0 0 0 0 0 0 0 0 0 -R__s3 * c__3 + R__s3
* c__4; 0 0 -R__s3 * R__s4 * c__4 R__s4 ^ 2 * c__4 + R__s4 ^ 2 *
c__5 - c__s4 -R__s4 * R__s5 * c__5 0 0 0 0 0 0 0 0 0 0 -R__s4 *
c__4 + R__s4 * c__5; 0 0 0 -R__s4 * R__s5 * c__5 R__s5 ^ 2 * c__5
+ R__s5 ^ 2 * c__6 - c__s5 -R__s5 * R__s6 * c__6 0 0 0 0 0 0 0 0
0 -R__s5 * c__5 + R__s5 * c__6; 0 0 0 0 -R__s5 * R__s6 * c__6
R__s6 ^ 2 * c__6 + R__s6 ^ 2 * c__7 - c__s6 -R__s6 * R__s7 * c__7
0 0 0 0 0 0 0 0 -R__s6 * c__6 + R__s6 * c__7; 0 0 0 0 0 -R__s6 *
R__s7 * c__7 R__s7 ^ 2 * c__7 + R__s7 ^ 2 * c__8 - c__s7 -R__s7 *
R__s8 * c__8 0 0 0 0 0 0 0 -R__s7 * c__7; 0 0 0 0 0 0 -R__s7 *
R__s8 * c__8 R__s8 ^ 2 * c__8 + R__s8 ^ 2 * c__9 - c__s8 -R__s8 *
R__s9 * c__9 0 0 0 0 0 0 0; 0 0 0 0 0 0 0 -R__s8 * R__s9 * c__9
R__s9 ^ 2 * c__10 + R__s9 ^ 2 * c__9 - c__s9 -R__s10 * R__s9 *
c__10 0 0 0 0 0 0; 0 0 0 0 0 0 0 0 -R__s10 * R__s9 * c__10 R__s10
^ 2 * c__10 + R__s10 ^ 2 * c__11 - c__s10 -R__s10 * R__s11 *
c__11 0 0 0 0 0; 0 0 0 0 0 0 0 0 0 -R__s10 * R__s11 * c__11
R__s11 ^ 2 * c__11 + R__s11 ^ 2 * c__12 - c__s11 -R__s11 * R__s12
* c__12 0 0 0 0; 0 0 0 0 0 0 0 0 0 0 -R__s11 * R__s12 * c__12
R__s12 ^ 2 * c__12 + R__s12 ^ 2 * c__13 - c__s12 0 0 L__B *
R__s12 * c__13 0; 0 0 0 0 0 0 0 0 0 0 0 0 R__s13 ^ 2 * c__14 +
R__s13 ^ 2 * c__15 - c__s13 -R__s13 * R__s14 * c__15 L__A *
R__s13 * c__14 0; 0 0 0 0 0 0 0 0 0 0 0 0 -R__s13 * R__s14 *
c__15 R__s14 ^ 2 * c__15 + R__s14 ^ 2 * c__16 - c__s14 0 0; 0 0 0
0 0 0 0 0 0 0 0 0 0.1e1 * L__B * R__s12 * c__13 0.1e1 * L__A *
R__s13 * c__14 0 c__lever + 0.1e1 * c__14 * L__A ^ 2 + 0.1e1 *
c__13 * L__B ^ 2 0; R__s1 * c__2 -R__s2 * c__2 + R__s2 * c__3 -
R__s3 * c__3 + R__s3 * c__4 -R__s4 * c__4 + R__s4 * c__5 -R__s5 *
c__5 + R__s5 * c__6 -R__s6 * c__6 + R__s6 * c__7 -R__s7 * c__7 0
0 0 0 0 0 0 0 c__7 + c__2 + c__3 + c__5 + c__4 + c__6;];
```

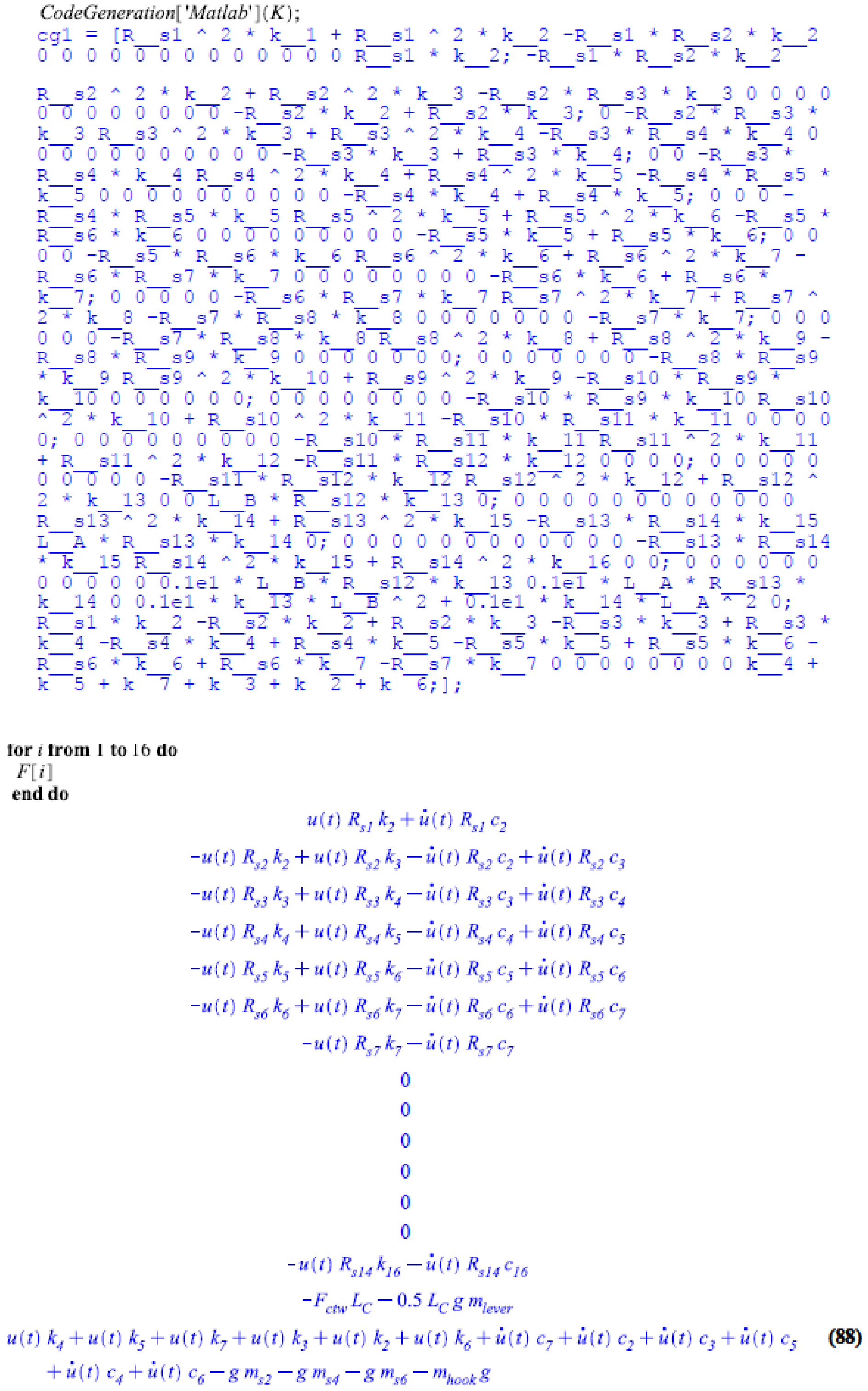

CodeGeneration['Matlab'](K);

```
cg1 = [R__s1 ^ 2 * k__1 + R__s1 ^ 2 * k__2 -R__s1 * R__s2 * k__2
0 0 0 0 0 0 0 0 0 0 0 0 0 R__s1 * k__2; -R__s1 * R__s2 * k__2

R__s2 ^ 2 * k__2 + R__s2 ^ 2 * k__3 -R__s2 * R__s3 * k__3 0 0 0 0
0 0 0 0 0 0 0 0 -R__s2 * k__2 + R__s2 * k__3; 0 -R__s2 * R__s3 *
k__3 R__s3 ^ 2 * k__3 + R__s3 ^ 2 * k__4 -R__s3 * R__s4 * k__4 0
0 0 0 0 0 0 0 0 0 0 -R__s3 * k__3 + R__s3 * k__4; 0 0 -R__s3 *
R__s4 * k__4 R__s4 ^ 2 * k__4 + R__s4 ^ 2 * k__5 -R__s4 * R__s5 *
k__5 0 0 0 0 0 0 0 0 0 0 -R__s4 * k__4 + R__s4 * k__5; 0 0 0 -
R__s4 * R__s5 * k__5 R__s5 ^ 2 * k__5 + R__s5 ^ 2 * k__6 -R__s5 *
R__s6 * k__6 0 0 0 0 0 0 0 0 0 -R__s5 * k__5 + R__s5 * k__6; 0 0
0 0 -R__s5 * R__s6 * k__6 R__s6 ^ 2 * k__6 + R__s6 ^ 2 * k__7 -
R__s6 * R__s7 * k__7 0 0 0 0 0 0 0 0 -R__s6 * k__6 + R__s6 *
k__7; 0 0 0 0 0 -R__s6 * R__s7 * k__7 R__s7 ^ 2 * k__7 + R__s7 ^
2 * k__8 -R__s7 * R__s8 * k__8 0 0 0 0 0 0 0 -R__s7 * k__7; 0 0 0
0 0 0 -R__s7 * R__s8 * k__8 R__s8 ^ 2 * k__8 + R__s8 ^ 2 * k__9 -
R__s8 * R__s9 * k__9 0 0 0 0 0 0 0; 0 0 0 0 0 0 0 -R__s8 * R__s9
* k__9 R__s9 ^ 2 * k__10 + R__s9 ^ 2 * k__9 -R__s10 * R__s9 *
k__10 0 0 0 0 0 0; 0 0 0 0 0 0 0 0 -R__s10 * R__s9 * k__10 R__s10
^ 2 * k__10 + R__s10 ^ 2 * k__11 -R__s10 * R__s11 * k__11 0 0 0 0
0; 0 0 0 0 0 0 0 0 0 -R__s10 * R__s11 * k__11 R__s11 ^ 2 * k__11
+ R__s11 ^ 2 * k__12 -R__s11 * R__s12 * k__12 0 0 0 0; 0 0 0 0 0
0 0 0 0 0 -R__s11 * R__s12 * k__12 R__s12 ^ 2 * k__12 + R__s12 ^
2 * k__13 0 0 L__B * R__s12 * k__13 0; 0 0 0 0 0 0 0 0 0 0 0 0 0
R__s13 ^ 2 * k__14 + R__s13 ^ 2 * k__15 -R__s13 * R__s14 * k__15
L__A * R__s13 * k__14 0; 0 0 0 0 0 0 0 0 0 0 0 0 -R__s13 * R__s14
* k__15 R__s14 ^ 2 * k__15 + R__s14 ^ 2 * k__16 0 0; 0 0 0 0 0 0
0 0 0 0 0 0.1e1 * L__B * R__s12 * k__13 0.1e1 * L__A * R__s13 *
k__14 0 0.1e1 * k__13 * L__B ^ 2 + 0.1e1 * k__14 * L__A ^ 2 0;
R__s1 * k__2 -R__s2 * k__2 + R__s2 * k__3 -R__s3 * k__3 + R__s3 *
k__4 -R__s4 * k__4 + R__s4 * k__5 -R__s5 * k__5 + R__s5 * k__6 -
R__s6 * k__6 + R__s6 * k__7 -R__s7 * k__7 0 0 0 0 0 0 0 0 k__4 +
k__5 + k__7 + k__3 + k__2 + k__6;];
```

for *i* **from** 1 **to** 16 **do**
F[*i*]
end do

$$u(t)\ R_{s1}\, k_2 + \dot{u}(t)\ R_{s1}\, c_2$$

$$-u(t)\ R_{s2}\, k_2 + u(t)\ R_{s2}\, k_3 - \dot{u}(t)\ R_{s2}\, c_2 + \dot{u}(t)\ R_{s2}\, c_3$$

$$-u(t)\ R_{s3}\, k_3 + u(t)\ R_{s3}\, k_4 - \dot{u}(t)\ R_{s3}\, c_3 + \dot{u}(t)\ R_{s3}\, c_4$$

$$-u(t)\ R_{s4}\, k_4 + u(t)\ R_{s4}\, k_5 - \dot{u}(t)\ R_{s4}\, c_4 + \dot{u}(t)\ R_{s4}\, c_5$$

$$-u(t)\ R_{s5}\, k_5 + u(t)\ R_{s5}\, k_6 - \dot{u}(t)\ R_{s5}\, c_5 + \dot{u}(t)\ R_{s5}\, c_6$$

$$-u(t)\ R_{s6}\, k_6 + u(t)\ R_{s6}\, k_7 - \dot{u}(t)\ R_{s6}\, c_6 + \dot{u}(t)\ R_{s6}\, c_7$$

$$-u(t)\ R_{s7}\, k_7 - \dot{u}(t)\ R_{s7}\, c_7$$

$$0$$

$$0$$

$$0$$

$$0$$

$$0$$

$$0$$

$$-u(t)\ R_{s14}\, k_{16} - \dot{u}(t)\ R_{s14}\, c_{16}$$

$$-F_{ctw}\, L_C - 0.5\ L_C\, g\ m_{lever}$$

$$u(t)\ k_4 + u(t)\ k_5 + u(t)\ k_7 + u(t)\ k_3 + u(t)\ k_2 + u(t)\ k_6 + \dot{u}(t)\ c_7 + \dot{u}(t)\ c_2 + \dot{u}(t)\ c_3 + \dot{u}(t)\ c_5 + \dot{u}(t)\ c_4 + \dot{u}(t)\ c_6 - g\ m_{s2} - g\ m_{s4} - g\ m_{s6} - m_{hook}\, g \qquad \textbf{(88)}$$

Figure C.3: M, C and K matrix for the equations of motions of modelling stage 3 and the external force vector.

D

Time Series

D.1. Vessel and payload: without earth-fixed heave compensation

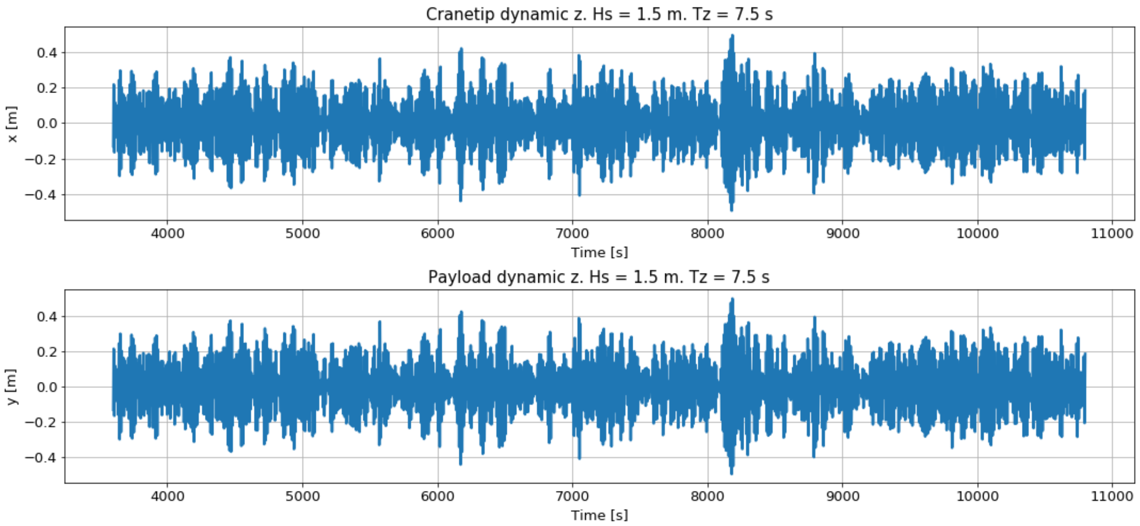

Figure D.1: Time series of crane tip and payload motions without earth-fixed heave compensation.

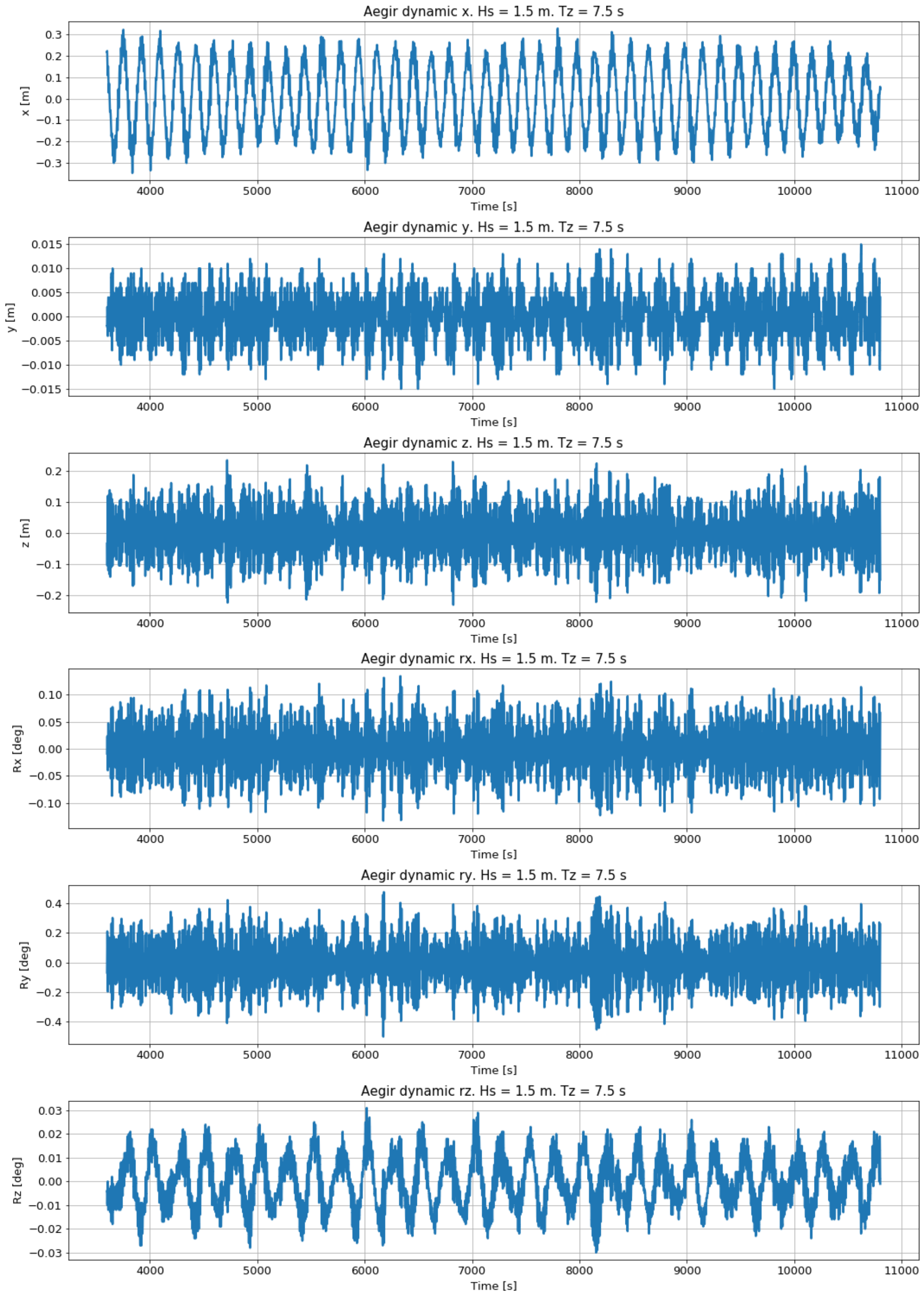

Figure D.2: Time series of vessel motions without earth-fixed heave compensation.

E

Sensitivity Analysis

Figures below show the sensitivity to different mean zero-crossing periods of the JONSWAP wave spectrum and to the wave direction.

E.1. Wave period

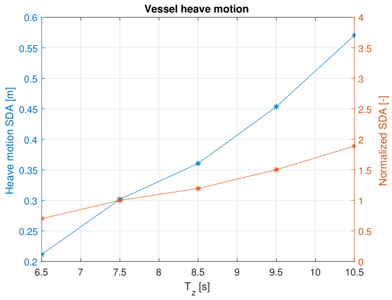

Figure E.1: Vessel heave motion for different wave periods.

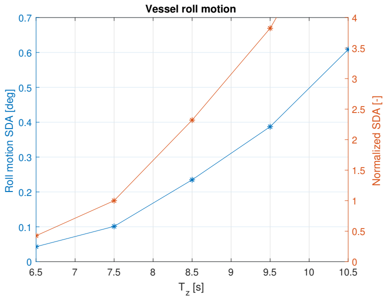

Figure E.2: Vessel roll motion for different wave periods.

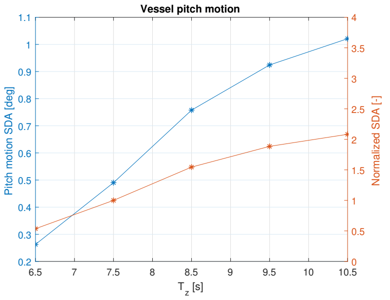

Figure E.3: Vessel pitch motion for different wave periods.

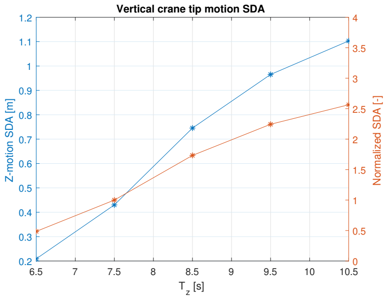

Figure E.4: Cranetip vertical motion for different wave periods.

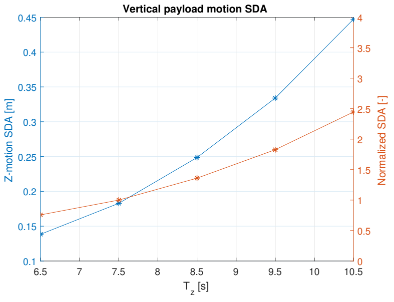

Figure E.5: Payload vertical motion for different wave periods.

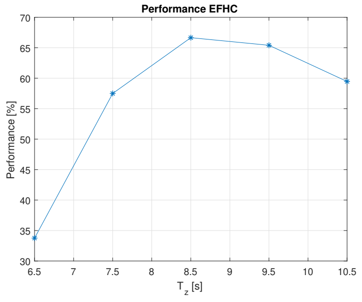

Figure E.6: EFHC performance for different wave periods.

E.2. Wave direction

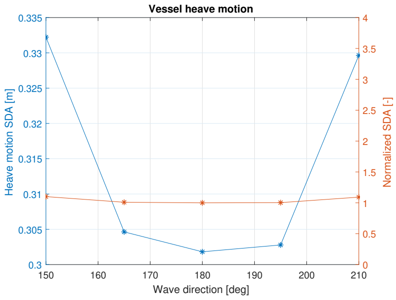

Figure E.7: Vessel heave motion for different wave directions.

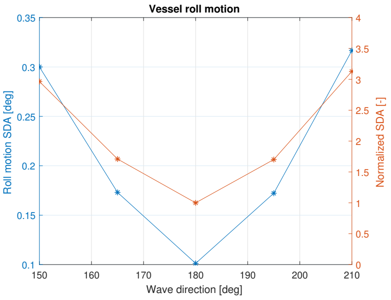

Figure E.8: Vessel roll motion for different wave directions.

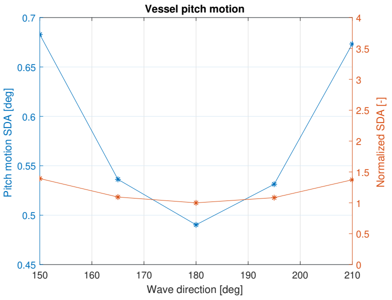

Figure E.9: Vessel pitch motion for different wave directions.

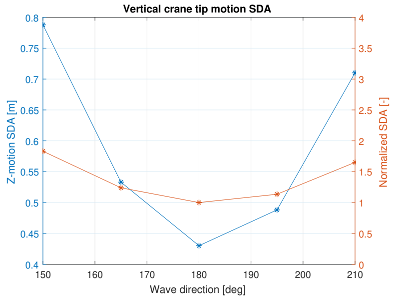

Figure E.10: Cranetip vertical motion for different wave directions.

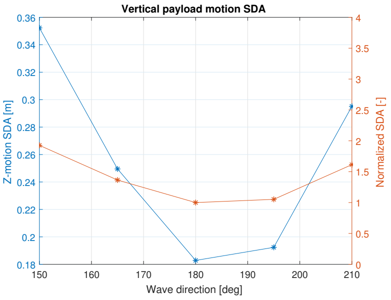

Figure E.11: Payload vertical motion for different wave directions.

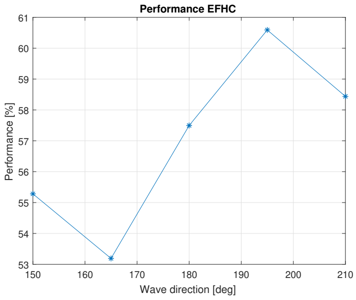

Figure E.12: EFHC performance for different wave directions.

E.3. Payload mass

A set of simulations is done for a varying payload mass. This time, the mass is only adjust +/- 15%. This is done since there is no big uncertainty in the total mass of the crane block, spreader frame and RNA. Naturally, there is a possibility that the RNA mass of next generation turbines is larger. However, the capacity of the crane block and reeving is only 750 t. A large increase in mass would require a different reeving plan and crane block, and a different transmission ratio of EFHC. This is not considered in this report.

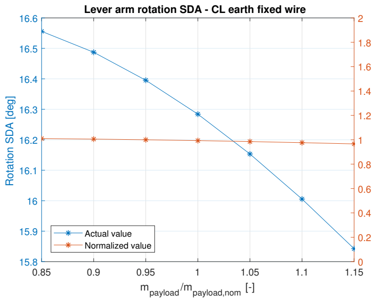

Figure E.13: Lever arm motion for varying payload mass.

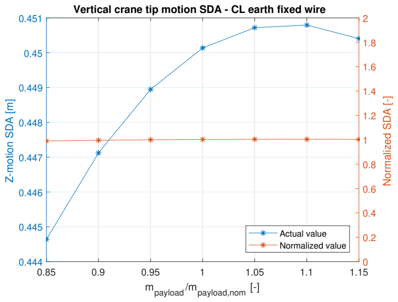

Figure E.14: Cranetip motion for varying payload mass.

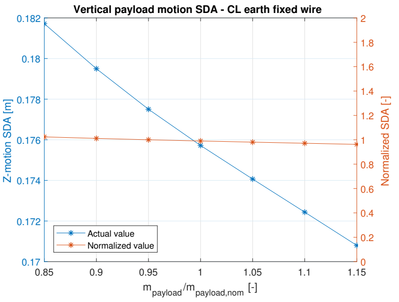

Figure E.15: Payload motion for varying payload mass.

Figures above show that the difference in behaviour of the system do not vary significantly for different payload masses. The performance increase with approximately 3% for a mass increase of 15%. Crane tip motions maximally differ 1% and the lever arm rotation decreases with maximally 3% for increasing payload mass. Figure E.16 shows there is a small dependency between the payload mass and the performance of the heave compensator.

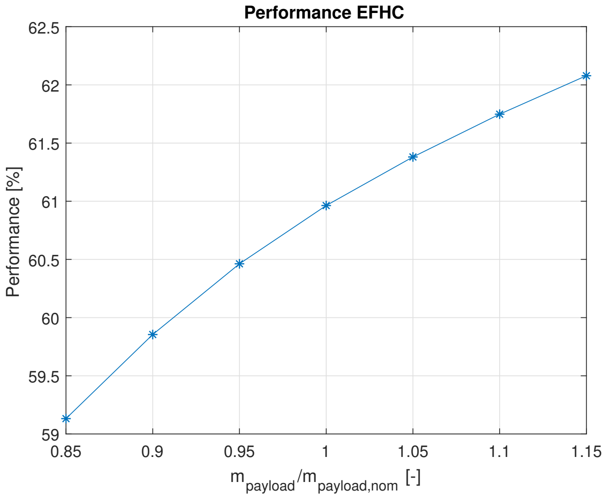

Figure E.16: EFHC performance varying payload mass.